THE UNIVERSITY OF CHICAGO

PROBING ULTRAFAST CHIRAL EXCITED STATE DYNAMICS WITH TWO-DIMENSIONAL ELECTRONIC SPECTROSCOPY

A DISSERTATION SUBMITTED TO
THE FACULTY OF THE DIVISION OF THE PHYSICAL SCIENCES
IN CANDIDACY FOR THE DEGREE OF
DOCTOR OF PHILOSOPHY

DEPARTMENT OF CHEMISTRY

BY
CAITLIN BELLORA

CHICAGO, ILLINOIS
DECEMBER 2026

© 2026 by Caitlin Bellora

ORCID iD: https://orcid.org/0000-0001-9153-9391

To my wonderful parents. Thank you for all your support!

TABLE OF CONTENTS

LIST OF FIGURES vi

LIST OF TABLES vii

ACKNOWLEDGMENTS viii

ABSTRACT ix

1 INTRODUCTION 1
1.1 Physical Origins of Chirality 1
1.2 Spectroscopic Probes of Molecular Chirality and Measurement Limitations . 4
References 9

2 THEORY OF NONLINEAR SPECTROSCOPY AND THE CHIRAL RESPONSE 14
2.1 Foundations of Light-Matter Interaction and the Linear Response 14
2.2 Third-Order Nonlinear Response and Spectroscopy 18
2.3 Polarization-Controlled Pathway Selection 23
2.4 Chiral Response: Going Beyond the Dipole Approximation 28
References 37

3 CHIRAL TRANSIENT ABSORPTION AND TWO-DIMENSIONAL ELECTRONIC SPECTROSCOPY 39
3.1 Experimental Implementation 39
3.1.1 Optical Layout 39
3.1.2 LO Heterodyne Detection in the Pump-Probe Geometry 46
3.1.3 Transient Absorption Measurements 48
3.1.4 Phase Stability and Measurement Techniques 52
3.1.5 Polarization Considerations for Optimal Chiral Signal Purity 55
3.1.6 Pulse Characterization 66
3.2 Data Processing 67
3.2.1 Third-Order Signal Isolation 67
3.2.2 Isolating Rephasing and Non Rephasing Signal Contributions 71
3.2.3 Phase Corrections 73
3.3 Generality of Chiral Data and Amenability to Traditional 2DES Analysis . . 77
3.3.1 Effect of Chirality on Excited-State Evolution 77
3.3.2 Chiral 2DES Liouville Pathway Dependence 79
References 82

4 CHIRAL EXCITONIC DYNAMICS IN PORPHYRIN AGGREGATES 87
4.1 Abstract 87
4.2 Introduction 88
4.3 Instrument Approach 92

4.3.1 Isolating the Chiral Component of the Third-Order Response 92
4.3.2 Chiral Two-Dimensional Electronic Spectrometer Design 94
4.4 Results 95
4.4.1 Sign Inversion of Chiral Signal Between Enantiomers 95
4.4.2 Spectral Features Under Chiral vs. Dipolar Polarization Conditions . 96
4.4.3 Assignment of Spectral Features to Aggregate Photophysics 97
4.5 Discussion 101
4.6 Conclusion 104
References 105

5 FUTURE DIRECTIONS 110
5.1 Single-Experiment Measurement of Multiple Polarization Conditions 110
5.2 Experimental Considerations for Optimizing Routine 2DES Data Collection . 117
5.2.1 Sample Selection Considerations 117
5.2.2 Noise Reduction Strategies 120
References 125

6 CONCLUSIONS 126

APPENDIX A TPPS AGGREGATE SAMPLE INFORMATION 129
A.1 TPPS Aggregate Synthesis 129

LIST OF FIGURES

1.1 Additional degrees of freedom accessible in symmetry broken molecular systems 3
1.2 Visual depiction of a parity transformation 5

2.1 Third-order Feynman diagrams for stimulated emission, ground state bleach, and excited state absorption pathways 21
2.2 Rephasing and non-rephasing Feynman pathways 22
2.3 Example Feynman diagrams for magnetic dipole interaction 35
2.4 Example Feynman diagrams for electric quadrupole interaction 36

3.1 Chiral two-dimensional electronic spectroscopy instrument schematic 44
3.2 Birefringent wedge assembly within the NIREOS GEMINI-2D interferometer . . 45
3.3 Pulse ordering for LO-heterodyne detected 2DES and TA measurements 51
3.4 IR144 signal minimization trend used to prepare the nominal XXXY polarization condition 58
3.5 Polarization optics positioned immediately downstream all metal mirror reflections for orthogonal probe and local oscillator polarization conditions 62
3.6 Effects of circular birefringence and circular dichroism in a chiral sample on the polarization of transmitted light that is linearly and circularly polarized. 63
3.7 Low-strain sample cell mount machined for chiral experiments 65
3.8 Temporal pulse width characterization through SHG and iFROG measurements 67
3.9 Schematic illustrating the separation of the rephasing and non-rephasing signal components 72
3.10 Local oscillator heterodyne detected transient absorption spectra before and after applying a phase correction 76

4.1 Spectral and structural characterization of chiral TPPS J-aggregates 91
4.2 Overview of chiral two-dimensional electronic spectrometer 92
4.3 TA and 2DES data under chiral and dipolar polarization conditions for the TPPS L- and D-aggregates 100
4.4 Interpretation of TPPS aggregate nonlinear chiral signal 103

5.1 Normalized achiral and chiral 2DES data frames acquired at a waiting time of t_2=5000 fs 114
5.2 Projections of the achiral and chiral 2DES data over the excitation energy axis . 115
5.3 Time evolution of real 2DES frames measured under dipolar and chiral polarization conditions 121
5.4 Singular value weights for achiral and chiral 2DES data 123
5.5 2DES frames at waiting time = 1000 fs comparing the full measured signal to the SVD reconstruction 124

LIST OF TABLES

2.1 Common dipolar polarization conditions used in 2DES and TA measurements . 27

3.1 Polarization purity measurements of the collinear pump beams for different orderings of the polarization optics 61

ACKNOWLEDGMENTS

Thank you to Professor Greg Engel for being such an incredible mentor and for helping me develop into the scientist I am today. I deeply appreciate your insight in solving seemingly endless scientific problems, as well as the freedom you gave me to pursue my ideas. Thank you to my committee members, Professor Mazziotti and Professor Tian, for your advice and support.

Thank you to all the wonderful members of the Engel group, past and present. To the Engel group members in my cohort, Dr. Qijie Shen, Dr. Coco Li, and Dr. Indranil Ghosh, I am so glad to have shared this incredible journey with such a wonderful group of people. I am also grateful to my mentors, Dr. Elizabeth M. Bain, Dr. William R. Hollingsworth, Dr. Sarah R. Zinn, Dr. Jake Higgins, Dr. Lawson T. Lloyd, and Dr. Siddhartha Sohoni, who have taught me so much and who have continuously challenged me to grow. Special thanks to Dr. Elizabeth M. Bain for inspiring me to pursue this chiral instrument development project and for patiently teaching me about lasers and Franck. To my other Franck team members, Olivia Wedig and Jaz Belz, I am grateful to have spent so much time working alongside such an exceptional group of scientists. Thank you especially to Olivia Wedig for her persistence and coding expertise throughout the many years we spent developing and troubleshooting this novel experiment.

Thank you to Dr. Bentley Wall for keeping the building operational and for managing our stringent temperature and humidity requirements. Thank you also to Dr. Karen Watters for her scientific editing.

Finally, thank you to my parents, Kenneth Bellora and Karen Bellora, for your unwavering support throughout my academic career.

This work was funded in part by the Department of Defense National Defense Science and Engineering Graduate Fellowship.

ABSTRACT

Chirality plays an integral role in the mechanisms underlying ultrafast photophysics in biological and material systems. Disentangling the mechanistic link between chiral structure and these ultrafast photophysics is critical for informing the functional design of next-generation chiral devices. However, isolating the chiral response to light from more dominant achiral contributions remains an experimental challenge that is limited by the low signal amplitude and demanding polarization purity requirements. This thesis details the development of a chiral two-dimensional electronic spectrometer (2DES), which is a tool that can be leveraged to identify the key excited-state processes driving the chiral response. Chiral 2DES records a series of snapshots that correlate the excitation and emission energy, revealing how excited state populations and coherences evolve on femtosecond timescales. This instrument was designed to optimize polarization purity, phase stability, and signal strength, while mitigating common pitfalls encountered in chiral measurements, such as strain-induced birefringence.

The chiral 2DES instrument and methods were validated in a proof of concept experiment comparing achiral and chiral spectra of helical porphyrin J-aggregates. In comparison to the standard achiral 2DES spectra, the chiral spectra exhibited enhanced resolution that revealed unique electronic transitions that are otherwise obscured in traditional dipolar measurements. The purity of the measured signals is demonstrated by the mirror symmetry of chiral spectra acquired for opposite-handed aggregates. These findings demonstrate the unique ability of chiral 2DES to provide insight into the geometrical arrangement of transition dipoles giving rise to the chiral response. Future experimental directions are proposed to further enhance the quality of the detected chiral 2DES signal. By implementing strategies to enhance signal-to-noise, future experiments will have the resolution necessary to fit dynamical models to the chiral excited-state evolution. Additionally, a dual-channel detection strategy is proposed which can minimize the acquisition time required for 2DES measurements by simultaneously measuring multiple polarization-dependent tensor components of

the emitted signal. Through the work presented in this thesis, chiral 2DES is established as a tool for routine measurements of ultrafast chiral photophysics.

CHAPTER 1

INTRODUCTION

Building smaller and more efficient optoelectronic devices requires the ability to exploit quantum mechanical properties of materials. When light interacts with a molecular system, its energy can be absorbed and stored within the system's excited state. What the material inevitably does with that stored energy depends on its structure, which governs the dynamics that ultimately determine its potential device applications.

One structural property of molecules that can be used to tune these dynamics is chirality, or handedness, which arises from an asymmetry in molecular structure. Handed materials interact differently with handed light, providing a unique opportunity to control material behavior through the coupling between the handedness of light and matter. However, how the initial chiral light-matter interaction influences the subsequent dynamics remains poorly understood. Techniques are therefore needed that can connect a material's chiral structure to its dynamics and, ultimately, its function for tailored device applications. This thesis will accomplish just that, by developing a novel instrument for characterizing the evolution of handed light-matter interaction. The instrument's capabilities are demonstrated by measuring how energy moves through materials of opposite handedness in a proof of principle measurement.

1.1 Physical Origins of Chirality

Chirality describes a particular type of geometric asymmetry in which an object cannot be superimposed on its mirror image. Louis Pasteur's work in 1848 on tartaric acid salts provided an early molecular example of chiral phenomena [1]. A common pedagogical analogy is the relationship between your left and right hands. At first glance, your hands may appear identical; however, no amount of rotation or translation will allow you to overlap one hand with

the other. That is because your left and right hands are mirror-image, non-superimposable objects, and therefore form a chiral pair. One hand exhibits a distinct left-handed symmetry, whereas the other hand exhibits right-handed symmetry. In the molecular world, a similar type of symmetry persists, where two enantiomers possess the same atomic composition and connectivity but differ in their three-dimensional arrangement.

Molecular chirality is a central component of all biological systems, making it essential to our very existence, from the molecules that build our bodies, to the food we eat. Many biomolecules, including amino acids, sugars, and proteins, occur predominantly in one handedness in living systems. This handedness preference, known as homochirality, has been an ongoing point of debate for many years [2–5].

The consequences of chirality are apparent in everyday chemical perception. This is famously demonstrated in a general chemistry lab experiment in which students smell the distinct aromas of isolated enantiomers, *S*-carvone and *R*-carvone. The *R*-carvone is commonly found in spearmint plants, where it contributes to the sweet, minty aroma. On the other hand, *S*-carvone is found in caraway seeds and has a much more earthy scent [6]. Chirality can also have far more serious consequences in pharmacology. The drug thalidomide was originally prescribed to expectant mothers as a racemic mixture, meaning it contained both thalidomide enantiomers. Thalidomide's use resulted in around 10,000 severe birth defects [7]. Later studies identified the S-enantiomer of thalidomide as teratogenic in animal models [8]. The exact mechanism is still a point of debate, because enantiomer interconversion prevents the confident link between a single enantiomer and the resulting toxicity [9]. Regardless, this example further demonstrates just how consequential chirality can be to our lives.

These examples illustrate a broader scientific principle that is central to chemistry: structure determines function. In chiral systems, two molecules may be composed of the same atoms and points of connectivity, yet their precise spatial arrangement can drastically affect

their chemical, biological, and photophysical behavior. While the examples discussed so far have emphasized the pure geometrical consequences of chirality, this thesis focuses on how chiral molecules interact with light.

Chiral molecules exhibit optical activity, meaning they exhibit a differential response to left- and right- circularly polarized light [10]. This differential response arises from two effects: circular birefringence, in which left- and right- circularly polarized light experience different refractive indices, $n_L \neq n_R$, and circular dichroism, in which a chiral material exhibits differential molar absorptivities to left- and right- circularly polarized light, $\varepsilon_L \neq \varepsilon_R$ [10]. Circular dichroism is commonly measured with circular dichroism spectroscopy, in which the differential absorption of left- and right-circularly polarized light is measured, whereas circular birefringence, which gives rise to the rotation of linearly polarized light, is often measured through optical rotatory dispersion experiments. This differential response by chiral systems is of particular interest, because it has direct applications to device development. Chiral

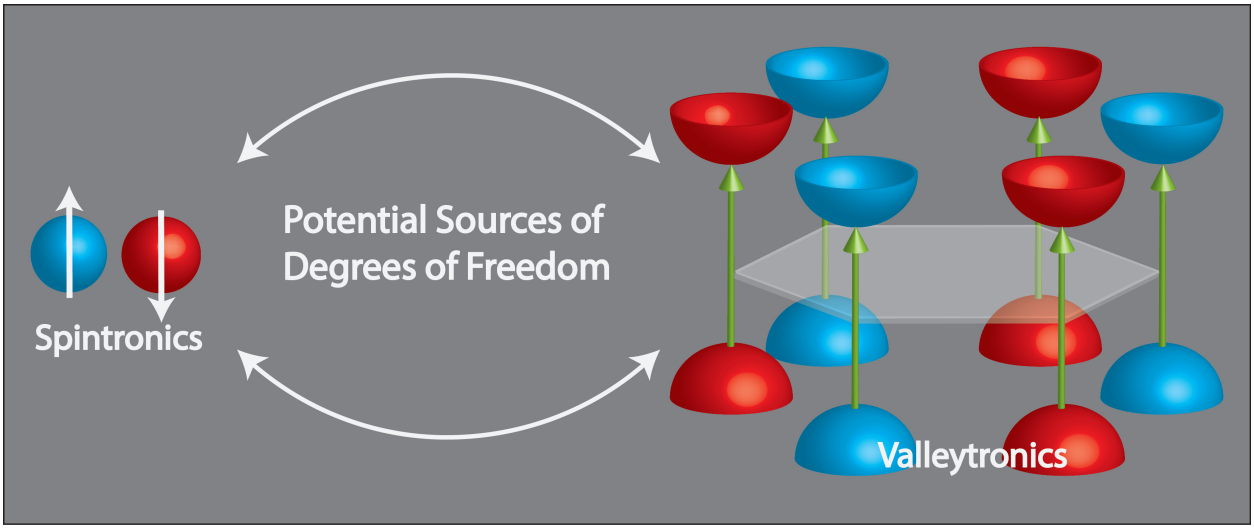

Figure 1.1: Additional degrees of freedom accessible in symmetry broken molecular systems.

materials are selectively sensitive to the spin angular momentum of light, meaning the chiral excited state can be exploited as an additional degree of freedom for decoding quantum information encoded through light's angular momentum. Harnessing additional degrees of

freedom in device development subsequently leads to the generation of smaller, more efficient devices. Chirality can also provide a route to optimizing charge transport efficiency. Recent work on organic solar cell development has shown increased efficiency in enantiopure organic semiconductors compared to racemic semiconductor designs [11–13]. In light of these developments, it is clear that the efficient development of chiral quantum technologies depends on the mechanistic understanding of the processes that underpin the excited state dynamics in chiral systems.

The dynamics that follow optical excitation of chiral materials to a higher-energy state occur on ultrafast timescales. The dominant excited-state phenomena directly dictate the practical technological applications a chiral material can support. Within femtoseconds to picoseconds, processes such as energy transfer, excited state and ground state coupling, and vibrational coherences have begun. The dynamics and timescales of these processes are directly linked to the structure of the chiral material. Understanding how chiral structure shapes these excited-state properties is therefore essential for engineering materials that can selectively prepare, transmit, or read out polarization-dependent optical information. These factors motivate the need for ultrafast spectroscopic techniques to characterize the Hamiltonian of materials that exploit chiral states for the detection of quantum-encoded information.

1.2 Spectroscopic Probes of Molecular Chirality and Measurement Limitations

To determine whether a signal reports on chirality, the parity of the measured observable can be analyzed. Parity becomes especially helpful when discussing nonlinear optical activity, which is the main theoretical concept of this thesis.

The parity operator represents the symmetry operation that performs a spatial inversion on a system. This can be visualized by inverting all coordinates within a system through

the origin, which negates the system's original coordinates, $q(a, b, c)$, following the parity operation, $q(-a, -b, -c)$ [14]. If a system is achiral, its parity-inverted image is superimposable on the original (up to any rotations on the parity-inverted image), and the parity is said to be conserved. By contrast, a parity operation on a chiral molecule transforms it into its enantiomer. Similarly, parity can be used on physical quantities that contribute to an optical signal, in order to classify that signal as being sensitive or insensitive to chirality. If the physical quantity is unchanged by the parity operator, it is parity-even, whereas if the quantity changes sign, it is parity-odd [14]. To measure a chiral signal, two conditions need to hold simultaneously: the system must be chiral, and the measured observable must be parity-odd. These principles can be summarized as follows: parity-even measurements yield identical signals for two enantiomers, whereas parity-odd measurements yield signals of opposite sign. As noted above, CD and ORD are spectroscopic techniques sensitive to molecular chirality, so the quantity they measure is parity-odd; however, they lack any temporal resolution needed to measure ultrafast photophysics.

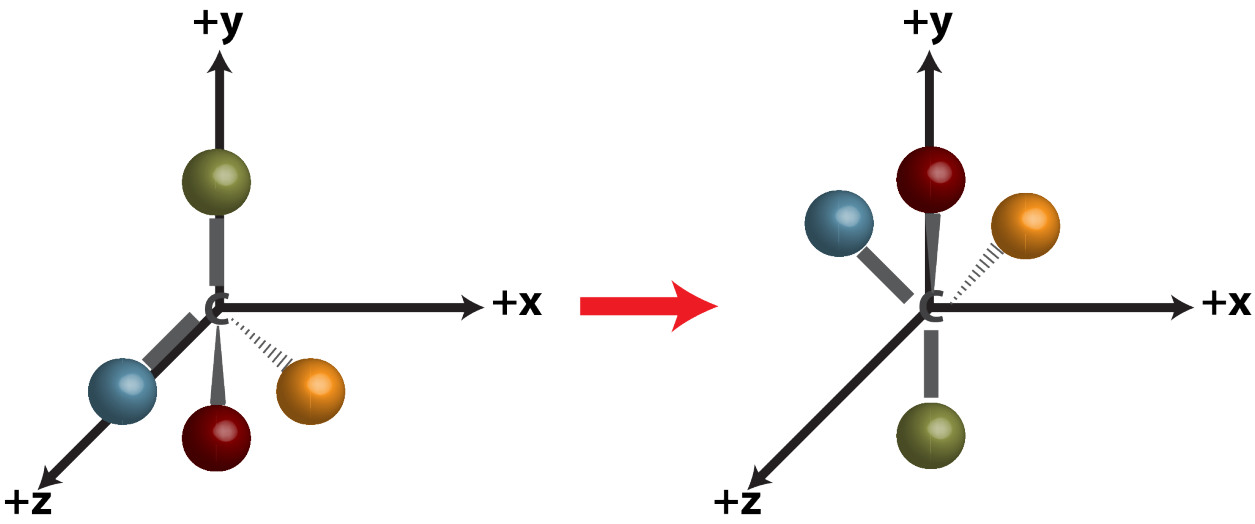

Figure 1.2: Visual depiction of a parity transformation. A parity transformation results in inverted molecular coordinates relative to the original molecule $q(a, b, c)$ to $q(-a, -b, -c)$. The inversion center of the molecule shown corresponds to the coordinate grid's origin for the illustrated transformation.

Time resolved optical activity has historically been used to extend our understanding of static chirality into the dynamic regime by measuring the time evolution of the chiral optical response. The experimental setup mimics that of a conventional transient absorption (TA) measurement. A pump pulse excites the molecular system into an excited-state population, then a probe pulse interrogates the system's evolution at varying time delays, known as waiting time, between the initial pump excitation and the probe pulse. The emitted signal interferes with the probe pulse and is detected in the frequency domain. The main experimental difference between achiral and chiral transient absorption experiments lies in the electric field polarization scheme employed. Time-resolved optical spectroscopy experiments can be categorized as either differential absorption or ellipsometry techniques [15]. Differential absorption techniques are the analog to steady-state circular dichroism measurements. In these, the pump pulse is typically linearly polarized and the probe pulse is circularly polarized. A photoelastic modulator (PEM) rapidly switches the probe polarization between left- and right- circular polarization. The difference between the left- and right- circularly polarized signals is taken to yield a differential absorption signal [16].

Despite large strides in the resolution of chiral transient absorption measurements, the lack of excitation-energy resolution prevents the formation of a complete excited-state picture, one in which the signal amplitude can be correlated between the excitation and emission energies to reveal the coupling between chiral states [15, 17–20]. Two dimensional electronic spectroscopy measures the same signal as a transient absorption measurement, but with an additional excitation energy axis resolved. The experiment yields excitation-emission energy correlation maps that illustrate the evolution of the excited states as a function of time. Experimentally, a second time delay, known as coherence time, is introduced between the pump pulse and a second pump pulse. This delay between the two pump pulses is scanned, and a Fourier transform over the coherence time in post-processing yields the excitation-energy axis. A major drawback of 2DES is the added acquisition time required; in exchange, 2DES

reveals a clearer roadmap to excited state disentanglement by resolving direct couplings between states. The chiral analog to 2DES has been extensively discussed theoretically, however experimental limitations have prevented the routine collection of chiral 2DES data.

The achiral 2DES signal is already a weak, perturbative response, which makes the chiral 2DES experiment especially challenging given that the chiral signal is two to five orders of magnitude smaller than the achiral signal [21–24]. Any imperfection in the polarization or detection scheme will allow the dominant achiral signal to obscure the chiral response. The left-circularly polarized signal and right-circularly polarized signals consist predominantly of the achiral signal, and any failure to perfectly subtract the two prevents accurate isolation of the chiral signal. Consequently, chiral difference measurements are especially prone to achiral signal contamination resulting from laser instability [21]. Other common sources of error in chiral measurements include strain-induced birefringence, pump-induced artifacts, linear dichroism, linear birefringence, and polarization impurities [16]. These compounded effects make the chiral 2DES experiment especially difficult. The measurement has been performed experimentally on one occasion by Fidler et al., using a GRAPES detection scheme and linear polarization sequences [24]. However, the experiment has yet to be repeated, likely due to the measurement difficulty, despite the wealth of information it can provide.

In this thesis, I describe a novel chiral 2DES setup designed to enable routine chiral 2DES measurements. Experimental artifacts are mitigated through careful design of the optical layout, data acquisition and data analysis pipelines, which are detailed in Chapter 3. The instrument utilizes linear pulse polarization sequences to collect the chiral signal directly in a single experiment, removing the need to subtract very large signals acquired at different points in lab time. Both linear and circularly polarized pulse sequences have been used extensively to simulate time resolved chiral experiments [21, 25–39]. Pure pulse polarizations are obtained by exploiting the high extinction ratio naturally achieved by birefringent α-BBO crystals. Polarization impurities arising from mirror reflections are mitigated by positioning

the polarization optics immediately downstream of the sample cell. Phase drift is monitored with a second spectrometer and corrected. Polarization and phase impurities at the sample are minimized using a carefully designed low-strain sample mount. Lastly, longer camera integration times are used to increase the accumulated chiral signal and average over random noise. Together, these modifications enabled the first chiral 2DES demonstration of mirror-image signal symmetry between enantiomers.

References

(1) Pasteur, L. Memoires sur la relation qui peut exister entre la forme crystalline et al composition chimique, et sur la cause de la polarization rotatoire. *Compt. rend.* **1848**, *26*, 535–538.

(2) Cowan, J. A.; Furnstahl, R. J. Origin of Chirality in the Molecules of Life. *ACS Earth and Space Chemistry* **2022**, *6*, 2575–2581.

(3) Keszthelyi, L. Origin of the homochirality of biomolecules. *Quarterly Reviews of Biophysics* **1995**, *28*, 473–507.

(4) Bonner, W. A. In *Topics in Stereochemistry*; John Wiley & Sons, Ltd: 1988, pp 1–96.

(5) Blackmond, D. G. The origin of biological homochirality. *Philosophical Transactions of the Royal Society B: Biological Sciences* **2011**, *366*, 2878–2884.

(6) Schaller, C. P. 5.12 Chirality in Nature and Chiral Environments, [Online; accessed 2026-06-05], 2024.

(7) Franks, M. E.; Macpherson, G. R.; Figg, W. D. Thalidomide. *The Lancet* **2004**, *363*, 1802–1811.

(8) Blaschke, G. v.; Kraft, H.; Fickentscher, K.; Koehler, F. Chromatographic separation of racemic thalidomide and teratogenic activity of its enantiomers (author's transl). *Arzneimittel-forschung* **1979**, *29*, 1640–1642.

(9) Vargesson, N. Thalidomide-induced teratogenesis: History and mechanisms. *Birth Defects Research Part C: Embryo Today: Reviews* **2015**, *105*, 140–156.

(10) Cho, M. *Two-Dimensional Optical Spectroscopy*; CRC Press: 2009.

(11) Chen, M.; Li, J.; Jiao, X.; Yang, X.; Wu, W.; McNeill, C. R.; Gao, X. Enantiopure versus racemic naphthalene diimide-based n-type organic semiconductors: effect on charge transport. *J. Mater. Chem. C* **2019**, *7*, 2659–2665.

(12) Josse, P.; Favereau, L.; Shen, C.; Dabos-Seignon, S.; Blanchard, P.; Cabanetos, C.; Crassous, J. Enantiopure versus Racemic Naphthalimide End-Capped Helicenic Non-fullerene Electron Acceptors: Impact on Organic Photovoltaics Performance. *Chemistry – A European Journal* **2017**, *23*, 6277–6281.

(13) Khasbaatar, A.; Damron, A. M.; Fernando, P. S.; Williams, J. S.; Zhu, C.; Gann, E. H.; Lee, J.-H.; Birge, A.; Kim, B.; Sabury, S.; Lee, M. L.; Reynolds, J. R.; Diao, Y. Lyotropic Liquid Crystal Mediated Assembly of Donor Polymers Enhances Efficiency and Stability of Blade-Coated Organic Solar Cells. *Advanced Materials* **2025**, *37*, 2414632.

(14) Barron, L. D. *Molecular Light Scattering and Optical Activity*, 2nd ed.; Cambridge University Press: 2004.

(15) Trifonov, A.; Buchvarov, I.; Lohr, A.; Würthner, F.; Fiebig, T. Broadband femtosecond circular dichroism spectrometer with white-light polarization control. *Review of Scientific Instruments* **2010**, *81*.

(16) Xie, X.; Simon, J. D. Picosecond time-resolved circular dichroism spectroscopy: experimental details and applications. *Review of Scientific Instruments* **1989**, *60*, 2614–2627.

(17) Liu, H.; Ouyang, M. Chirality-driven spin dynamics and manipulation in all-inorganic chiral heterostructures. *Nature Communications* **2025**, *16*, 8382.

(18) Monti, M.; Biancorosso, L.; Coccia, E. Time-resolved circular dichroism in molecules: experimental and theoretical advances. *Molecules* **2024**, *29*, 4049.

(19) Cui, T.; Wang, X.; Pan, H.; Chen, J. Unravel excited state chirality dynamics during symmetry-breaking charge separation. *Science China Materials* **2026**, 1–7.

(20) Schirato, A.; Crotti, G.; Kim, R. M.; Lee, S. M.; Han, J. H.; Villa, A.; Ali, D.; Rizzo, A.; Maiuri, M.; Nam, K. T., et al. Broadband ultrafast self-heterodyned chiro-optical spectroscopy. *arXiv preprint arXiv:2511.10574* **2025**.

(21) Holdaway, D. I. H.; Collini, E.; Olaya-Castro, A. Isolating the chiral contribution in optical two-dimensional chiral spectroscopy using linearly polarized light. *Opt. Express* **2017**, *25*, 6383–6401.

(22) Berova, N.; Nakanishi, K.; Woody, R. W. *Circular dichroism: principles and applications*; John Wiley & Sons: 2000.

(23) Parson, W. *Modern Optical Spectroscopy: With Exercises and Examples from Biophysics and Biochemistry*; Springer Berlin Heidelberg: 2006.

(24) Fidler, A. F.; Singh, V. P.; Long, P. D.; Dahlberg, P. D.; Engel, G. S. Dynamic localization of electronic excitation in photosynthetic complexes revealed with chiral two-dimensional spectroscopy. *Nature communications* **2014**, *5*, 3286.

(25) Abramavicius, D.; Mukamel, S. Coherent third-order spectroscopic probes of molecular chirality. *The Journal of Chemical Physics* **2005**, *122*, 134305.

(26) Cho, M. Two-dimensional circularly polarized pump–probe spectroscopy. *The Journal of Chemical Physics* **2003**, *119*, 7003–7016.

(27) Choi, J.-H.; Cho, M. Nonlinear optical activity measurement spectroscopy of coupled multi-chromophore systems. *Chemical Physics* **2007**, *341*, Ultrafast Dynamics of Molecules in the Condensed Phase: Photon Echoes and Coupled Excitations, 57–70.

(28) Choi, J.-H.; Cho, M. Quadrupole contribution to the third-order optical activity spectroscopy. *The Journal of Chemical Physics* **2007**, *127*, 024507.

(29) Choi, J.-H.; Cheon, S.; Lee, H.; Cho, M. Two-dimensional nonlinear optical activity spectroscopy of coupled multi-chromophore system. *Phys. Chem. Chem. Phys.* **2008**, *10*, 3839–3856.

(30) Abramavicius, D.; Mukamel, S. Time-domain chirally-sensitive three-pulse coherent probes of vibrational excitons in proteins. *Chemical Physics* **2005**, *318*, Molecular Nanoscience, 50–70.

(31) Abramavicius, D.; Mukamel, S. Chirality-induced signals in coherent multidimensional spectroscopy of excitons. *The Journal of Chemical Physics* **2006**, *124*, 034113.

(32) Abramavicius, D.; Zhuang, W.; Mukamel, S. Probing molecular chirality via excitonic nonlinear response*. *Journal of Physics B: Atomic, Molecular and Optical Physics* **2006**, *39*, 5051.

(33) Voronine, D. V.; Abramavicius, D.; Mukamel, S. Coherent control of cross-peaks in chirality-induced two-dimensional optical signals of excitons. *The Journal of Chemical Physics* **2006**, *125*, 224504.

(34) Voronine, D. V.; Abramavicius, D.; Mukamel, S. Chirality-Based Signatures of Local Protein Environments in Two-Dimensional Optical Spectroscopy of Two Species Photosynthetic Complexes of Green Sulfur Bacteria: Simulation Study. *Biophysical Journal* **2008**, *95*, 4896–4907.

(35) Holdaway, D. I. H.; Collini, E.; Olaya-Castro, A. Coherence specific signal detection via chiral pump-probe spectroscopy. *The Journal of Chemical Physics* **2016**, *144*, 194112.

(36) Rouxel, J. R.; Rajabi, A.; Mukamel, S. Chiral Four-Wave Mixing Signals with Circularly Polarized X-ray Pulses. *Journal of Chemical Theory and Computation* **2020**, *16*, PMID: 32786909, 5784–5791.

(37) Liu, Z.; Jha, A.; Liang, X.-T.; Duan, H.-G. Transient chiral dynamics revealed by two-dimensional circular dichroism spectroscopy. *Phys. Rev. E* **2023**, *107*, 054119.

(38) Yang, Y.; Liu, Z.; Zheng, F.; Zhang, P.; He, H.; Jha, A.; Duan, H.-G. Diverse Transient Chiral Dynamics in Evolutionary Distinct Photosynthetic Reaction Centers. *Journal of Chemical Theory and Computation* **2025**, *21*, PMID: 39718439, 321–332.

(39) Arpin, P. C.; Turner, D. B. Perturbative theoretical model of electronic transient circular dichroism spectroscopy of molecular aggregates. *The Journal of Chemical Physics* **2022**, *157*, 154101.

CHAPTER 2

THEORY OF NONLINEAR SPECTROSCOPY AND THE CHIRAL RESPONSE

2.1 Foundations of Light-Matter Interaction and the Linear Response

Spectroscopy provides a powerful means of probing the energetic structure and dynamical response of molecular systems. Spectroscopic observables report on the electronic structure of the system, and the dynamical processes governing its excited-state evolution.

To establish the theoretical framework that defines higher-order spectroscopic techniques, we begin with a brief introduction to light-matter interactions in the linear response regime. The following material is described in detail in standard quantum mechanics and spectroscopy textbooks [1–3].

Consider a quantum mechanical system of interest. The energetic structure of the molecular system is encoded within its Hamiltonian, $\hat{H}$. In the absence of an external radiation field, the system is described by the isolated molecular Hamiltonian, $\hat{H}_0$. The eigenstates of the system and their corresponding energies are obtained by solving the time-independent Schrödinger equation,

$$\hat{H}_0|\psi_n\rangle = E_n|\psi_n\rangle \tag{2.1}$$

where E_n denotes the energy eigenvalue associated with the nth eigenstate, $|\psi_n\rangle$.

The time-independent Schrödinger equation defines the molecular eigenstates of the isolated Hamiltonian. The time-dependent evolution of the molecular system requires explicit time dependence, which is determined by solving the time-dependent Schrödinger equation,

$$\frac{\partial}{\partial t}|\psi(t)\rangle = \frac{-i}{\hbar}\hat{H}_0|\psi(t)\rangle \tag{2.2}$$

where $|\psi(t)\rangle$ denotes the time-dependent wavefunction, where $|\psi(t)\rangle$ is a linear combination of $|\psi_n\rangle$ eigenstates [1, 3]. The solution to the time-dependent Schrödinger equation in the absence of an external field is given by

$$|\Psi(t)\rangle = \sum_n c_n e^{-iE_n t/\hbar} |\psi_n\rangle. \tag{2.3}$$

where c_n are the time-independent eigenstate coefficients [3].

During the interaction with an external laser field, the Hamiltonian of the system is time dependent. The total Hamiltonian of the molecular system, $\hat{H}$, is then expressed as,

$$\hat{H} = \hat{H}_0 + \hat{W}(t) \tag{2.4}$$

where, $\hat{H}_0$ is still the time independent molecular Hamiltonian, but the total Hamiltonian now includes the term, $\hat{W}(t)$, which gives the time-dependence of the light-matter interaction and is treated perturbatively. The incident radiation is coupled to the molecular system through the interaction between the incident radiation field and the molecular system transition dipole by

$$\hat{W}(t) = -\hat{\mu} E(t) \tag{2.5}$$

where $\hat{\mu}$ is the molecule's electric transition dipole. We adopt a semiclassical treatment of the light-matter interaction in which the electromagnetic field is treated classically, while the molecular system is treated quantum mechanically. The incident electric field is expressed as a time dependent plane wave,

$$E(t) = E^{'}(t) cos(\tilde{\mathbf{k}} \cdot \tilde{\mathbf{r}} - \omega t + \phi) \tag{2.6}$$

which may also be written in an equivalent complex form as

$$E(t) = \frac{1}{2}E^{'}(t)(e^{+i(\tilde{\mathbf{k}}\cdot\tilde{\mathbf{r}}-\omega t+\phi)} + e^{-i(\tilde{\mathbf{k}}\cdot\tilde{\mathbf{r}}-\omega t+\phi)}) \tag{2.7}$$

where the wavevector, $\tilde{\mathbf{k}}$, describes the fields propagation direction, ω is the carrier frequency, ϕ is the carrier phase, and $E^{'}(t)$ is the pulse envelope [3].

During the pulse interaction, the coefficients in Equation 2.3 are now time dependent. The time dependence of the coefficients is solved through the time-dependent Schrödinger equation [3].

$$\frac{\partial}{\partial t}c_m(t) = -\frac{i}{\hbar}\sum_n c_n(t)e^{-i(E_n-E_m)t/\hbar}\langle m|\hat{W}(t)|n\rangle. \tag{2.8}$$

Physically, interaction of the electric field with the molecular system drives the redistribution of charge density within the system, referred to as the macroscopic polarization, $P(t)$. The macroscopic polarization acts as a source that emits an electric field, E_{sig}, as governed by Maxwell's equations [1, 3]. This emitted signal serves as the experimental observable for spectroscopy experiments and is proportional to the 90° phase shifted macroscopic polarization,

$$E_{sig}(t) \propto iP(t) \tag{2.9}$$

The macroscopic polarization evolves in time according to the system's molecular response, $R(t)$, which is ultimately what we are interested in. We are operating within the weak-field approximation (linear response theory), in which the macroscopic polarization scales linearly with the electric field strength [1]. Thus, the time evolution of the macroscopic polarization is defined by the convolution between the incident electric field and system response which for linear spectroscopy is given by

$$P^{(1)}(t) \propto \int_0^{\infty} R^{(1)}(\tau)\, E(t-\tau)\, d\tau \tag{2.10}$$

We can alternatively define the macroscopic polarization through the expectation value of the system's transition dipole [3].

$$P(t) = \langle \psi(t) | \hat{\mu} | \psi(t) \rangle = \langle \mu \rangle \tag{2.11}$$

The formalism discussed within this chapter so far has existed within the ordinary quantum mechanical Hilbert space, which uses vector notation to define the wavefunction. For most spectroscopy experiments we are not probing a system that can be fully described by a single wavefunction, but we are probing a statistical average over an ensemble of molecules. From here on, we will express the system's evolution within Liouville-space, which enables the clean representation of statistical ensembles. In Liouville space, instead of monitoring the evolution of the wavefunction, the evolution of the density matrix, ρ, is monitored [1].

Formally, a system that cannot be defined by a single wavefunction is in a mixed state and $\mathrm{Tr}(\rho^2) < 1$. In contrast, a system that can be completely described by a wavefunction is in a pure state, and $\mathrm{Tr}(\rho^2) = 1$. Additional density matrix requirements are detailed elsewhere [1, 3]. Systems probed by spectroscopy experiments are typically in a mixed state, represented by a statistical ensemble of wavefunctions given by

$$\rho = \sum_k P_k \left| \psi_k(t) \right\rangle \left\langle \psi_k(t) \right| \tag{2.12}$$

where P_k is the probability of the system being in state, $|\psi_k(t)\rangle$. Density matrices provide a clean formalism for expressing a system's coherences and populations which is especially useful for mixed states. The time evolution of the density matrix is described by the Liouville-von Neumann equation.

$$\frac{d}{dt}\rho = -\frac{i}{\hbar}[\hat{H}, \rho] \tag{2.13}$$

Recall the measurable observable is dependent on the generated macroscopic polarization.

We can write the macroscopic polarization as the trace of the density matrix and the dipole moment operator, $\hat{\mu}$.

$$P(t) = \mathrm{Tr}(\hat{\mu}\rho(t)) \tag{2.14}$$

2.2 Third-Order Nonlinear Response and Spectroscopy

We will now extend our picture of spectroscopy to nonlinear measurements, which monitors the molecular system's evolution through multiple electric field interactions.

The macroscopic polarization can be expanded according to the power-law dependence to n^{th} order in the field given as $P^{(n)}$. The previous section focused on first order optical measurements, in which the polarization is described by the linear polarization, P_L or $P^{(1)}$. Subsequent interactions to n^{th} order that increases with the number of field interactions. As shown by Mukamel [1] an nth order macroscopic polarization is given by

$$P(t) = P^{(1)} + P^{(2)} + P^{(3)} + ... = P_L + P_{NL} \tag{2.15}$$

Similarly, the expansion of the density matrix to higher order interactions is expressed by

$$\rho(t) = \rho^{(1)} + \rho^{(2)} + \rho^{(3)} + ... = \rho_L + \rho_{NL} \tag{2.16}$$

where ρ_L and P_L describe the first-order linear measurements, and all higher order measurements are described by ρ_{NL} and P_{NL}.

As introduced in the previous section, the macroscopic polarization is a convolution between the material's response function and the incident radiation shown in Equation 2.10. The general expression for macroscopic polarization to n^{th} order in the external field is given

by,

$$P^{(n)}(t) = \int_0^\infty dt_n \int_0^\infty dt_{n-1} \cdots \int_0^\infty dt_1 \\ E(t-t_n)\, E(t-t_n-t_{n-1}) \cdots E(t-t_n-\cdots-t_1)\, R^{(n)}(t_n, \cdots, t_1) \tag{2.17}$$

where the nth order response function is given by

$$R^{(n)}(t_n, \cdots, t_1) = -\left(-\frac{i}{\hbar}\right)^n \Big\langle \hat{\mu}(t_n + \cdots + t_1) \big[\hat{\mu}(t_{n-1} + \cdots + t_1), \\ \cdots \big[\hat{\mu}(0), \rho(-\infty)\big] \cdots \big] \Big\rangle. \tag{2.18}$$

where the time values, t_i in both expressions correspond to the time intervals between the electric fields. The details surrounding the expansion are detailed elsewhere [3]. The 2DES and TA experiments described in this thesis are both third-order experiments. The third-order macroscopic polarization and response functions are given by Equations 2.19 and 2.20, respectively [3].

$$P^{(3)}(t) \propto \int_0^\infty dt_3 \int_0^\infty dt_2 \int_0^\infty dt_1 \; E_3(t-t_3)\, E_2(t-t_3-t_2) \\ \cdot E_1(t-t_3-t_2-t_1)\, R^{(3)}(t_3, t_2, t_1) \tag{2.19}$$

$$R^{(3)}(t_3, t_2, t_1) \propto -i \, \langle \hat{\mu}(t_3+t_2+t_1) \, [\hat{\mu}(t_2+t_1), [\hat{\mu}(t_1), [\hat{\mu}(0), \rho(-\infty)]]] \rangle \tag{2.20}$$

The evolution of the density matrix can be visualized using double-sided Feynman diagrams, which provide a compact way to track the state of the system in higher-order spectroscopy experiments. These diagrams graphically represent the sequence of excitation and emission events induced by interactions between the density matrix and the external electric fields.

An example is shown in Figure 2.1, which presents representative Feynman diagrams for a 2DES experiment. Time increases from the bottom to the top of the diagram, which is indicated by the two vertical lines sandwiching the diagram. The diagonal arrows represent the external field interactions with the density matrix, which occur at each point where the horizontal and vertical rungs intersect. Both the position and direction of each arrow carry physical meaning.

Each arrow encodes three main pieces of information. First, the side of the diagram on which the arrow appears indicates whether the interaction acts on the ket or bra side of the density matrix. The number of bra side interactions, given by n, then determines the sign of the Feynman diagram and corresponding emitted signal, $(-1)^n$. Second, the direction of the arrow relative to the Feynman diagram indicates whether the interaction corresponds to an absorption or emission event. For example, an arrow pointing towards the ket side of a ground state density matrix element, $|\mathrm{g}\rangle\langle\mathrm{g}|$, promotes the ket to an excited state, such as $|\mathrm{e}_1\rangle\langle\mathrm{g}|$. Third, the absolute direction of the arrow (left or right) identifies the electric field component involved in the interaction. The interacting field for an arrow pointing left and right is proportional to $E^*(t) = e^{+i(\tilde{\mathbf{k}}\cdot\tilde{\mathbf{r}}-\omega t+\phi)}$ and $E(t) = e^{-i(\tilde{\mathbf{k}}\cdot\tilde{\mathbf{r}}-\omega t+\phi)}$, respectively.

After each electric field interaction, the density matrix evolves during the time intervals marked between the horizontal rungs. In a 2DES experiment, the third-order response is generated by three interactions with external fields, separated by three time intervals, t_1, t_2, and t_3. These intervals correspond to the delay between the first and second pump interactions, the delay between the second pump interaction and the probe interaction, and the time between the probe interaction and the emission of the signal field, respectively.

The ket-bra notation shown between the ladder rungs identifies the density matrix element evolving during each time interval. This notation indicates whether the system evolves as a coherence or as a population during a given time period. During the first and third time periods, the system evolves as a coherence. During the second time interval, the system

may evolve as a population or coherence, depending on the system and specific Liouville pathway. In total, there are three general categories of Feynman pathways that contribute

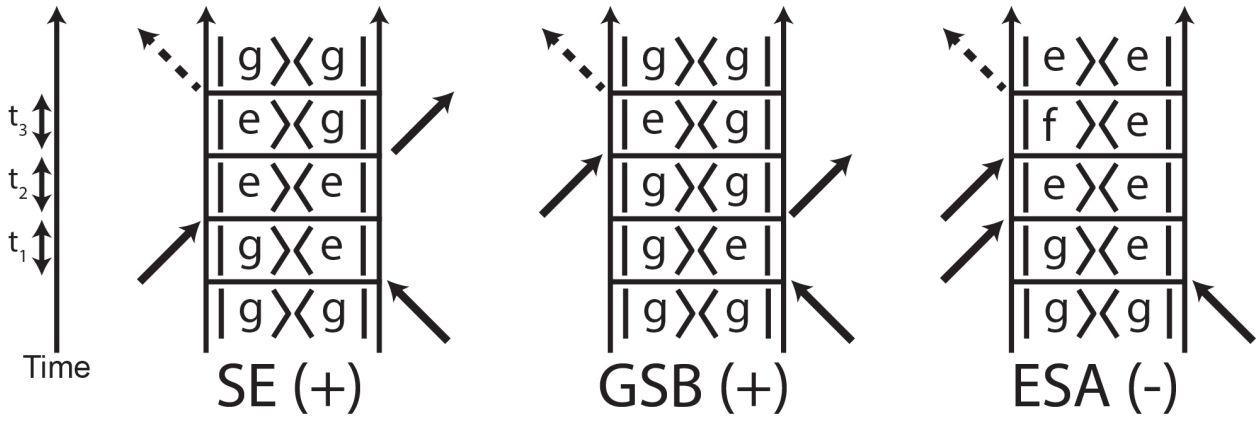

Figure 2.1: Third-order Feynman diagrams for stimulated emission (SE), ground state bleach (GSB), and excited state absorption (ESA) pathways. The experimental time intervals are indicated on the left side of the figure. The coherence time, t_1, corresponds to the interval between the two pump interactions, t_2 is the waiting time interval between the second pump interaction and the probe interaction, and t_3 represents the interval between the probe interaction and the signal emission. Only rephasing pathways are shown, although the full absorptive response contains contributions from both rephasing and non-rephasing pathways.

to the third-order signal detected in a 2DES experiment: ground state bleach (GSB), stimulated emission (SE), and excited-state absorption (ESA). An example of each Feynman diagram is shown in Figure 2.1. The sign of the signal for the ESA, GSB, and SE pathways is dependent on the difference in signal intensity detected on the camera between the pump-blocked and pump-unblocked data frames. For the GSB Feynman pathway, the first pulse excites a coherence between the ground and excited state, $|e\rangle\langle g|$. The second pulse interaction de-excites the initial coherence resulting in the system being in a ground state population, $|g\rangle\langle g|$, during t_2. If we then consider the photons hitting the camera, when the pump is blocked, there is a decrease in the amount of probe absorption by the sample compared to when the pump is unblocked. When the pump is not blocked, there is a reduction in the amount of photons absorbed by the sample, resulting in a net increase in photons hitting the detector for GSB signal contributions. This decrease in photons yields a positive

signed feature for GSB pathways. Likewise, for stimulated emission, the system exists as an excited state population during t_2. When comparing the photons on the camera at the given transition energy with and without the pump pulse present, similar to the GSB case, the photons are decreased when the pump is present, resulting in a positive signal amplitude. In contrast, ESA produces a negative signal. The density matrix exists in the excited state during waiting time, then the probe excites the sample into a coherence with a higher energy state. As a result, the absorption of the second excited state is enhanced compared to when the pump is not present.

The GSB, ESA, and SE pathways can be further categorized as rephasing or non-rephasing, depending on the relative sign of the phase evolution during t_1 and t_3. If the sign of the evolving phase is the same during t_1 and t_3, the signal is non-rephasing. Rephasing signals (also known as photon-echo signals) have opposite sign evolutions during t_1 and t_3. A comparison of a GSB rephasing and non-rephasing Feynman diagram is shown in Figure 2.2 Note, each Feynman diagram arrow is annotated by a series of wave vectors. The wave

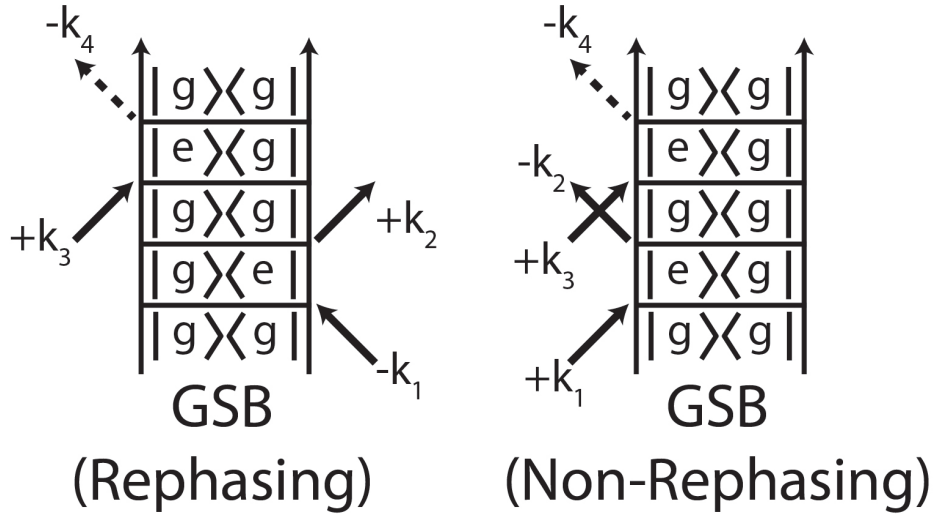

Figure 2.2: Rephasing (left) and non-rephasing (right) ground state bleach Feynman pathways.

vector subscripts reflect the chronological field ordering such that k_1, k_2, and k_3, correspond to pulses 1, 2 and 3 in the experiment respectively. The final wave vector is the emitted

signal and given by k_{sig} or k_4. The coherently generated signal emits in the direction that is the sum of all wave vectors of incident light fields,

$$k_{sig} = \sum_{i}^{n} k_i \tag{2.21}$$

[1]. For a 2DES experiment, in wave vector notation the emitted signal is given as,

$$k_{sig} = k_R + k_{NR} = \pm k_1 \mp k_2 + k_3 \tag{2.22}$$

where the total emitted signal consists of both rephasing ($-k_1 + k_2 + k_3 = k_R$) and non-rephasing ($k_1 - k_2 + k_3 = k_{NR}$).

2.3 Polarization-Controlled Pathway Selection

The polarization of the electric fields in a spectroscopy experiment is a powerful experimental control that can be leveraged to select specific components of the molecular response. By appropriate pulse polarization sequences, certain response pathways can be enhanced while others are suppressed, allowing polarization to serve as an experimental design parameter. Common polarization conditions and their associated uses are summarized in Table 2.1. The orientation of the electric field polarization relative to a system's transition dipole moment is an important consideration in spectroscopy experiments. In the electric dipole approximation, the signal scales with the dot product between the transition dipole and electric field ($\propto (\mathbf{E} \cdot \boldsymbol{\mu})$). For example, if the electric field polarization and transition dipole moment were fixed orthogonal to one another, the interaction would vanish because ($(\mathbf{E} \cdot \boldsymbol{\mu}) \propto |\mathbf{E}||\boldsymbol{\mu}| \cos(90^\circ) = 0$), assuming the dipole moment was spatially fixed. This concept extends naturally to third-order nonlinear spectroscopy, where the orientations of the electric fields and transition dipole moments associated with each field interaction dictate

the strength of a given Feynman pathway. The third-order macroscopic polarization can be written to include this orientational dependency as

$$\vec{P}^{(3)}(t) \propto -i \int_{-\infty}^{t} d\tau_3 \int_{-\infty}^{\tau_3} d\tau_2 \int_{-\infty}^{\tau_2} d\tau_1 \left\langle \vec{\mu}_\delta(t) \left[\vec{\mu}_\gamma(\tau_3) \cdot \vec{E}_c(\tau_3), \left[\vec{\mu}_\beta(\tau_2) \cdot \vec{E}_b(\tau_2), \left[\vec{\mu}_\alpha(\tau_1) \cdot \vec{E}_a(\tau_1), \rho(-\infty) \right] \right] \right] \right\rangle \quad (2.23)$$

where the subscripts on the transition dipoles $(\alpha, \beta, \gamma, \delta)$ and on incident electric field (a, b, c) indicate the potentially unique transition dipoles and electric field polarizations associated with each interaction [3].

To evaluate the polarization dependence of the signal, we need to consider the orientation of the transition dipole relative to the corresponding electric field polarization. The transition dipole orientations are defined within the molecular frame coordinate system, whereas the electric field polarizations and wave vectors are defined within a fixed laboratory frame. In a heterodyne detected experiment, or if a polarizer is used to detect the signal, the emitted signal is projected onto a fourth field, the local oscillator, E_d. The measured observable, S, is therefore proportional to,

$$S \propto (\vec{\mu}_\alpha \cdot \vec{E}_a)(\vec{\mu}_\beta \cdot \vec{E}_b)(\vec{\mu}_\gamma \cdot \vec{E}_c)(\vec{\mu}_\delta \cdot \vec{E}_d) \quad (2.24)$$

For isotropic systems, the molecules are randomly oriented in space. Therefore, the signal must be averaged over all orientations of the molecular frame relative to the fixed lab frame. This orientational average is indicated by $\langle ... \rangle$ [9]. The orientational average for a fourth-rank measurement is given by

$$S \propto \langle (\vec{\mu}_\alpha \cdot \vec{E}_a)(\vec{\mu}_\beta \cdot \vec{E}_b)(\vec{\mu}_\gamma \cdot \vec{E}_c)(\vec{\mu}_\delta \cdot \vec{E}_d) \rangle \quad (2.25)$$

The orientational component can be isolated by separating the vector directions from the

electric field amplitudes and transition dipole magnitudes as shown by

$$S = \langle(\hat{\mu}_\alpha \cdot \hat{E}_a)(\hat{\mu}_\beta \cdot \hat{E}_b)(\hat{\mu}_\gamma \cdot \hat{E}_c)(\hat{\mu}_\delta \cdot \hat{E}_d)\rangle \langle \mu_\alpha \mu_\beta \mu_\gamma \mu_\delta \rangle E_a E_b E_c E_d \tag{2.26}$$

where the first term is the orientational component of interest.

Andrews and Thirunamachandran [10] developed a succinct matrix formalism for computing the orientational averages of varying tensor ranks. For a fourth rank tensor in the electric dipole approximation, the orientational factor is given by [3]

$$\langle(\hat{\alpha}\cdot\hat{E}_a)(\hat{\beta}\cdot\hat{E}_b)(\hat{\gamma}\cdot\hat{E}_c)(\hat{\delta}\cdot\hat{E}_d)\rangle = \frac{1}{30}\begin{pmatrix}\cos\theta_{ab}\cos\theta_{cd}\\ \cos\theta_{ac}\cos\theta_{bd}\\ \cos\theta_{ad}\cos\theta_{bc}\end{pmatrix}^{\mathsf{T}}\begin{pmatrix}4 & -1 & -1\\ -1 & 4 & -1\\ -1 & -1 & 4\end{pmatrix}\begin{pmatrix}\cos\theta_{\alpha\beta}\cos\theta_{\gamma\delta}\\ \cos\theta_{\alpha\gamma}\cos\theta_{\beta\delta}\\ \cos\theta_{\alpha\delta}\cos\theta_{\beta\gamma}.\end{pmatrix} \tag{2.27}$$

Here, the first matrix contains the lab frame polarization dependence, the second matrix is system independent, and the third matrix contains the molecular frame transition dipole direction.

Alternatively, the general form for a four-wave mixing experiment, as expressed by Hochstrasser et al., can be used [11]. The expanded expression is given by [3].

$$\begin{aligned}\langle(\hat{\alpha}\cdot\hat{E}_a)(\hat{\beta}\cdot\hat{E}_b)(\hat{\gamma}\cdot\hat{E}_c)(\hat{\delta}\cdot\hat{E}_d)\rangle = \\ \frac{1}{30}\big\{&\cos\theta_{\alpha\beta}\cos\theta_{\gamma\delta}\,(4\cos\theta_{ab}\cos\theta_{cd}-\cos\theta_{ac}\cos\theta_{bd}-\cos\theta_{ad}\cos\theta_{bc})\\ &+\cos\theta_{\alpha\gamma}\cos\theta_{\beta\delta}\,(4\cos\theta_{ac}\cos\theta_{bd}-\cos\theta_{ab}\cos\theta_{cd}-\cos\theta_{ad}\cos\theta_{bc})\\ &+\cos\theta_{\alpha\delta}\cos\theta_{\beta\gamma}\,(4\cos\theta_{ad}\cos\theta_{bc}-\cos\theta_{ab}\cos\theta_{cd}-\cos\theta_{ac}\cos\theta_{bd})\,\big\}\end{aligned} \tag{2.28}$$

The pathway dependence associated with different polarization sequences has been summarized by Hochstrasser et al. [11]. For example, a diagonal feature resulting from four interactions with the same transition dipole is weighted by 1/5 under all-parallel XXXX

polarization conditions, and 1/15 under $XXYY$ polarization conditions [11].

Table 2.1: Common dipolar polarization conditions that have been historically implemented to isolate Feynman pathways in 2DES and TA experiments.

Polarization Condition	**Description**
(0°,0°,0°,0°) "All Parallel"	Benchmark condition with strong diagonal features that may obscure weak cross peaks.
(45°,45°,90°,0°) "Background free"	Suppresses the large probe background inherent to the pump-probe geometry [4].
(45°,−45°,90°,0°) "Cross-Polarized"	Suppresses diagonal pathways, (*iiii*), enhancing sensitivity to weak cross-peaks [5]. Reveals diagonal peaks arising from ultrafast coherence transfer [6].
(−60°,60°,0°,0°)	An additional cross-peak specific condition that suppresses diagonal pathways [5].
(0°,0°,+60°,−60°)	Pump-probe geometry analogue of cross peak specific pulse sequence,used for TA and 2DES measurements at $t_2 = 0$ [7].
(0°,0°,+$\theta(t_2)$,−$\theta(t_2)$)	Pump-probe geometry cross peak specific pulse sequence for $t_2 > 0$ (adjusts for rotational diffusion mediated anisotropy) [7].
(0°,0°,90°,90°) "Perpendicular"	Used in conjunction with (0°,0°,0°,0°) to extract anisotropy dynamics.
(54.7°,54.7°,0°,0°) "Magic Angle"	Removes decay contributions arising from rotational diffusion [8].

2.4 Chiral Response: Going Beyond the Dipole Approximation

In the previous section, the dipole approximation was used to describe the dominant contributions to the molecular response. Within this approximation, only terms that are zeroth order in wavevector are retained. Higher order contributions, such as wavevector dependent terms arising from the spatial variation of the electric field phase across the molecule, are neglected [9, 12]. Terms first-order in wavevector stem from the magnetic dipole-magnetic field and electric quadrupole-electric field interactions and are central to the chiroptical response. As such, they are crucial to the description of chiral nonlinear spectroscopy.

For many measurements on chiral systems, the dipole approximation remains appropriate because the chiral response is typically 2-3 orders of magnitude smaller than the dominant dipolar response [2]. As a result, direct measurement of the chiral signal is experimentally difficult and requires suppression of the dominant electric dipole response. Fortunately, specific polarization conditions can suppress the achiral electric dipole response and isolate the chiral signal contributions. This section provides a general overview of the theory underlying chiral nonlinear spectroscopy. The theoretical formalisms for nonlinear chiral spectroscopy were developed by Abramavicius, Mukamel et al. [9, 12–14], and by Cho and Choi et al. [15, 16]. The treatment in this section predominantly follows the formalism presented by Cho et al. [2].

Let us begin with the radiation-matter interaction Hamiltonian. Under the dipole approximation, the interaction Hamiltonian is constrained to the lowest order interaction between the molecular electric dipole and the electric field, given by $-\boldsymbol{\mu} \cdot \mathbf{E}(\mathbf{r}, t)$. Beyond the dipole approximation, the interaction Hamiltonian is expanded to include magnetic dipole-magnetic field and electric quadrupole-electric field interactions,

$$H_{rad-matter} = -\boldsymbol{\mu} \cdot \mathbf{E}(\mathbf{r}, t) - \mathbf{m} \cdot \mathbf{B}(\mathbf{r}, t) - (1/2)\mathbf{Q}\nabla\mathbf{E} : (\mathbf{r}, t) \tag{2.29}$$

where $\boldsymbol{\mu}$ is the electric dipole moment, $\mathbf{m}$ is the magnetic dipole, $\mathbf{B}$ is the magnetic field, and $\mathbf{Q}$ is the electric quadrupole tensor [2]. The radiation-matter interaction Hamiltonian can alternatively be written in terms of the optical wavevector, which will be useful for the orientational averaging description later in this section [2].

$$\begin{aligned} H_{rad-matter} = &- \{\boldsymbol{\mu} + (\mathbf{m} \times \hat{\mathbf{k}}) + (i/2)\mathbf{k} \cdot \mathbf{Q}\} \cdot \mathbf{e}E(t)e^{i\mathbf{k}\cdot\mathbf{r}-i\omega t} \\ &- \{\boldsymbol{\mu} + (\mathbf{m} \times \hat{\mathbf{k}}) - (i/2)\mathbf{k} \cdot \mathbf{Q}\} \cdot \mathbf{e}E(t)e^{-i\mathbf{k}\cdot\mathbf{r}+i\omega t} \end{aligned} \tag{2.30}$$

Experimentally, the first-order wavevector dependent terms are isolated by taking the difference between signals measured under left- and right- circularly polarized field conditions. The electric dipole signal is identical under left- and right- circular polarization conditions and will therefore vanish in the subtraction. The general chiral signal is defined by

$$\Delta S = S_L - S_R \tag{2.31}$$

where the L and R subscripts refer to the polarization of the incident radiation, and ΔS is the measured signal [2]. For linear chiral measurements, this concept directly translates into measuring the differential absorption of left and right circularly polarized light by a chiral sample. For nonlinear measurements, there is a wider range of experiments that can be used to selectively measure a system's chirality. Any *nth* order measurement of optical activity can simply be performed by substituting one linearly polarized field with left- and then right- circular polarization and taking the difference as shown by

$$\Delta S^{(n)}_{l_1 l_2,\ldots,l_{j-1},C,l_{j+1},\ldots,l_n} = \Delta S^{(n)}_{l_1 l_2,\ldots,l_{j-1},L,l_{j+1},\ldots,l_n} - S^{(n)}_{l_1 l_2,\ldots,l_{j-1},R,l_{j+1},\ldots,l_n} \tag{2.32}$$

where the jth interaction is the interaction with circular polarization [2]. We are interested in the third-order nonlinear response for a 2DES experiment, in which any of the four fields can be substituted with left and then right circularly polarized light.

Circularly polarized light can be written as a linear combination of linearly polarized light with a phase difference,

$$\mathbf{e}_L = \frac{1}{\sqrt{2}}(\mathbf{x} + i\mathbf{y}); \qquad \mathbf{e}_R = \frac{1}{\sqrt{2}}(\mathbf{x} - i\mathbf{y}) \tag{2.33}$$

where $\mathbf{e}_L$ and $\mathbf{e}_R$ represent electric field vectors that are left and right circularly polarized, respectively [2]. Because of this facile basis transformation between circular and linear electric field polarizations, one can similarly perform chiral experiments that are sensitive to the chiral response using linear polarization. For a four-wave mixing measurement under collinear beam geometry, the possible substitutions are given by

$$\Delta S_{x,x,x,C} = \Delta S_{x,x,x,L} - \Delta S_{x,x,x,R} = \sqrt{2} i S_{x,x,x,y} \tag{2.34}$$

$$\Delta S_{x,x,C,x} = \Delta S_{x,x,L,x} - \Delta S_{x,x,R,x} = \sqrt{2} i S_{x,x,y,x} \tag{2.35}$$

$$\Delta S_{x,C,x,x} = \Delta S_{x,L,x,x} - \Delta S_{x,R,x,x} = \sqrt{2} i S_{x,y,x,x} \tag{2.36}$$

$$\Delta S_{C,x,x,x} = \Delta S_{L,x,x,x} - \Delta S_{R,x,x,x} = \sqrt{2} i S_{y,x,x,x} \tag{2.37}$$

$$\Delta S_{y,y,x,C} = \Delta S_{y,y,x,L} - \Delta S_{y,y,x,R} = \sqrt{2} i S_{y,y,x,y} \tag{2.38}$$

$$\Delta S_{y,y,C,x} = \Delta S_{y,y,L,x} - \Delta S_{y,y,R,x} = \sqrt{2} i S_{y,y,y,x} \tag{2.39}$$

$$\Delta S_{x,C,y,y} = \Delta S_{x,L,y,y} - \Delta S_{x,R,y,y} = \sqrt{2} i S_{x,y,y,y} \tag{2.40}$$

$$\Delta S_{C,x,y,y} = \Delta S_{L,x,y,y} - \Delta S_{R,x,y,y} = \sqrt{2} i S_{y,x,y,y} \tag{2.41}$$

$$\Delta S_{x,y,y,C} = \Delta S_{x,y,y,L} - \Delta S_{x,y,y,R} = \sqrt{2} i S_{x,y,y,y} \tag{2.42}$$

$$\Delta S_{C,y,y,x} = \Delta S_{L,y,y,x} - \Delta S_{R,y,y,x} = \sqrt{2} i S_{y,y,y,x} \tag{2.43}$$

$$\Delta S_{y,x,C,y} = \Delta S_{y,x,L,y} - \Delta S_{y,x,R,y} = \sqrt{2} i S_{y,x,y,y} \tag{2.44}$$

$$\Delta S_{y,C,x,y} = \Delta S_{y,L,x,y} - \Delta S_{y,R,x,y} = \sqrt{2} i S_{y,y,x,y} \tag{2.45}$$

$$\Delta S_{x,y,C,y} = \Delta S_{x,y,L,y} - \Delta S_{x,y,R,y} = \sqrt{2} i S_{x,y,y,y} \tag{2.46}$$

$$\Delta S_{C,y,x,y} = \Delta S_{L,y,x,y} - \Delta S_{R,y,x,y} = \sqrt{2} i S_{y,y,x,y} \tag{2.47}$$

$$\Delta S_{y,x,y,C} = \Delta S_{y,x,y,L} - \Delta S_{y,x,y,R} = \sqrt{2} i S_{y,x,y,y} \tag{2.48}$$

$$\Delta S_{y,C,y,x} = \Delta S_{y,L,y,x} - \Delta S_{y,R,y,x} = \sqrt{2} i S_{y,y,y,x} \tag{2.49}$$

where the subscript, C, denotes the circular field polarization difference [2, 16]. Therefore, $XXXY$, $XXYX$, $YXXX$, and $XYXX$ linear polarization conditions can be used to isolate the chiral response without requiring the subtraction of measurements acquired with opposite circular polarization states. Out of those four signals, $XXYX$, $XYXX$, and $YXXX$ are linearly independent [14]. Using linear polarization is experimentally advantageous because it reduces the measurement time by half, and it eliminates signal contamination that arises from subtracting two very large signals that were collected at different experimental times [17].

We can express the third-order polarization of the measured signal as a power series expansion in terms of $\mathbf{m}$ and $\mathbf{Q}$

$$\mathbf{P}_{2DES}(t) = \mathbf{P}^{(0)}_{2DES}(t) + \mathbf{P}^{(1)}_{2DES}(t;m) + \mathbf{P}^{(1)}_{2DES}(t:Q) + ... \tag{2.50}$$

where the terms higher order in $\mathbf{m}$ and $\mathbf{Q}$ are orders of magnitude weaker than the terms linear in $\mathbf{m}$ and $\mathbf{Q}$ and are therefore neglected [2]. When only considering the interactions linear in $\mathbf{m}$ and $\mathbf{Q}$, the relevant signals for a chiral 2DES measurement are those in which one of the field-matter interaction terms is replaced with either the magnetic dipole-magnetic field or the electric quadrupole-electric field interaction. The other three field-matter interactions are electric dipole-electric field interactions. The tensors that are considered for a general system beyond the dipole approximation to first order in wavevec-

tor are $[\boldsymbol{\mu}_4\boldsymbol{\mu}_3\boldsymbol{\mu}_2\boldsymbol{\mu}_1]$, $[\boldsymbol{\mu}_4\boldsymbol{\mu}_3\boldsymbol{\mu}_2(\mathbf{m}_1 \times \hat{\mathbf{k}}_1)]$, $[\boldsymbol{\mu}_4\boldsymbol{\mu}_3(\mathbf{m}_2 \times \hat{\mathbf{k}}_2)\boldsymbol{\mu}_1]$, $[\boldsymbol{\mu}_4(\mathbf{m}_3 \times \hat{\mathbf{k}}_3)\boldsymbol{\mu}_2\boldsymbol{\mu}_1]$, $[(\mathbf{m}_4 \times \hat{\mathbf{k}}_4)\boldsymbol{\mu}_3\boldsymbol{\mu}_2\boldsymbol{\mu}_1]$, $[\boldsymbol{\mu}_4\boldsymbol{\mu}_3\boldsymbol{\mu}_2(\mathbf{k}_1 \cdot \mathbf{Q}_1)]$, $[\boldsymbol{\mu}_4\boldsymbol{\mu}_3(\mathbf{k}_2 \cdot \mathbf{Q}_2)\boldsymbol{\mu}_1]$, $[\boldsymbol{\mu}_4(\mathbf{k_3} \cdot \mathbf{Q}_3)\boldsymbol{\mu}_2\boldsymbol{\mu}_1]$, $[(\mathbf{k}_4 \cdot \mathbf{Q}_4)\boldsymbol{\mu}_3\boldsymbol{\mu}_2\boldsymbol{\mu}_1]$, where the subscripts denote the transitions for interactions 1-3 and the fourth field is the emitted signal that is heterodyne detected by a local oscillator field [2]. The first term, $[\boldsymbol{\mu}_4\boldsymbol{\mu}_3\boldsymbol{\mu}_2\boldsymbol{\mu}_1]$, is the contribution considered under the electric dipole approximation. The eight additional tensors listed must be considered when expanding the contribution beyond the dipole approximation to include terms linear in $\mathbf{m}$ and $\mathbf{Q}$.

The beam geometry employed in the setup discussed in Chapter 3 is in the pump-probe geometry with a small crossing angle between the pump and probe wavevectors. Because of this small angle, the beam propagation direction is approximately along a single wavevector direction, which we fix along the Z-axis in the space-fixed frame. Therefore, the cross product of the magnetic dipole and Z-wavevector is given by

$$\mathbf{m} \times \hat{\mathbf{k}} = m_Y \hat{X} - m_x \hat{Y} \tag{2.51}$$

I will now give an example calculation for determining the orientational factor of an $YXXX$ chiral polarization condition using an example detailed by Cho et al. [2]. I will limit the discussion to the magnetic dipole magnetic field interaction for brevity, so we will discuss $[\boldsymbol{\mu}_4\boldsymbol{\mu}_3\boldsymbol{\mu}_2(\mathbf{m}_1 \times \hat{\mathbf{k}}_1)]_{XXXY}$, $[\boldsymbol{\mu}_4\boldsymbol{\mu}_3(\mathbf{m}_2 \times \hat{\mathbf{k}}_2)\boldsymbol{\mu}_1]_{XXXY}$, $[\boldsymbol{\mu}_4(\mathbf{m}_3 \times \hat{\mathbf{k}}_3)\boldsymbol{\mu}_2\boldsymbol{\mu}_1]_{XXXY}$, and $[(\mathbf{m}_4 \times \hat{\mathbf{k}}_4)\boldsymbol{\mu}_3\boldsymbol{\mu}_2\boldsymbol{\mu}_1]_{XXXY}$ tensor components. The subscripts of the tensor components represent the field polarization conditions for each of the interactions. Note that here the chronological ordering of the dipoles and fields are written 4,3,2,1.

To begin, consider the contribution arising from the $[\boldsymbol{\mu}_4\boldsymbol{\mu}_3\boldsymbol{\mu}_2(\mathbf{m}_1 \times \hat{\mathbf{k}}_1)]_{XXXY}$ tensor, where the magnetic dipole is located in the first position. The transition magnetic dipole is defined as $\mathbf{m}_n = i\mathbf{M}_n$ because the matrix elements are imaginary for a real wavefunction and $\mathbf{M}_n$ is purely real. Through Equation 2.51 and the relationship between $\mathbf{M}$ and $\mathbf{m}$, the

tensor is redefined as

$$[\boldsymbol{\mu}_4\boldsymbol{\mu}_3\boldsymbol{\mu}_2(\mathbf{m}_1 \times \hat{\mathbf{k}}_1)]_{XXXY} = -i[\boldsymbol{\mu}_4\boldsymbol{\mu}_3\boldsymbol{\mu}_2\mathbf{M}_1]_{XXXX} \tag{2.52}$$

We then can perform a fourth rank rotational average using the matrix formalism in Equation 2.27. The orientational factor for a non specific Feynman pathway is therefore given by

$$\begin{aligned}&[\boldsymbol{\mu}_4\boldsymbol{\mu}_3\boldsymbol{\mu}_2(\mathbf{m}_1 \times \hat{\mathbf{k}}_1)]_{XXXY} = \\ &\frac{-i}{30}\{2(\boldsymbol{\mu}_4 \cdot \boldsymbol{\mu}_3)(\boldsymbol{\mu}_2 \cdot \mathbf{M}_1) + 2(\boldsymbol{\mu}_4 \cdot \boldsymbol{\mu}_2)(\boldsymbol{\mu}_3 \cdot \mathbf{M}_1) + 2(\boldsymbol{\mu}_4 \cdot \mathbf{M}_1)(\boldsymbol{\mu}_3 \cdot \boldsymbol{\mu}_2)\}\end{aligned} \tag{2.53}$$

As an example let's consider a ground state bleach pathway. The full orientational factor for the magnetic component of a ground state bleach pathway specified by $S^m_{XXXY}(ge, eg, ge, eg)$ is given by

$$\begin{aligned}S^m_{XXXY}(ge, eg, ge, eg) = &\left[\boldsymbol{\mu}_{ge}\,\boldsymbol{\mu}_{eg}\,\boldsymbol{\mu}_{ge}\,(\mathbf{m}_{eg} \times \hat{\mathbf{k}}_{pu})\right]_{XXXY} \\ &+ \left[\boldsymbol{\mu}_{ge}\,\boldsymbol{\mu}_{eg}\,(\mathbf{m}_{ge} \times \hat{\mathbf{k}}_{pu})\,\boldsymbol{\mu}_{eg}\right]_{XXXY} \\ &+ \left[\boldsymbol{\mu}_{ge}\,(\mathbf{m}_{eg} \times \hat{\mathbf{k}}_{pu})\,\boldsymbol{\mu}_{ge}\,\boldsymbol{\mu}_{eg}\right]_{XXXY} \\ &+ \left[(\mathbf{m}_{ge} \times \hat{\mathbf{k}}_{pu})\,\boldsymbol{\mu}_{eg}\,\boldsymbol{\mu}_{ge}\,\boldsymbol{\mu}_{eg}\right]_{XXXY} \\ = &\frac{4i}{15}\,(\boldsymbol{\mu}_{ge} \cdot \boldsymbol{\mu}_{eg})^M\,(\boldsymbol{\mu}_{ge} \cdot \mathbf{M}_{eg})^M.\end{aligned} \tag{2.54}$$

where the superscript M indicates the result is in the molecule fixed-frame. Note, the final product resembles the product of a dipole strength by a rotational strength. Under $XXYX$

polarization conditions, the orientational factor is opposite in sign as given by

$$\begin{aligned} S^{m}_{XXYX}(ge,eg,ge,eg) = & \left[\boldsymbol{\mu}_{ge}\,\boldsymbol{\mu}_{eg}\,\boldsymbol{\mu}_{ge}\,(\mathbf{m}_{eg}\times\hat{\mathbf{k}}_{pu})\right]_{XXYX} \\ & + \left[\boldsymbol{\mu}_{ge}\,\boldsymbol{\mu}_{eg}\,(\mathbf{m}_{ge}\times\hat{\mathbf{k}}_{pu})\,\boldsymbol{\mu}_{eg}\right]_{XXYX} \\ & + \left[\boldsymbol{\mu}_{ge}\,(\mathbf{m}_{eg}\times\hat{\mathbf{k}}_{pu})\,\boldsymbol{\mu}_{ge}\,\boldsymbol{\mu}_{eg}\right]_{XXYX} \\ & + \left[(\mathbf{m}_{ge}\times\hat{\mathbf{k}}_{pu})\,\boldsymbol{\mu}_{eg}\,\boldsymbol{\mu}_{ge}\,\boldsymbol{\mu}_{eg}\right]_{XXYX} \\ = & \frac{-4i}{15}\,(\boldsymbol{\mu}_{ge}\cdot\boldsymbol{\mu}_{eg})^{M}\,(\boldsymbol{\mu}_{ge}\cdot\mathbf{M}_{eg})^{M}. \end{aligned} \tag{2.55}$$

The relationship: $iM_{eg} = -iM_{ge}$ is implemented to simplify the above expressions [2]. The same treatment can be used to determine the orientational factors for the remaining Feynman pathways. For the electric quadrupole interaction a similar procedure is followed; however, a fifth rank rotational average is required. The orientational factors are further discussed in Chapter 3.3.

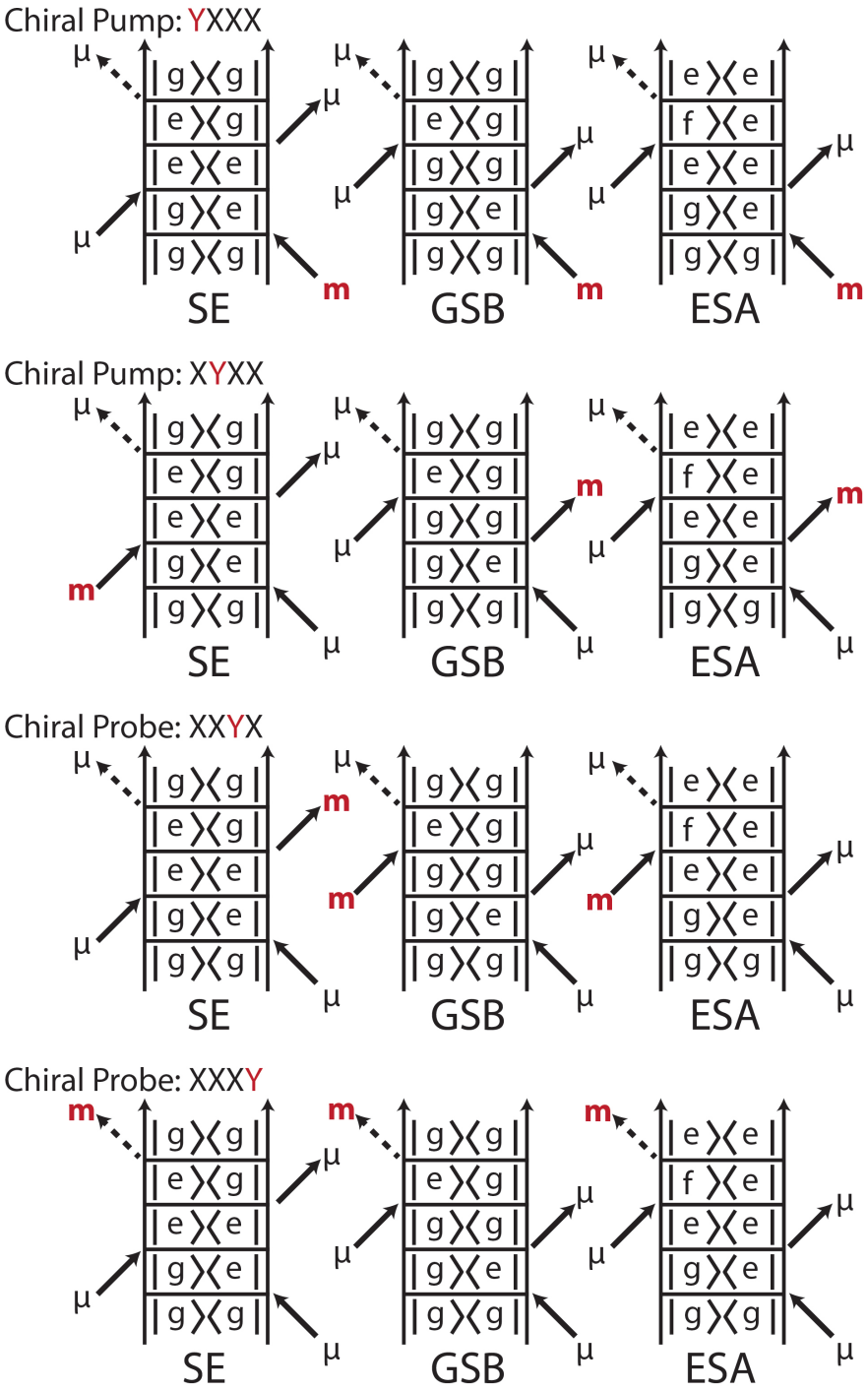

Figure 2.3: Feynman diagrams for stimulated emission (SE), ground state bleach (GSB), and excited state absorption (ESA) pathways modified for chiral polarization conditions. The first two rows show chiral pump polarization conditions and the last two rows show the chiral probe polarization conditions. The magnetic dipole magnetic field interactions are indicated by **m** [18, 19].

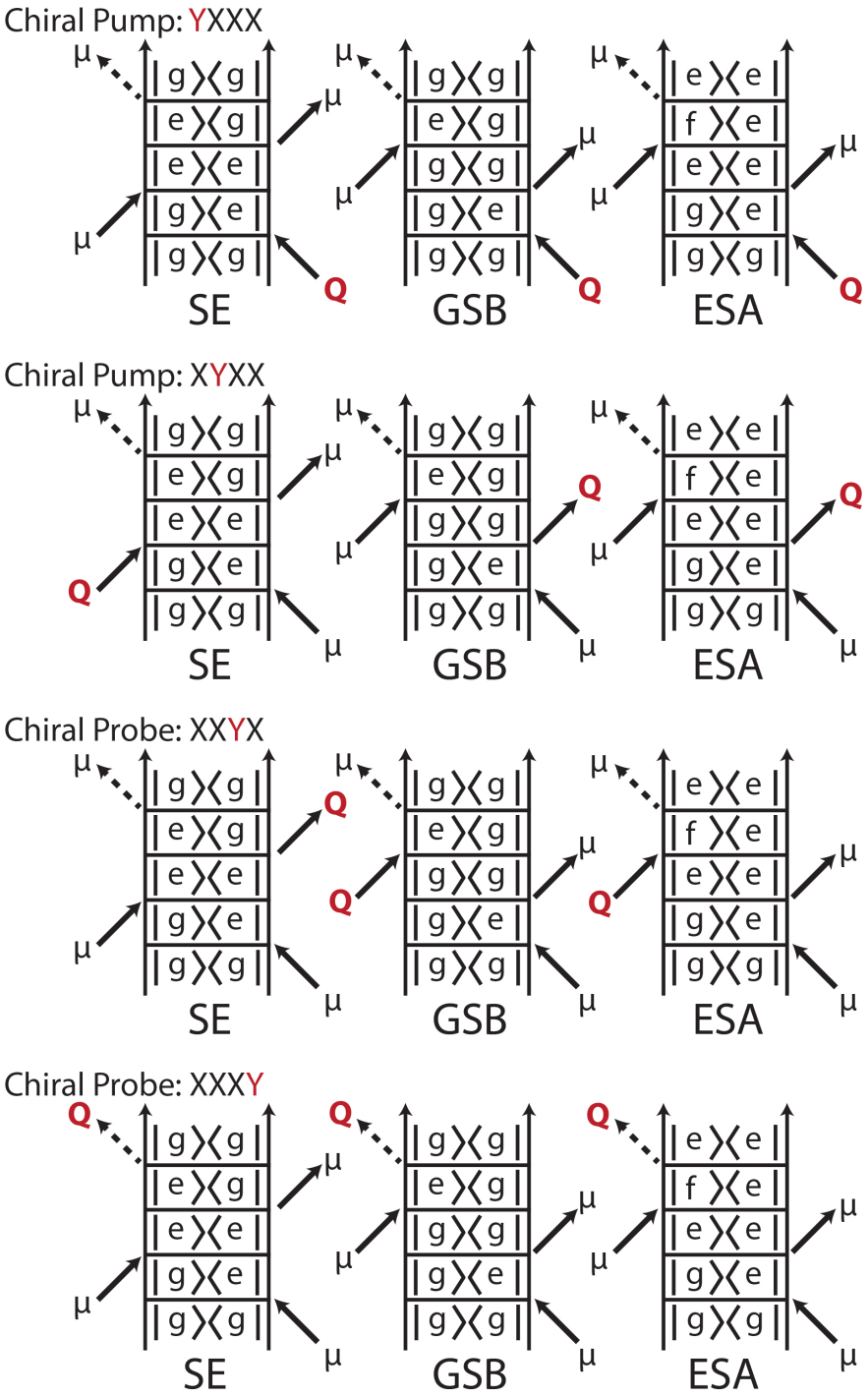

Figure 2.4: Modified version of Figure 2.3. Feynman diagrams for stimulated emission (SE), ground state bleach (GSB), and excited state absorption (ESA) pathways are shown. The first two rows show chiral pump polarization conditions and the last two rows show the chiral probe polarization conditions. The electric quadrupole electric field interactions are indicated by **Q** [18, 19].

References

(1) Mukamel, S. *Principles of Nonlinear Optical Spectroscopy*; Oxford series in optical and imaging sciences; Oxford University Press: 1995.

(2) Cho, M. *Two-Dimensional Optical Spectroscopy*; CRC Press: 2009.

(3) Hamm, P.; Zanni, M. *Concepts and Methods of 2D Infrared Spectroscopy*; Cambridge University Press: 2011.

(4) Myers, J. A.; Lewis, K. L. M.; Tekavec, P. F.; Ogilvie, J. P. Two-color two-dimensional Fourier transform electronic spectroscopy with a pulse-shaper. *Opt. Express* **2008**, *16*, 17420–17428.

(5) Zanni, M. T.; Ge, N.-H.; Kim, Y. S.; Hochstrasser, R. M. Two-dimensional IR spectroscopy can be designed to eliminate the diagonal peaks and expose only the cross-peaks needed for structure determination. *Proceedings of the National Academy of Sciences* **2001**, *98*, 11265–11270.

(6) Sardjan, A. S.; Westerman, F. P.; Ogilvie, J. P.; Jansen, T. L. C. Observation of Ultrafast Coherence Transfer and Degenerate States with Polarization-Controlled Two-Dimensional Electronic Spectroscopy. *The Journal of Physical Chemistry B* **2020**, *124*, PMID: 32990439, 9420–9427.

(7) Farrell, K. M.; Yang, N.; Zanni, M. T. A polarization scheme that resolves cross-peaks with transient absorption and eliminates diagonal peaks in 2D spectroscopy. *Proceedings of the National Academy of Sciences* **2022**, *119*, e2117398119.

(8) Fleming, G.; Morris, J.; Robinson, G. Direct observation of rotational diffusion by picosecond spectroscopy. *Chemical Physics* **1976**, *17*, 91–100.

(9) Abramavicius, D.; Mukamel, S. Coherent third-order spectroscopic probes of molecular chirality. *The Journal of Chemical Physics* **2005**, *122*, 134305.

(10) Andrews, D. L.; Thirunamachandran, T. On three-dimensional rotational averages. *The Journal of Chemical Physics* **1977**, *67*, 5026–5033.

(11) Hochstrasser, R. M. Two-dimensional IR-spectroscopy: polarization anisotropy effects. *Chemical Physics* **2001**, *266*, 273–284.

(12) Abramavicius, D.; Mukamel, S. Time-domain chirally-sensitive three-pulse coherent probes of vibrational excitons in proteins. *Chemical Physics* **2005**, *318*, Molecular Nanoscience, 50–70.

(13) Abramavicius, D.; Mukamel, S. Chirality-induced signals in coherent multidimensional spectroscopy of excitons. *The Journal of Chemical Physics* **2006**, *124*, 034113.

(14) Abramavicius, D.; Zhuang, W.; Mukamel, S. Probing molecular chirality via excitonic nonlinear response*. *Journal of Physics B: Atomic, Molecular and Optical Physics* **2006**, *39*, 5051.

(15) Choi, J.-H.; Cho, M. Nonlinear optical activity measurement spectroscopy of coupled multi-chromophore systems. *Chemical Physics* **2007**, *341*, Ultrafast Dynamics of Molecules in the Condensed Phase: Photon Echoes and Coupled Excitations, 57–70.

(16) Choi, J.-H.; Cho, M. Quadrupole contribution to the third-order optical activity spectroscopy. *The Journal of Chemical Physics* **2007**, *127*, 024507.

(17) Holdaway, D. I. H.; Collini, E.; Olaya-Castro, A. Isolating the chiral contribution in optical two-dimensional chiral spectroscopy using linearly polarized light. *Opt. Express* **2017**, *25*, 6383–6401.

(18) Cho, M. Two-dimensional circularly polarized pump–probe spectroscopy. *The Journal of Chemical Physics* **2003**, *119*, 7003–7016.

(19) Choi, J.-H.; Cheon, S.; Lee, H.; Cho, M. Two-dimensional nonlinear optical activity spectroscopy of coupled multi-chromophore system. *Phys. Chem. Chem. Phys.* **2008**, *10*, 3839–3856.

CHAPTER 3

CHIRAL TRANSIENT ABSORPTION AND TWO-DIMENSIONAL ELECTRONIC SPECTROSCOPY

3.1 Experimental Implementation

3.1.1 Optical Layout

The laser pulses used for the 2DES and TA measurements are generated by seeding a Coherent Legend Elite regenerative amplifier with an 80 MHz Coherent Micra oscillator. The 5 kHz regenerative amplifier output has a center wavelength of 800 nm and a 40 fs FWHM pulse duration. The regenerative amplifier output is focused into a 1 m long tube filled with 22 psi compressed argon gas, generating a broadband supercontinuum.

The spectrum is then further shaped according to the frequencies required to interrogate a given sample. A series of short-pass, long-pass, and bandpass filters are installed after the argon tube to shape the optical spectrum such that its carrier frequency is approximately centered relative to the optical transitions of interest. For the aggregate data discussed in Chapter 4, an 800 nm short-pass filter was used to remove most of the remaining fundamental output, followed by a 315 -710 nm bandpass filter from Thorlabs.

Special consideration must be given to the type of filter used to shape high-power laser pulses. Reflective filters are preferred in regions of the setup where the laser power is high, because absorptive filters can heat significantly, potentially leading to cracking or laser instability during an experiment. The filters, along with other transmissive optics downstream in the setup, such as wave plates and polarizers, introduce positive dispersion to the electric field. This dispersion must be compensated to yield near-transform-limited laser pulses. Therefore, the total number of transmissive optics should be minimized to avoid unnecessary dispersion, which can temporally broaden or otherwise distort the pulse.

The accumulated chirp is compensated using a series of dispersion compensating mirror (DCM) reflections, which primarily correct for second-order dispersion, in combination with a multiphoton intrapulse interference phase scan pulse shaper (MIIPS Box 640, Biophotonics Solutions) for higher-order chirp correction. There are 28 reflection pairs divided between two pairs of DCM-10 chirped mirrors, which provide -100 fs^2 of group delay dispersion (GDD) per reflection pair, and two pairs of reflections on DCM-9 chirped mirrors which provide -55 fs^2 per reflection pair [1]. Although the MIIPS can compensate a large amount of chirp independently, we have found that using it to correct excessive dispersion can introduce intensity modulations across the spectrum. Therefore, chirped mirrors are used to remove most of the second-order dispersion before fine higher-order correction with the MIIPS.

After dispersion compensation, the beam is directed into the 2D box, where the TA and 2DES experiments are performed. The 2D box begins with a 90:10 beamsplitter, which reflects 10% of the beam for the probe/LO path and transmits the remaining 90% into the pump path.

The pump beam is directed into a retroreflective delay stage, which controls the second time delay, t_2, also referred to as the waiting time or population time. This delay corresponds to the time interval between the second pump pulse and the probe. After the delay stage, the pump beam is focused through an optical chopper, which modulates the pump at half the acquisition rate of the CCD detector. The pump polarization is then rotated to 45° using a $\lambda/2$ wave plate before entering the GEMINI 2D interferometer.

The GEMINI-2D Interferometer is described in detail elsewhere [2, 3]. Briefly, the GEMINI-2D utilizes birefringent wedges to introduce a time delay between the X and Y polarization components of the incident electric field, producing a pair of phase-locked and temporally separated pulse replicas. These pulse replicas define the first time delay, known as coherence time t_1.

The time delay between the two orthogonally polarized pulse replicas depends on the

thickness of birefringent material traversed by the beam. Therefore, t_1 is scanned precisely by mechanically translating the birefringent wedges into or out of the beam path, thereby increasing or decreasing the temporal separation between the pulse replicas. Another wedge, cut along the optic axis, is translated in tandem with the delay-generating wedge. The purpose of the second wedge is to keep the glass thickness, and therefore the dispersion, constant as t_1 is scanned. A final static wedge can be manually adjusted to fine-tune the dispersion in the pump path so that it matches the dispersion in the probe path. The wedges within the GEMINI 2D are shown in Figure 3.2.

Immediately downstream of the GEMINI-2D, the pump beam passes through a sequence of polarization optics. The specific order, location, and orientation of these optics depend on the polarization conditions required for a given experiment.

Because the pump pulses are collinear, this setup can measure only polarization conditions where the pump-pulse replicas are either parallel or orthogonal to one another. After transmission through the GEMINI-2D, the pump-pulse replicas are orthogonally polarized. For polarization sequences requiring parallel pump polarizations, the orthogonal pulses first pass through a wave plate, which rotates their polarizations so that an equal amount of each pulse component is projected onto a common polarization axis by the downstream polarizer. The polarizer then defines the pump polarization angle for the experiment.

The pulses then pass through a 0.1 ND filter, which reflects a small fraction of the beams into a second spectrometer. The reflected signal is used to monitor the relative phase between the pump pulses over the course of an experiment. The transmitted pump pulses are then directed onto a 500 mm focusing mirror and aligned to overlap with the probe beam at the sample position. Immediately before the sample and after the focusing mirror, the pump beam passes through a final polarizer mounted in a modified Thorlabs precision rotation mount. This polarizer removes residual polarization impurities before the pump pulses interact with the sample.

Polarization conditions in which the two pump pulses are orthogonal require the polarizers located after the GEMINI-2D to be removed from the beam path or moved upstream of the GEMINI-2D. If a given analysis requires comparison between orthogonal and parallel pump polarization conditions, such as sequential chiral pump and chiral probe experiments, the polarizers can be placed upstream to maintain consistent dispersion between measurements. For this configuration, the polarizers are aligned to maximize pump throughput. However, for experiments that require only orthogonal pump polarizations, the two polarizers can be removed from the pump path entirely. In this case, approximately 6 mm of compensating glass can also be removed from the probe path.

The probe path begins with the 10% component reflected from the beamsplitter at the entrance of the 2DES/TA box. The probe path contains additional transmissive optics, including fused-quartz windows and a c-cut α-BBO (CASTECH), to match the dispersion accumulated by the pump pulses (primarily inside the GEMINI-2D).

An a-cut α-BBO crystal is then used to generate orthogonally polarized pulse replicas that are temporally separated by an amount determined by the crystal thickness. These pulse replicas serve as the probe and local oscillator for the 2DES and TA experiments. The polarization of an incident pulse relative to the fast and slow axes of the a-cut α-BBO determines the relative intensities of the probe and local oscillator. In our experiment, the horizontally polarized component precedes the vertically polarized component by 1.1 ps and is used as the local oscillator. The polarization of the field incident on the α-BBO crystal is first rotated with a wave plate and then purified with a polarizer aligned approximately 1° from vertical polarization, leaving most of the intensity in the probe pulse.

Similar to the pump-path, the exact order of polarization optics in the probe path differs depending on the desired polarization conditions. For polarization sequences in which the probe and local oscillator are parallel, a second polarizer is positioned just after the α-BBO crystal. This polarizer projects the probe and local oscillator onto a common polarization

axis. For polarization sequences in which the probe and local oscillator must remain orthogonally polarized, the second probe polarizer is moved upstream of the α-BBO. Placing the polarizer upstream preserves the same amount of transmissive material in the probe path when switching between measurements that require parallel and orthogonal probe/LO polarization conditions.

Downstream of the polarization optics, the probe and local oscillator are focused onto the sample cell by the same 500 mm concave mirror used to focus the pump pulses. For chiral probe polarization conditions, where a high polarization purity is required, the a-cut α-BBO crystal is instead placed immediately before the sample, after reflection from the focusing mirror. The rationale for this decision is described in Chapter 3.1.5.

After the sample, under orthogonal probe/LO polarization conditions, a Glan-Thompson polarizer is used as an analyzer to suppress the residual probe background while transmitting the horizontally polarized emitted signal. Under parallel probe/LO polarization conditions, the probe cannot be filtered out, so a neutral density filter may be installed in the probe path to prevent saturation of the detection camera.

The signal and local oscillator are then aligned into an Andor Kymera 328i spectrograph and detected with a Teledyne Dalsa Spyder3 dual line-scan camera. During data acquisition, the camera acquisition rate is set to 20 Hz, while the pump pulses are modulated at 10 Hz. This acquisition scheme produces alternating pump-unblocked and pump-blocked frames at each experimental time point. The pump-unblocked frames contain pump-induced nonlinear signal, whereas the pump-blocked frames contain non pump-induced background signals that are subtracted during processing.

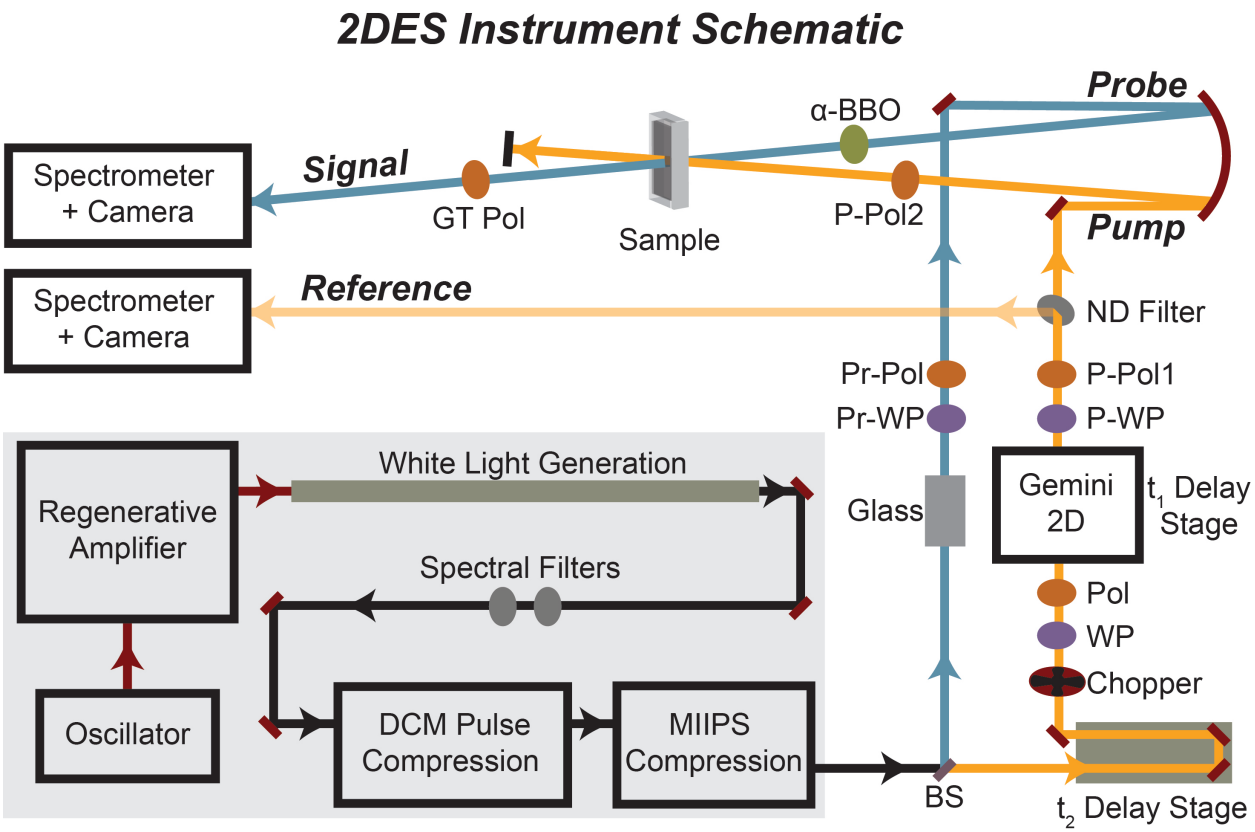

Figure 3.1: Instrument schematic for chiral probe polarization sequences. Briefly, a 5 kHz pulse train is generated by the oscillator and regenerative amplifier systems (Coherent). The 800 nm output is focused into a 22 psi argon-filled tube to generate a broadband supercontinuum, which is subsequently shaped by spectral filters. Coarse pulse compression is achieved using DCM-9 and DCM-10 chirped mirrors, and fine pulse compression is performed by the multiphoton intrapulse interference phase scan pulse shaper (MIIPS). A 90:10 beamsplitter reflects 10% of the incident beam along the probe path, while the remaining 90% is transmitted along the pump-path. Along the pump path, the beam reflects from a retroreflective delay stage, which controls the waiting time, t_2. The beam is then focused through an optical chopper that modulates the pump at 10 Hz. The pump beam is split into two phase-locked pulse replicas within the GEMINI-2D interferometer, and a portion of the pump beams are sent to a second spectrometer and camera. A series of polarization optics, including a wave plate (P-WP), a polarizer (P-Pol1) and a second polarizer (P-Pol2) are used to control the pump polarization conditions. The probe pulse transmits through glass (for dispersion matching), then through a wave plate (Pr-WP) and polarizer (Pr-Pol) which control the ratio of probe to local oscillator intensity by adjusting the polarization angle of the incident probe field relative to the axes of the alpha barium borate crystal (BBO). The BBO generates a time-separated, orthogonally polarized local oscillator that precedes the probe pulse by 1.1 ps. The probe and local oscillator pulses are then focused into the sample. The signal and local oscillator transmit through the Glan-Thompson polarizer (GT-Pol) before being directed to the spectrometer and line scan CCD camera.

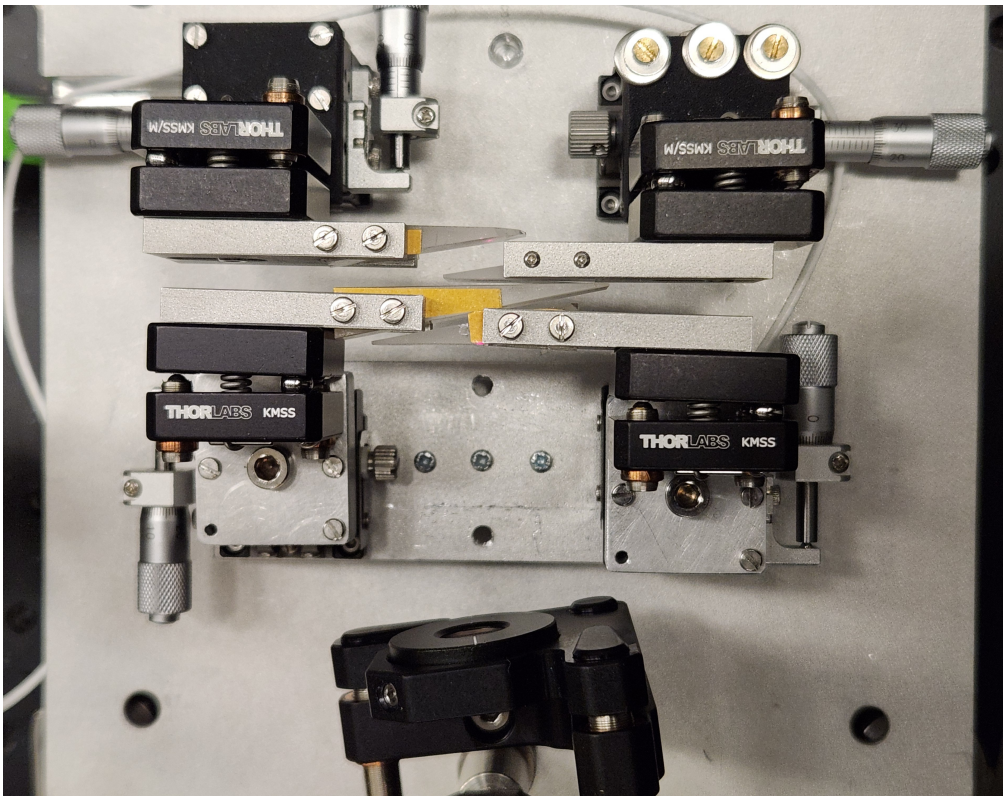

Figure 3.2: The birefringent wedge assembly within the NIREOS GEMINI-2D interferometer. The beam propagates from the bottom to the top of the image, transmitting through a polarizer oriented at 45° and then through a motorized birefringent wedge pair, in which one wedge introduces the variable temporal delay between the orthogonally polarized pump-pulse replicas and the second wedge compensates the total material thickness to maintain constant dispersion during the scan. Finally, the beam transmits through a second wedge pair, where one wedge is used to manually adjust the pump-path dispersion and the other controls the absolute time-zero position [4].

3.1.2 LO Heterodyne Detection in the Pump-Probe Geometry

The partially collinear pump-probe geometry was first theoretically described by Faeder et al. [5] and was later implemented experimentally in mid-IR [6] and IR 2D spectroscopy experiments [7]. In the pump-probe geometry, the first two pulses are collinear, such that $k_1 = k_2$, while the third interaction is provided by the probe pulse, which is collinear with the detected signal field. Because the first two pump wave vectors are equivalent, the rephasing and non rephasing contributions are emitted simultaneously into the same wave vector direction. As a result, the absorptive 2D signal can be obtained directly by scanning the positive coherence time [7].

In conventional pump-probe geometries, the probe serves as both the third field interaction and as the local oscillator for heterodyne detection, thereby preserving the signal phase [7]. This configuration contrasts with the commonly used boxCARS geometry, in which the excitation wave vectors are noncollinear. In the boxCARS geometry, the three excitation fields form the three corners of a box, and the signal is emitted in the phase-matched direction corresponding to the fourth corner, where it overlaps with a local oscillator for heterodyne detection [8].

The spatial separation of all fields in the boxCARS geometry leads to the background free detection of 2DES signals, enhancing the sensitivity to weak nonlinear signals at the added cost of additional experimental complexity. The rephasing and non-rephasing signals must be measured independently, either by reversing the temporal ordering of the first two pump interactions or by detecting the signals emitted in two distinct phase-matched directions [5, 9]. Additionally, phase stability is much lower because the noncollinear beam paths acquire an independent phase. In contrast, the pump-probe geometry has a higher phase stability because the phase acquired over collinear propagation paths cancels in the detected signal.

Although the partially collinear pump-probe geometry offers several experimental advantages, it also limits independent polarization control of the electric fields. This limitation

is particularly important for the measurement of chiral signals, $XXXY$, $XXYX$, $XYXX$, and $YXXX$.

In conventional partially collinear 2DES setups, it is not possible to measure polarization conditions in which the probe and local oscillator are orthogonal, while still preserving the signal's phase. This constraint arises because the probe pulse serves as both the third field interaction and the local oscillator. Therefore, the probe and local oscillator must have a shared polarization component.

Traditionally, this limit has been circumvented by inserting an analyzer before the detector to suppress the probe background while still allowing a small probe component to act as the local oscillator. For example, in the pulse sequence (45°, 45°, 90°, 0°), the probe is polarized at 90°, and the analyzer is set a few degrees away from 0° for heterodyning [10]. If the analyzer were set exactly to 0°, the background would be completely removed and the detected signal would be homodyne-detected. Because the detector is a square-law detector, intensity is measured and the signal phase is canceled out for homodyne detected signal.

$$I_{sig} = |E_{sig}e^{-i\omega t+i\phi}|^2 = E_{sig}e^{-i\omega t+i\phi}E^*_{sig}e^{i\omega t-i\phi} = E_{sig}E^*_{sig} \tag{3.1}$$

Signal phase cancellation prevents the differentiation of positive Liouville pathways, ground state bleach and stimulated emission, from the negative Liouville pathway, excited state absorption.

This slight offset in polarization preserves the phase of the detected signal by enabling self-heterodyne detection between the emitted signal and the small amount of probe electric field reaching the detector. However, this approach alters the measured polarization conditions. For a strict measurement of (45°, 45°, 90°, 0°), the detected signal nominally contains only XXYY and XYXY contributions. Rotating the analyzer slightly adds signal from XXXX, which is a linear combination of XYXY+XXYY+XYYX contributions [11].

For dipolar experiments, adding small amounts of other dipolar pulse sequences to the

overall detected signal is typically negligible, and this strategy remains effective at removing large probe background from the detected signal while preserving the signal phase. However, for chiral probe experiments, in which the probe and local oscillator are orthogonal, a slight polarization offset in the detected signal adds in parasitic dipolar contamination from the same XXXX polarization condition, which rapidly overwhelms the very weak chiral response. To avoid this limitation, we heterodyne-detect the chiral signal with a time-separated local oscillator.

The presented setup features an a-cut α-BBO crystal in the probe path, which generates a local oscillator pulse that is orthogonally polarized and temporally offset from the probe pulse. The a-cut α-BBO crystal is linearly birefringent, so the incident field component aligned with the fast axis of the BBO emerges from the crystal before the field component aligned with the slow axis. The time difference between the two orthogonal components depends on the thickness of the crystal; in this setup, the BBO thickness produces a 1.1 ps delay between the probe and local oscillator. A polarizer placed in front of the detector can then be used to reject the probe background while transmitting the local oscillator and emitted signal. This configuration enables phase-sensitive heterodyne detection of polarization sequences in which the probe and local oscillator are orthogonally polarized, such as XXXY and XXYX, while preserving the phase of the emitted signal.

3.1.3 Transient Absorption Measurements

The pump-probe geometry enables routine switching between 2DES and TA measurements. This capability is particularly useful when setting the chiral polarization angles with high precision, as discussed in Chapter 3.1.5. In a TA measurement, one of the two pump-pulse replicas is removed because a single pump pulse provides the two field interactions required to generate an excited-state population. Consequently, TA measurements are constrained to polarization conditions in which the two pump interactions are parallel. In conventional TA

setups, the probe also serves as both the third field interaction and the local oscillator, which constrains the third and fourth fields to parallel polarization conditions. In the described setup, however, the TA signal is heterodyne detected with a time separated local oscillator, analogous to the 2DES configuration described in the previous section. Because the LO and probe are orthogonally polarized, this configuration also enables TA measurements under polarization conditions in which the third and fourth fields are orthogonally polarized, including the chiral probe polarization conditions used in Chapter 4. Several strategies are used to switch the experimental setup between 2DES and TA measurements, as described below.

As described in the previous section, for parallel pump pulse conditions, a $\lambda/2$ wave plate and two polarizers are positioned immediately downstream of the GEMINI 2D interferometer to control the pump-pulse polarizations. The two pump-pulses are orthogonal to one another after transmitting through the Gemini 2D. For a 2DES experiment, the wave plate is aligned such that the polarizer is oriented precisely 45° relative to the two orthogonal pump polarizations, allowing both pump replicas to transmit with equal amplitude. To transition to a TA measurement, the wave plate is rotated so that either the vertically or horizontally polarized pump replica is oriented orthogonally relative to the polarizer and is therefore blocked. In practice, this adjustment is performed by minimizing pump scatter from the unwanted pulse.

To identify and suppress the unwanted pump replica, the coherence time stage is set to a large pulse separation such as 300 fs, and the waiting time stage is set to 0 fs. Then, a piece of smudged glass is placed at the sample position, where the pump and probe/LO beams spatially overlap. The glass scatters a portion of the pump light into the probe/LO detection path, creating an interferometric signal between the scattered pump pulses and LO on the data detection camera. Under the chiral probe polarization conditions, the probe pulse is filtered out by the Glan-Thompson polarizer in front of the detector.

In the data acquisition software, both the detected interferogram and its corresponding Fourier transform are monitored in real time. The peak positions in the Fourier-transformed signal indicate the temporal spacing between the pulse replicas, allowing each peak to be assigned to a specific field interference. The LO is delayed by approximately 1.1 ps relative to the probe pulse. Therefore, when both the waiting time and coherence time are set to zero, both pump pulses are separated from the LO by approximately 1.1 ps, producing a peak in the Fourier transform at 1.1 ps. For example, at a coherence time of 300 fs, one of the pump pulses will move by 300 fs (pump pulse 1), the other pump pulse remains stationary (pump pulse 2). The Fourier transform of the interferogram then produces a peak at 1.1 ps, corresponding to the interference between the stationary pump pulse and the LO, and a peak at 0.8 ps, corresponding to the interference between the LO and the pump pulse that moves in coherence time. The 0.8 ps peak is minimized by rotating the wave plate to eliminate the pump pulse that moves with coherence time. This procedure leaves a single pump pulse for the TA measurement while preserving the chiral probe detection geometry used for the corresponding 2DES experiment. If the setup is configured for a 2DES measurement using orthogonally polarized pump replicas, the polarization optics downstream of the GEMINI-2D in the pump path can either be removed from the beam path or reinstalled upstream of the GEMINI-2D. Moving these optics upstream of the GEMINI-2D is the most efficient route for collecting chiral pump and chiral probe data sets sequentially, because it preserves the pump-path dispersion.

Immediately upstream of the GEMINI-2D birefringent wedges, the pump path contains a wave plate and polarizer. Under standard 2DES conditions, the polarizer inside the GEMINI-2D is oriented at 45° relative to the axes of the birefringent wedges, producing two orthogonally polarized pump pulse replicas with equal intensity. For a TA measurement, this polarizer can be rotated to either 90° or 0°, suppressing one pulse replica while transmitting the other. The pump pulse suppression can be achieved by duplicating the procedure

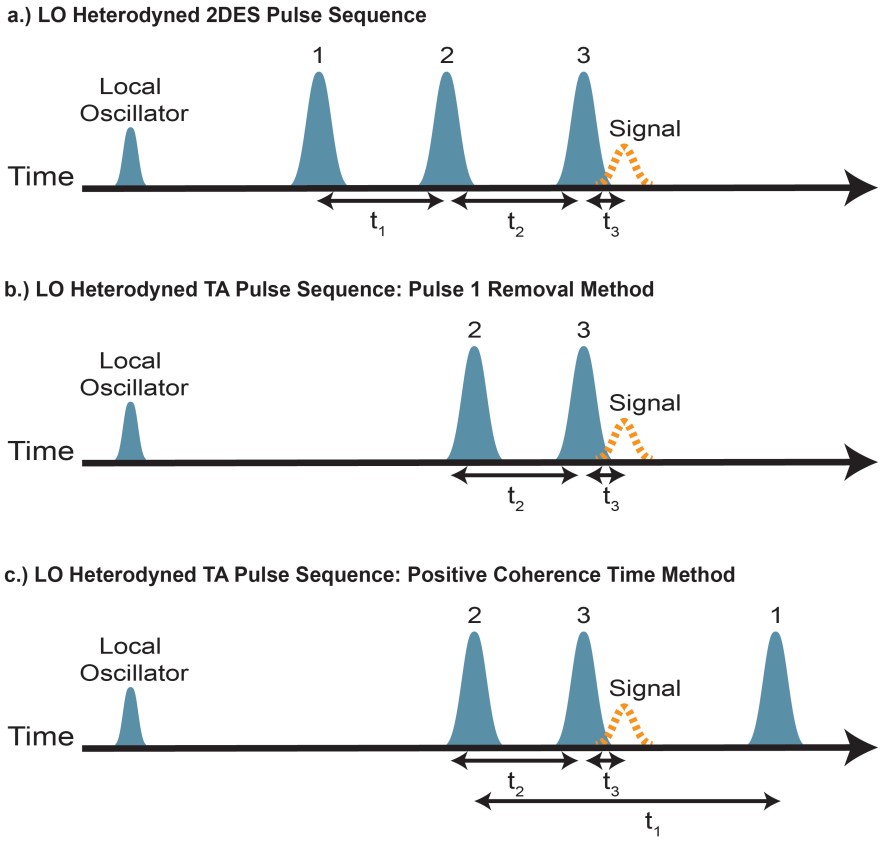

Figure 3.3: Pulse ordering for LO-heterodyne detected 2DES and TA measurements in the pump-probe geometry. (a) Standard pulse ordering for a 2DES measurement in which the LO arrives first, followed by the two pump interactions, the probe interaction, and the emitted signal. (b) One method for converting the setup to a TA measurement, in which a wave plate is rotated so that one of the orthogonally polarized pump replicas is blocked by a downstream polarizer. (c) A simpler method for acquiring an effective TA measurement, in which the coherence time is set to a sufficiently large negative delay such that only one pump replica interacts with the sample before the probe.

described above.

In addition to the method described above, which isolates a single pump replica by polarization rotation and attenuation, TA data can also be collected using a faster procedure that does not require changing the pump polarization optics. In this approach, the coherence time is set to a large negative value, as shown in Figure 3.3. At this large delay time, pump 2 arrives before the probe and can therefore generate a causal pump-probe signal. By contrast, pump pulse 1 arrives after the probe and does not contribute to the detected pump-probe

signal, because a signal emitted in the phase-matched probe direction cannot be generated before the pump excitation occurs.

This approach provides a rapid way to collect TA data, but it is limited in waiting-time range. As the waiting time is scanned, both pump replicas move relative to the probe. When the waiting time exceeds the positive coherence-time offset, pump pulse 1 also begins to arrive before the probe. At that point, both pump replicas can generate pump-probe signals, producing two overlapping TA contributions with different effective waiting-time axes. Therefore, the accessible waiting-time range must remain shorter than the maximum positive coherence time achievable.

3.1.4 Phase Stability and Measurement Techniques

One of the largest bottlenecks in 2DES measurements is the stringent phase-stability requirement. The phase detected on the camera contains contributions from each of the four field interactions in the measurement, along with the intrinsic signal phase, and can be written as

$$\Delta\phi_{measured} = -\phi_1 + \phi_2 + \phi_3 - \phi_4 + \phi_{sig} \tag{3.2}$$

where ϕ_1 through ϕ_4 are the phases of the four field interactions and ϕ_{sig} is the intrinsic signal phase [12]. The signal phase can be isolated by removing the contributions from the applied fields. Experimentally, this is accomplished by measuring the pulse phases and applying a corresponding phase correction during post-processing. The correction can be written more succinctly as

$$\phi_{corr} = -\Delta\phi_{12} + \Delta\phi_{34} \tag{3.3}$$

where $\Delta\phi_{12} = \phi_2 - \phi_1$ is the phase difference between the first and second pulses and $\Delta\phi_{34} = \phi_4 - \phi_3$ is the phase difference between the third and fourth pulses.

Adequate phase cancellation requires sub-cycle phase precision, typically around $\lambda/50$ [13,

14]. Any phase ambiguity or timing uncertainty along a Fourier-transformed axis can mix the absorptive (real) and dispersive (imaginary) components of the signal [15]. High interferometric precision is therefore required to prevent phase-induced spectral artifacts from appearing in the absorptive signal [16, 17].

In addition to the short-term phase stability required for a single Fourier transform, long term phase stability is often needed to correctly phase a complete data set, in which many waiting times are scanned and multiple data runs are collected for statistical analysis. The required duration of phase stability depends on the phase-measurement and correction procedure. For example, if the phase is measured only at the beginning of a lengthy acquisition, it must remain constant over the full acquisition period to within approximately $2\pi/50 \approx 0.13$ radians relative to the initially measured value [18].

In noncollinear beam geometries, the absolute phase is traditionally determined by performing an additional transient absorption measurement and comparing the projection of the 2DES signal onto the ω_3 axis with the transient absorption spectrum [19, 20]. However, experimental instability can cause the accumulated phase to drift significantly over the duration of a 2DES experiment [17]. Noncollinear beam geometries are especially prone to drift-induced phase errors because the four beams propagate along different paths, which compounds the effects of beam-pointing drift.

Several approaches have been developed to mitigate these phase errors. Experimentally, phase stability can be improved by enforcing common-path propagation through shared optics [17, 21–23], or it can be corrected in post-processing by monitoring phase drift through scattered light [14]. Partially collinear pump-probe geometries offer inherently improved phase stability. One benefit of this geometry is that the probe serves as the local oscillator for heterodyne detection, so there is no phase difference between the probe and local oscillator that must be corrected:

$$\phi_{\text{sig}} = \pm(\phi_1 - \phi_2) + \phi_{\text{probe}} - \phi_{\text{probe}} = \pm(\phi_1 - \phi_2) \tag{3.4}$$

where the signal phase depends only on the relative phase between the two pump pulses [8, 24]. In addition, because the two pump pulses are collinear and propagate through the same optics, phase jitter $\delta\phi_i$, affects both pump pulses equally, $\delta\phi_1 = \delta\phi_2$, and therefore cancels [25].

As described in Chapter 3.1.2, our implementation of the pump-probe geometry includes an added time-delayed local oscillator (LO). As a result, the phase correction is slightly more complex than in traditional pump-probe geometry. The time-delayed local oscillator adds a phase shift between the 3rd and 4th fields, similar to in the boxCARS geometry. However, as with the two pump pulses, the third and fourth fields are collinear and share a propagation path, so phase accumulated from path-length fluctuations cancels, $\delta\phi_3 = \delta\phi_4$.

We measure the phase difference between the pump pulses by reflecting a small component of the pump beam toward a second spectrometer. This spectrometer records the interference between pump pulses 1 and 2 throughout an experiment. In principle, this allows the pump-phase difference, $\Delta\phi_{12}$, to be corrected at every waiting time point.

For the $\Delta\phi_{34}$ phase measurement, we use the interferogram between pulses 3 and 4 recorded directly on the data camera. For polarization conditions in which pulses 3 and 4 are parallel, the sample can be removed to measure this interferogram. In practice, however, our setup often exploits orthogonality between pulses 3 and 4. Under these conditions, an analyzer aligned orthogonal to the probe pulse is installed before the detector to reject the probe background while transmitting the LO and signal. To measure the probe-LO interferogram in this configuration, the analyzer is momentarily rotated so that a small fraction of the probe reaches the detector. A small amount of neutral-density filtering is also added to prevent camera saturation.

Because the $\Delta\phi_{34}$ phase is highly stable, a single measurement at the beginning of data collection is sufficient. As evidence of this stability, we recorded thirteen probe-LO interferograms between data scans over the 51-hour period during which the data shown in Chapter 4

were collected. Taking the standard deviation of the recovered phase, we found a phase stability at 700 nm of $\lambda/120$.

In summary, although the time-delayed LO introduces an additional $\Delta\phi_{34}$ phase term, phase stability is not compromised. The procedure used to apply these phase corrections is discussed in Chapter 3.2.3.

3.1.5 Polarization Considerations for Optimal Chiral Signal Purity

Precise Polarization Alignment for Chiral Measurements

Setting polarizing optics to the precise angle required to collect chiral signal without dipolar contamination is experimentally tedious, but achievable with high-precision rotational mounts that provide sub-degree angular control. Because the dipolar signal can begin to obscure the much weaker chiral response when the polarization angles deviate by only a fraction of a degree from the ideal angle, careful polarization alignment is critical for chiral 2DES measurements [26]. Due to the required polarization precision, it is advantageous to exploit partially collinear pulse geometries to reduce experimental complexity.

The pump-probe geometry is partially collinear, meaning that the pump-pulses share the same wavevector, while the probe and local oscillator pulses share a second wavevector. Setting the polarizations of the electric fields in the pump-probe geometry is relatively straightforward because of this shared wavevector orientation. The pump pulses can be left orthogonally polarized if they are taken directly from the GEMINI-2D, or they can be made parallel by placing a polarizer downstream from the GEMINI-2D to project the pump pulse replicas onto a common polarization axis.

The same logic applies to setting the probe and local oscillator polarizations. Parallel probe and LO polarization conditions are achieved by placing a polarizer after the α-BBO crystal, thereby projecting the orthogonally polarized LO and probe onto a common polarization axis. Alternatively, the probe and local oscillator remain orthogonal when the

polarizer is placed upstream of the α-BBO crystal. In either case, setting chiral polarization conditions in the pump-probe geometry requires one arm to contain orthogonally polarized pulses and the second arm to contain parallel polarized pulses. The parallel pulse arm is finely adjusted relative to the orthogonal arm by making small micrometer adjustments to a precision rotation mount containing a high extinction ratio polarizer.

Polarization setting in the partially collinear geometry provides a significant advantage over the boxCARS geometry because fewer independent beams must be manually aligned. In the boxCARS geometry, three separate beams must be precisely aligned relative to the fourth beam, as was the case for the first published measurement of chiral 2DES polarization sequences [27]. Routine implementation of the partially collinear geometry should therefore improve the robustness of future chiral measurements by reducing experimental sources of error.

Procedurally, we use the micrometer rotation mount to finely adjust the polarization of the parallel pulses relative to the orthogonal pulses while measuring the amplitude of the transient absorption signal collected from an achiral control sample.

The polarization angle is first coarsely set by minimizing the interference between nominally orthogonal pulses, such as the pump pulse and the local oscillator for the XXXY polarization condition. For this technique, a dirty glass slide is placed at the sample position, where the pump and probe beams spatially overlap, to scatter a portion of the pump electric fields toward the data camera. The interference fringes between the pump pulses and local oscillator are maximized initially to enhance the sensitivity of our signal reduction test. The waiting time stage is set to approximately 200 fs, so that the Fourier transform of the pump-local oscillator interference fringes appears at a known temporal location. The pump polarization is first coarsely set orthogonal to the local oscillator by aligning the polarizer angle indicator orthogonal to the α-BBO crystal axes. Next, the micrometer of the same pump polarizer is rotated while pump-local oscillator Fourier transform interference

peak is minimized. The minimum amplitude of the interference peak reaches a plateau that persisted over approximately 0.5°. This precision is not sufficient for the final polarization setting, but it provides a useful starting point for the final optimization.

The final polarizer position is determined by finely incrementing the micrometer through a series of polarizer positions while collecting short time transient absorption spectra of an achiral control sample at each micrometer setting. Nominally, the achiral third-order signal is zero under ideal chiral polarization conditions. For each micrometer position, four transient absorption scans are collected with waiting time points between 200 fs and 400 fs. The signal amplitude is then compared across polarizer positions in post-processing. The summed signal amplitude exhibits quadratic dependence on polarizer angle, with the minimum corresponding to the polarization angle that produces the least achiral signal contamination. Using this technique, the signal plateau persisted over less than 0.1°, as shown in Figure 3.4. The center of the plateau was ultimately chosen as the chiral polarization angle for the data shown in Chapter 4. For chiral pump polarization conditions, the procedure requires a slight modification. Because a transient absorption measurement uses only one pump pulse, collecting TA data under orthogonal pump polarization conditions, such as XYXX or YXXX, is not possible. As an alternative, 2DES measurements can be collected at a single waiting time point for a dye sample to serve as the minimized observable. The 2DES spectra are measured over a series of probe polarization angles. The 2DES signal amplitude can then be compared across the probe polarization angles, and the signal amplitude is compared across these angles to determine the condition with minimum dipolar leak-through.

Under chiral pump polarization conditions, this procedure can be performed with or without the added time-separated local oscillator. To remove the time-separated LO, the α-BBO crystal can be removed completely from the beam path or placed upstream from the main optics controlling the probe polarization and oriented so the incident polarization is precisely aligned with the α-BBO crystal axis.

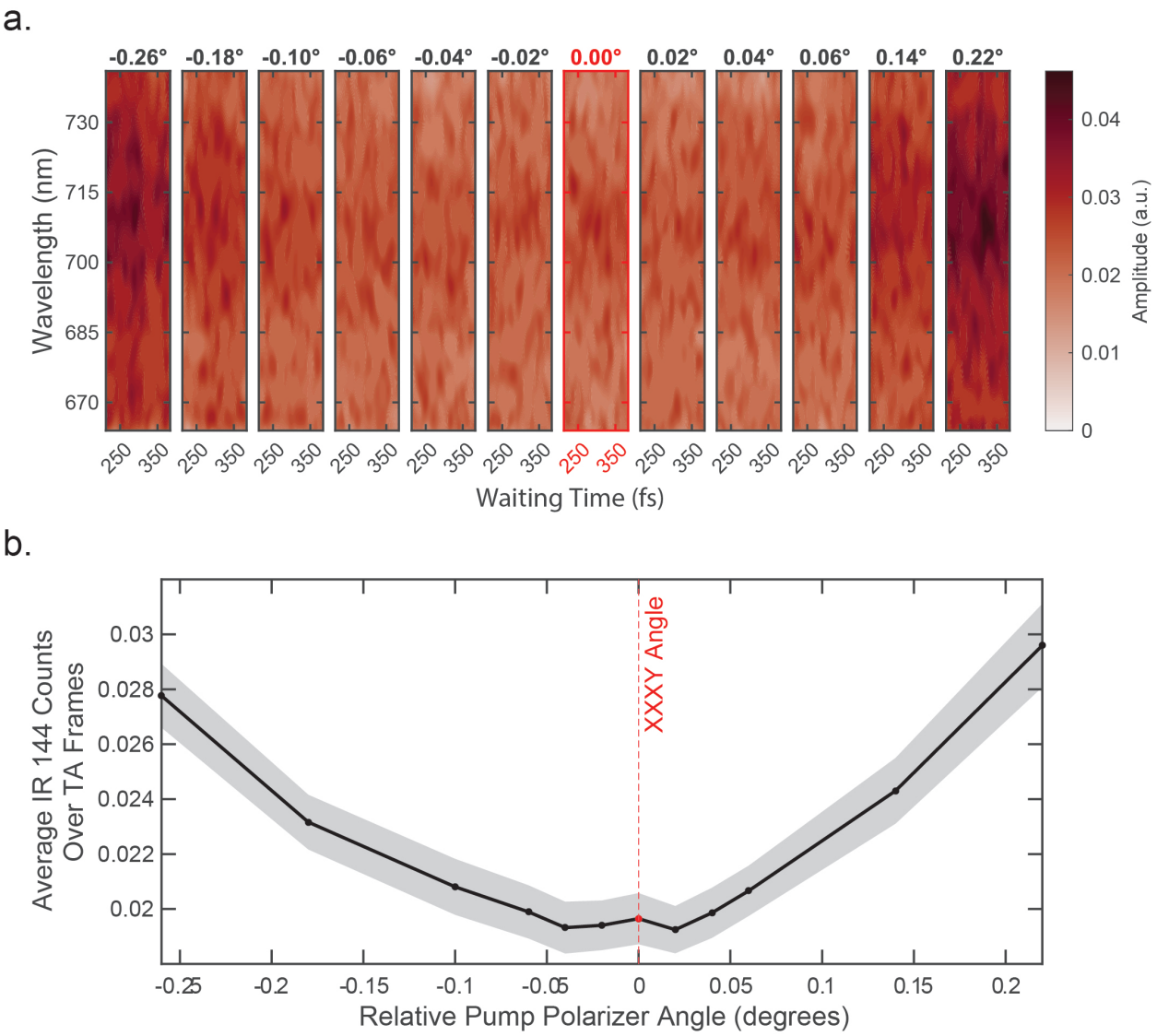

Figure 3.4: IR144 signal minimization trend used to prepare the nominal XXXY polarization condition employed in Chapter 4. (a) Transient absorption (TA) spectra acquired at a series of pump polarization angles near the nominal XXXY condition. The horizontal axis corresponds to the waiting time delay, and the vertical axis corresponds to the emission wavelength. (b) For each pump polarization angle, the signal amplitude is summed across the TA spectrum. The mean of four replicate measurements is plotted as a function of pump polarization angle, with the shaded region indicating the standard error of the mean. The angle corresponding to the minimum TA signal from the achiral sample is taken as the XXXY polarization condition for the experiment.

Engineering Optimal Polarization Purity

High-polarization purity of all four fields used in a chiral 2DES measurement is required to successfully measure the chiral response. Polarization contamination introduces dipolar signal contributions, which can quickly obscure the orders of magnitude weaker chiral signal. To maintain high polarization purity, both the choice and ordering of polarization optics are important. In particular, special care must be taken when using half-wave plates and metal mirrors.

To begin, we consider the use of half-wave plates. Half-wave plates, also known as retardation plates, introduce a 180° phase shift between the electric field components aligned with the fast and slow axes of the wave plate. For linearly polarized light incident at an angle θ relative to the fast axis, the output polarization is rotated by 2θ relative to its incident polarization [28]. This phase shift arises because wave plates are fabricated from birefringent materials, meaning that the electric field components aligned with the fast and slow axes experience different refractive indices. However, the refractive index of a material is wavelength dependent, and this wavelength dependent change in refractive index can be calculated through Sellmeier equations [29]. As a result, the phase shift imparted by the wave plate is not constant across the bandwidth of a broadband pulse. Different wavelength components therefore leave the wave plate with different retardances and, consequently, different polarizations. Because of this effect, even wave plates advertised as broadband can introduce significant polarization impurities.

Wire-grid polarizers, by contrast, generally introduce a less wavelength dependent polarization error. Their transmission depends on the orientation of the electric field polarization relative to the parallel metal wires mounted between two glass substrates. Radiation with electric field vectors oriented perpendicular to the metal wires is transmitted through the polarizer, whereas radiation with electric field vectors oriented parallel to the wires is reflected. Because this polarization selection mechanism is not based on wavelength dependent bire-

fringence, wire-grid polarizers are well suited for broadband experiments.

However, polarizers do not rotate light, which 2DES setups typically require to access a range of polarization conditions while maintaining high throughput. Therefore, when both polarization rotation and high purity are required, the wave plate should be located upstream of a high quality polarizer, which rejects unwanted polarization components and defines the final experiment polarization axis.

Another potential source of polarization impurity arises from metal mirror reflections. Silver mirrors are economical, highly reflective across the visible light spectrum, and introduce minimal dispersion, so they are commonly used in 2DES setups. However, the polarization of light can be modified upon reflection from a metal mirror because s- and p- polarized components acquire a different phase shift [30]. This phase difference can transform linearly polarized light into elliptically polarized light upon reflection, with handedness of ellipticity depending on the incident polarization angle relative to the mirror plane of incidence [31]. This effect can be eliminated when the electric field polarization is aligned as either purely s- or p- polarized relative to the mirror plane of incidence, or by using dielectric mirrors.

The reduction in polarization purity caused by metal mirror reflections is demonstrated by the purity measurements in Table 3.1. For an optical configuration in which the electric field is oriented 45° relative to the s- polarization direction, the measured extinction ration is 140:1, whereas the extinction ratio for 0° polarization is approximately 20,000:1, as shown in the last two columns of Table 3.1, respectively. Placing the polarization optics after the metal mirror reflections is one way to minimize this error. As shown in the first column, when the polarization optics are located before the metal mirrors, the extinction ratio is 97:1. In contrast, when the polarization optics are located after the metal mirrors, the extinction ratio increases to 235:1.

In the presented setup, the optical ordering was designed with the polarization impurity sources described above in mind. Ideally, all polarization optics in the pump and probe

Table 3.1: Polarization purity measurements of the collinear pump beams for different orderings of the polarization optics. A Glan-Thompson polarizer positioned immediately before a powermeter was rotated through 360° while the transmitted power was monitored to identify the analyzer angles corresponding to the minimum and maximum transmitted powers. At each of these angles, the power was averaged for 5 seconds, and the resulting values are reported in the table. The optical ordering used for each measurement is indicated by the column headers. The two polarizers in the pump beam path are denoted Pol1 and Pol2, and the wave plate is denoted WP. The angles listed for these elements indicate the approximate polarization angle of the field. The percent purity was calculated by dividing the max power by the sum of the max and min power.

	Pol1-Pol2-WP-Mirrors. 0°	Mirrors-Pol1-Pol2-WP. 90°	Mirrors-WP-Pol1-Pol2. 90°	Pol1-WP-Pol2-Mirrors. 45°	Pol1-WP-Pol2-Mirrors. 0°
Minimum Power (uW)	5.2427	2.3689	0.018736	3.4027	0.027038
Maximum Power (uW)	510.21	556.91	481.41	476.43	539.29
Extinction Ratio (max:min)	97.32:1	235.09:1	25,694:1	140.02:1	19,946:1
%Purity	98.983	99.576	99.996	99.291	99.995

paths would be located downstream of all metal mirrors, and all wave plates would be placed upstream of any final polarizers. The latter condition is much easier to accomplish than the former. Positioning all polarization optics between the final concave mirror and the sample is geometrically challenging because the pump and probe beams converge to a focal point within the sample cell after reflecting from the final concave mirror. This geometry makes it difficult to place polarization optics in the pump path without blocking the probe/LO path, or vice versa.

To help address this constraint, I changed the focusing mirror from an f=300 mm mirror to a 500 mm mirror, which reduced the convergence angle of the pump and probe beams, and provided more space for installing polarization optics before the sample. I also modified several optical mounts to reduce their footprint for the XXXY measurements presented in

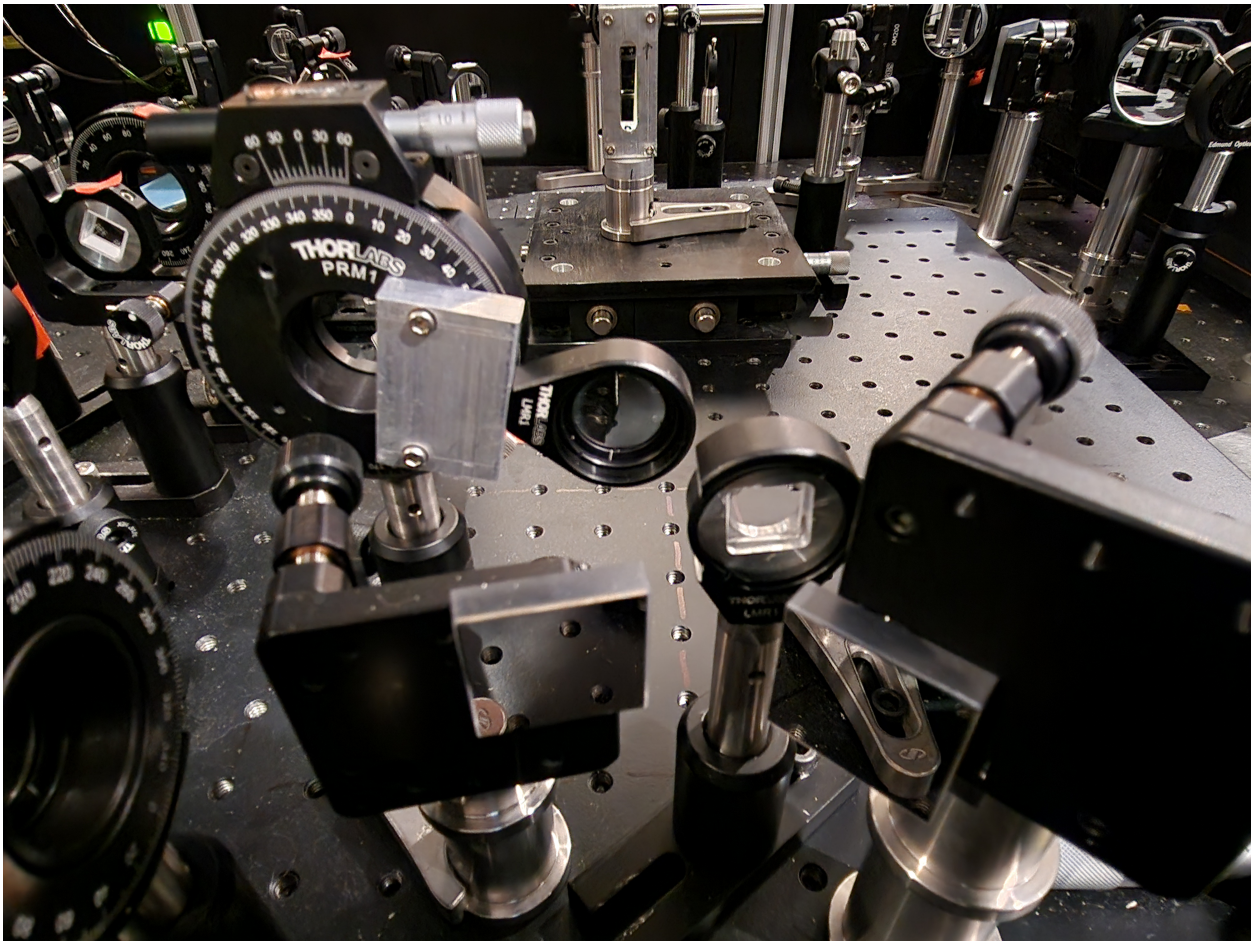

Figure 3.5: Polarization optics positioned immediately downstream all metal mirror reflections. For the $XXXY$ and $45°, 45°, 90°, 0°$ polarization conditions, the pump beam transmits through the modified precision rotation mount (left) while the probe pulse splits into the probe and temporally separated local oscillator pulse after transmitting through an α-BBO crystal (right).

Chapter 4. The native precision rotation mount, purchased from Thorlabs, is approximately 3 inches wide and holds the polarizer in the center of the mount. I machined a front plate for this precision mount that is compatible with a low profile, fixed lens mount from Thorlabs. This modified configuration allows the polarizer to be held away from the center of the bulky precision mount, so the main body of the mount can be positions farther from the pump probe beam path. Additionally, I replaced the original α-BBO crystal mount with a low-profile lens mount and cut away a portion of the mount to further minimize its footprint.

The machined mounts are shown in Figure 3.5.

Minimizing Phase-Errors from Strain-Induced Birefringence

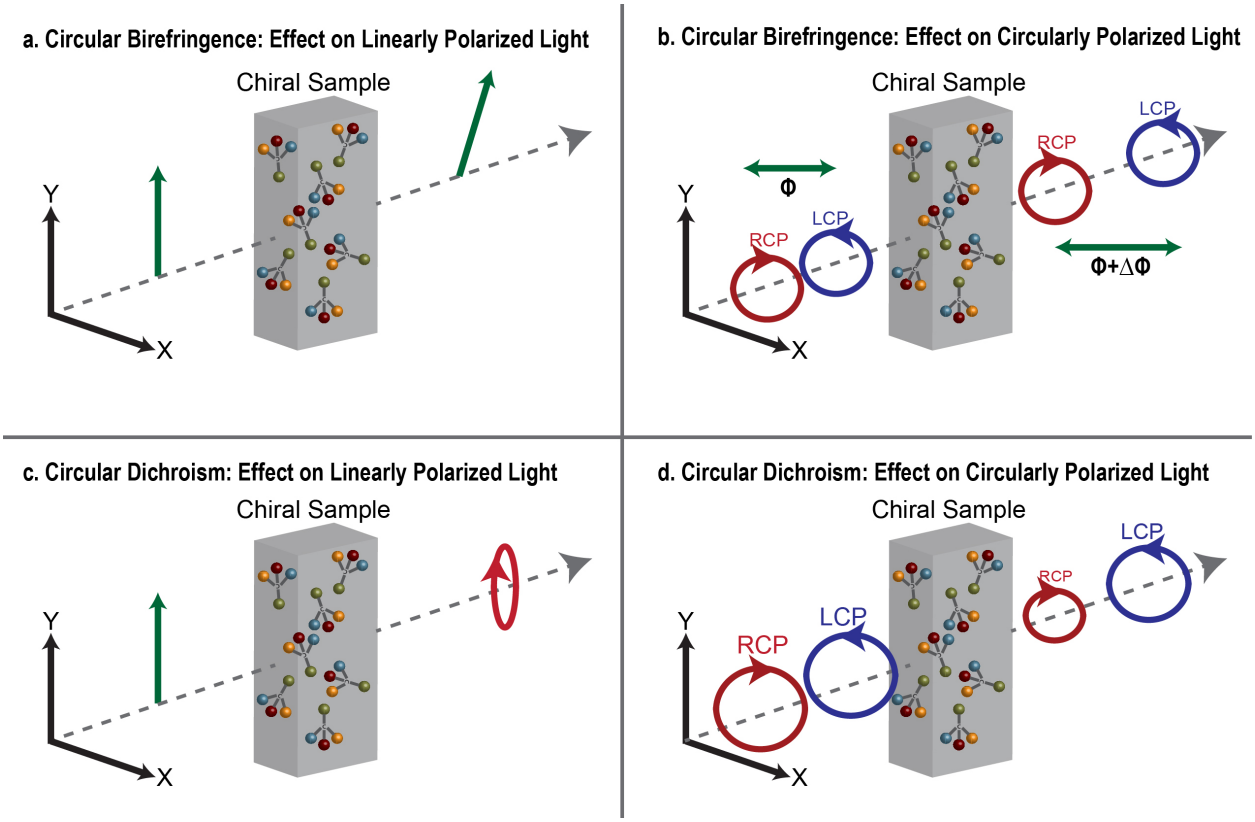

Figure 3.6: Effects of circular birefringence (CB) and circular dichroism (CD) in a chiral sample on the polarization of transmitted light. CB arises from the difference between the real refractive indices experienced by left- vs right- circularly polarized light (LCP and RCP, respectively). (a) For linearly polarized light, this differential refractive index rotates the plane of linear polarization. (b) For circularly polarized light, the polarization state remains circular, although the LCP and RCP components acquire different propagation phases. CD arises from the difference between the imaginary refractive index experienced by LCP and RCP. Consequently, CD (c) transforms linearly polarized light into elliptically polarized light and (d) produces differential absorption of LCP and RCP. These sample-induced effects can introduce polarization impurities into 2DES and TA measurements, but their magnitude can be minimized by using a sufficiently thin sample cell.

Strain induced birefringence in the sample cell can be a detrimental source of systematic error, especially in sensitive chiral measurements requiring high polarization purity and pre-

cise phase knowledge. Fused quartz is nominally isotropic; however, mechanical stress can induce birefringence. A birefringent material imparts a phase delay between electric field components aligned along its fast and slow optical axes. Consequently, pulses with nonparallel polarizations can experience different refractive indices while transmitting through a birefringent material. Under chiral polarization conditions such as XXXY, the phase differences between pulses 1 and 2 and between pulses 3 and 4 must be known accurately. For parallel polarized pulses 1 and 2, the same phase shift is imparted onto each pulse, leaving their phase difference unchanged. However, orthogonally polarized pulses 3 and 4 can experience a different index of refraction. Consequently, pulses 3 and 4 can acquire an additional phase difference after transmitting through the front plate of the sample cell. If the probe-LO phase is measured with the sample cell removed, the phase acquired through the sample cell will not contribute to the phase correction applied in post processing. This incomplete phase correction can mix the absorptive and dispersive components of the signal.

In addition to altering the 34 phase, birefringence can also compromise polarization purity which introduces achiral signal that obscures the chiral signal. Depending on the exact retardance between the crystal axes, nominally linearly polarized pulses may become elliptically polarized prior to interacting with the sample. Additionally, the pump pulses enter the front window of the sample cell at a slightly different location than the probe and LO pulses. If the strain-induced birefringence is not spatially uniform across the window, the two X-polarized pump pulses may experience a different polarization rotation compared to the X-polarized probe pulse. In that case, the intended XXXY polarization sequence is no longer pure XXXY at the sample, which can introduce achiral background into the chiral measurement.

Birefringence is also wavelength dependent, which is especially problematic for broadband experiments. Different wavelengths experience different refractive indices and therefore different retardances. This leads to wavelength dependent polarization rotation, which

introduces a variation in polarization purity across the optical spectrum.

To mitigate these sources of error, I machined a low-strain sample cell mount. The inside of the mount's bottom plate is lined with easily compressible foam, which gently holds the sample cell in place during an experiment through light compression. The bottom plate was designed with a precise inset depth to ensure that the mechanical stress applied to each sample cell is both low and consistent across samples. The inset depth corresponds to the sample cell thickness plus half of the foam height. After the sample cell is positioned within the recessed region of the bottom plate, the front plate of the mount is screwed down flush with the base plate. The sample cell mount is pictured in Figure 3.7. This design enables reproducible sample mounting while minimizing spectral artifacts that can arise from excessive sample cell strain.

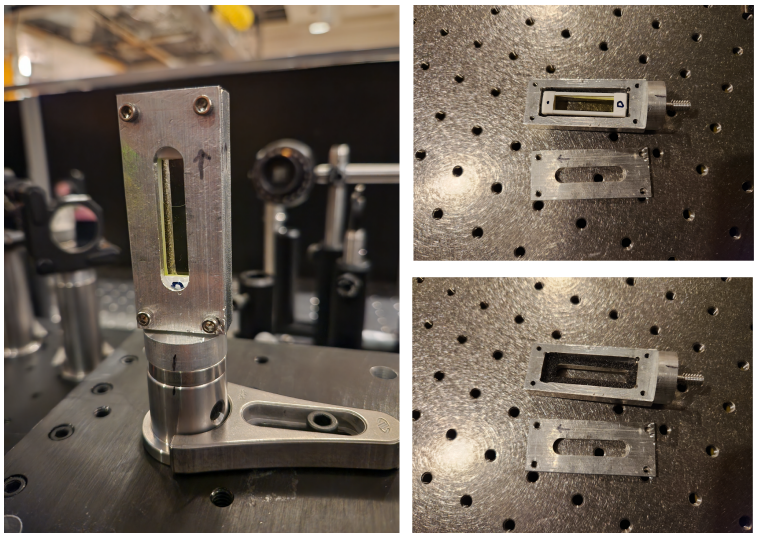

Figure 3.7: Low-strain sample cell mount machined for chiral experiments. Mount inset depth corresponds to the sample cell thickness plus 1/2 of the foam height to minimize strain applied to the sample cell from the metal plates. The gentle compression by the foam secures the sample cell in place. The top plate of the sample mount is screwed down flush with the base plate after the sample cell is placed in the divot. This design ensures consistently low strain is applied to the sample cell across measurements.

3.1.6 Pulse Characterization

We employ two forms of frequency-resolved optical gating (FROG) to characterize the temporal duration of the laser pulses. First, we perform a noncollinear cross-correlation second harmonic generation (SHG) FROG measurement between the pump and probe beams. A β-BBO crystal is placed at the pump-probe overlap position, and the generated SHG signal is detected with an Ocean Optics spectrometer in the phase-matched direction corresponding to the sum of the pump and probe wave vectors. The SHG spectrum is recorded as a function of t_2 as the pump and probe pulses are scanned through temporal overlap.

The pump pulse duration is measured independently using interferometric frequency-resolved optical gating (iFROG), in which collinear pump-pulse replicas generate an SHG interferogram as a function of their relative delay, t_1 [32, 33]. The pulse durations were retrieved using a retrieval algorithm (FROG v1.2.2, Trebino Group, Georgia Institute of Technology). The retrieved pulse durations for the pump-probe cross-FROG and iFROG were 19.1 fs and 17.1 fs respectively. The measured FROG traces are shown in Figure 3.8.

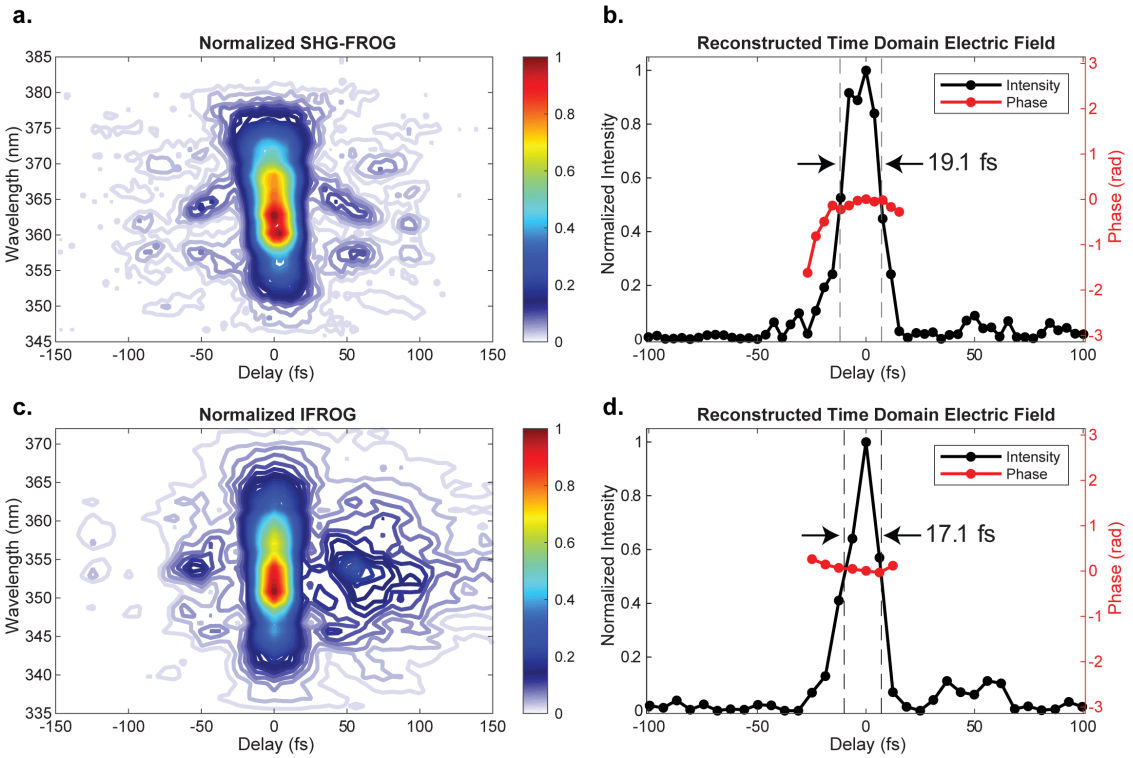

Figure 3.8: Temporal pulse width characterization. (a) Second-harmonic-generation frequency-resolved optical gating (SHG-FROG) trace used to characterize the pump and probe pulses and (b) the corresponding reconstructed time-domain intensity profile. (c) Interferometric frequency-resolved optical gating (iFROG) trace used to characterize the pump pulses and (d) the corresponding reconstructed time-domain intensity and phase. The reconstructed intensity is indicated by the black markers, and the reconstructed phase is indicated by the red markers. The retrieved FWHM from the SHG-FROG and iFROG measurements are 19.1 fs and 17.1 fs, respectively.

3.2 Data Processing

3.2.1 Third-Order Signal Isolation

The 2DES signal is detected in intensity on the camera as a function of coherence time, t_1, waiting time, t_2, and emission frequency, ω_3. In the absence of filtering, polarization-based suppression, and pump-pulse modulation, the total camera intensity can contain contributions from the emitted 2DES signal, E_{sig2D}, the pump-probe signals generated by each pump pulse, E_{sigpp1} and E_{sigpp2}, and scattered electric fields from the pump pulses, E_1 and E_2,

the probe pulse E_{pr}, and the local oscillator, E_{LO}.

$$I_{cam} = |E_1 + E_2 + E_{pr} + E_{LO} + E_{sig2D} + E_{sigpp1} + E_{sigpp2}|^2 \tag{3.5}$$

Under all-parallel polarization conditions, many cross terms can contribute to the detected intensity. Expanding Equation 3.5 gives

$$\begin{aligned} I_{cam} =& |E_1 + E_2 + E_{pr} + E_{LO} + E_{sig2D} + E_{sigpp1} + E_{sigpp2}|^2 = \\ & |E_1|^2 + |E_2|^2 + |E_{pr}|^2 + |E_{LO}|^2 + |E_{sig2D}|^2 + |E_{sigpp1}|^2 + |E_{sigpp2}|^2 \\ & + E_1E_2^* + E_1E_{pr}^* + E_1E_{LO}^* + E_1E_{sig2D}^* + E_1E_{sigpp1}^* + E_1E_{sigpp2}^* \\ & + E_2E_{pr}^* + E_2E_{LO}^* + E_2E_{sig2D}^* + E_2E_{sigpp1}^* + E_2E_{sigpp2}^* \\ & + E_{pr}E_{LO}^* + E_{pr}E_{sig2D}^* + E_{pr}E_{sigpp1}^* + E_{pr}E_{sigpp2}^* \\ & + E_{LO}E_{sig2D}^* + E_{LO}E_{sigpp1}^* + E_{LO}E_{sigpp2}^* \\ & + E_{sig2D}E_{sigpp1}^* + E_{sig2D}E_{sigpp2}^* \\ & + E_{sigpp1}E_{sigpp2}^* + \text{c.c.} \end{aligned} \tag{3.6}$$

The ultimate goal fo the scatter-removal procedure is to remove or at least minimize, all contributions other than the desired LO-heterodyne detected 2DES signal, $E_{sig}E_{LO}^*$. The appropriate strategy depends on the polarization conditions, acquisition scheme, and beam geometry. Here, I focus on the experimental and post-processing methods used to minimize scatter contributions in 2DES measurements performed under chiral pump and chiral probe polarization conditions.

The simplest case is the chiral probe sequence XXXY. In this polarization sequence, the local oscillator and detected signal are orthogonally polarized relative to the pump and probe pulses. Under XXXY polarization conditions, the Glan-Thompson polarizer placed before the detector transmits only the LO polarization and rejects X-polarized light, including contributions from E_1, E_2, and E_{pr}. The remaining fields are E_{LO}, E_{sig2D}, E_{sigpp1}, and

E_{sigpp2}. The detected intensity for this case is

$$\begin{aligned} I_{cam} = |E_{LO} + E_{sig2D} + E_{sigpp1} + E_{sigpp2}|^2 =& |E_{LO}|^2 + |E_{\mathrm{sig2D}}|^2 + |E_{sigpp1}|^2 + |E_{sigpp2}|^2 \\ &+ E_{LO}E^*_{sig2D} + E_{LO}E^*_{sigpp1} + E_{LO}E^*_{sigpp2} \\ &+ E_{sig2D}E^*_{sigpp1} + E_{sig2D}E^*_{sigpp2} \\ &+ E_{sigpp1}E^*_{sigpp2} + \mathrm{c.c.} \end{aligned} \tag{3.7}$$

Additionally, the pump pulses are modulated with a chopper, producing alternating pump-on and pump-off camera frames. The pump-off frame contains the LO-only intensity, $|E_{LO}|^2$, which is subtracted from the pump-on frame in post-processing. The desired heterodyne-detected signal is then further isolated using Fourier domain filters. These filter exploit the different behavior of the desired signal and residual scatter or pump-probe contamination along the waiting-frequency, coherence frequency, and detection-time axes.

First, consider the detection time domain, t_3. The desired signal is heterodyne detected with a local oscillator that precedes the emitted signal by 1.1 ps. As a result, the desired $E_{sig}E_{LO}$ signal appears at the LO signal delay in detection time. Therefore, any signal contributions arising from pairs of fields that are not separated by 1.1 ps can be suppressed by applying a window centered on the 1.1 ps peak. This procedure removes all homodyne detected terms and non LO cross terms. After windowing in detection time, we are left with the desired signal, $E_{sig}E_{LO}$, and the LO heterodyne detected pump-probe signals $E_{LO}E^*_{sigpp1}$ and $E_{LO}E^*_{sigpp2}$.

$$I_{cam} = + E^*_{LO}E_{sig2D} + E^*_{LO}E_{sigpp1} + E^*_{LO}E_{sigpp2} + \mathrm{c.c.} \tag{3.8}$$

The remaining pump-probe signals do not oscillate at the optical frequency as a function of coherence time. Therefore, after Fourier transformation over t_1 to ω_1, these signals appear near zero coherence frequency. In contrast, the 2DES signal appears at the optical frequency,

and can be isolated by applying a coherence frequency window.

For the other chiral probe sequence, XXYX, the probe is orthogonally polarized relative to the analyzer and is therefore rejected prior to the detector. However, because the pump pulses are parallel to the analyzer polarization, pump pulse scatter can contribute to the measured signal. In this case, the detected signal is

$$\begin{aligned} I_{cam} =& |E_1 + E_2 + E_{LO} + E_{sig2D} + E_{sigpp1} + E_{sigpp2}|^2 = \\ & |E_1|^2 + |E_2|^2 + |E_{LO}|^2 + |E_{sig2D}|^2 + |E_{sigpp1}|^2 + |E_{sigpp2}|^2 \\ & E_1E_2^* + E_1E_{LO}^* + E_1E_{sig2D}^* + E_1E_{sigpp1}^* + E_1E_{sigpp2}^* \\ & + E_2E_{LO}^* + E_2E_{sig2D}^* + E_2E_{sigpp1}^* + E_2E_{sigpp2}^* \\ & + E_{LO}E_{sig2D}^* + E_{LO}E_{sigpp1}^* + E_{LO}E_{sigpp2}^* \\ & + E_{sig2D}E_{sigpp1}^* + E_{sig2D}E_{sigpp2}^* \\ & + E_{sigpp1}E_{sigpp2}^* + \text{c.c.} \end{aligned} \tag{3.9}$$

As with the XXXY sequence, homodyne-detected terms and non LO cross terms are removed under XXYX polarization conditions by applying a detection time window centered at 1.1 ps. The terms that remain are

$$\begin{aligned} I_{cam} =& |E_1 + E_2 + E_{LO} + E_{sig2D} + E_{sigpp1} + E_{sigpp2}|^2 = \\ & + E_1E_{LO}^* + E_2E_{LO}^* + E_1E_{sig2D}^* + E_2E_{sig2D}^* \\ & + E_{LO}E_{sig2D}^* + E_{LO}E_{sigpp1}^* + E_{LO}E_{sigpp2}^* \\ & + \text{c.c.} \end{aligned} \tag{3.10}$$

the $E_1E_{LO}^*$, $E_2E_{LO}^*$, $E_1E_{sig2D}^*$, and $E_2E_{sig2D}^*$ terms are also suppressed by the detection time window, except when the separation between fields falls within the 1.1 ps window. For $E_1E_{LO}^*$ and $E_2E_{LO}^*$, this condition is met when scattered pump light is separated from the LO by approximately 1.1 ps, which occurs at waiting times near 0 fs. For $E_1E_{sig2D}^*$, and

$E_2 E^*_{sig2D}$, this condition is met around a waiting time of 1.1 ps. We can then remove the remaining LO heterodyne detected pump probe signals by applying a coherence frequency window. As described above, during coherence frequency, the desired signal oscillates at the at the optical frequency while the pump-probe signals appear near zero coherence frequency because they are not dependent on t_1.

Under chiral pump polarization conditions, XYXX and YXXX, the windowing procedure follows the same general logic used for the XXYX polarization conditions. However, because one of the pump pulses is orthogonally polarized relative to the transmitted detection polarization, scattered light from the orthogonal pump field is rejected by the analyzer.

3.2.2 Isolating Rephasing and Non Rephasing Signal Contributions

Rephasing and non-rephasing signal components of the measured 2DES signal are separated using a processing-level technique developed by Timmer et al. [34]. For 2DES data collected in the pump-probe geometry, the pump pulses are collinear, so the rephasing and non-rephasing signal components are emitted at the same time and in the same direction, as described in Chapter 3.1.2. The two components can nonetheless be disentangled by enforcing causality in the emission-time Fourier domain. I adopt a similar framework, with modifications to account for the LO-heterodyne signal detection employed in this setup, since Timmer et al. [34] use a conventional pump-probe geometry in which the probe serves as both the third interaction field and the LO. The full theoretical treatment is described in the original work.

In the presented setup, the 2DES signal is detected in intensity by a 2048-pixel CCD camera as a function of coherence time, waiting time, and detection wavelength. The non-rephasing and rephasing signal components can be tracked through the processing steps by their spectral quadrants shown in Figure 3.9, similar to the treatment by Timmer et al. [34].

To begin, the raw signal is a real-valued interferogram measured over positive emis-

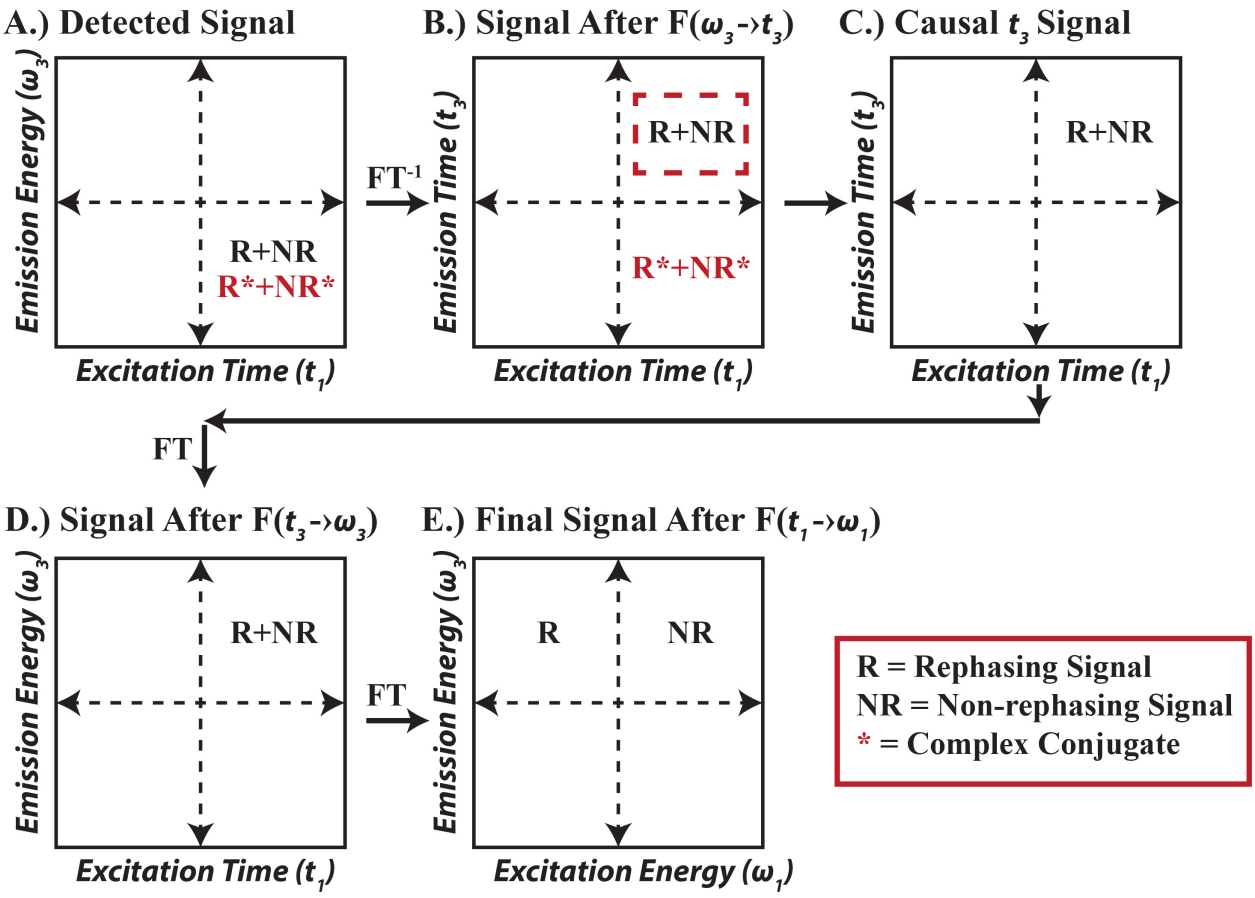

Figure 3.9: Schematic illustrating the separation of the rephasing and non-rephasing signal components. Figure was adapted from [34], licensed under CC BY 4.0.

sion frequencies, as shown in Figure 3.9A. The signal is Fourier transformed from emission frequency to the emission-time domain, t_3, where the rephasing and non-rephasing contributions, R and NR, separate from their complex conjugates, R* and NR*, into different t_3 quadrants. This separation arises from their opposing phase evolution during t_3 [35]. This quadrant separation is shown in Figure 3.9B.

Timmer et al. then enforce causality by applying a Heaviside step function in t_3 [34]. Functionally, points in $t_3<0$ are set to zero, which removes NR* and R*. The data point at time zero is also multiplied by 0.5 to avoid background artifacts. This procedure leaves the rephasing and non-rephasing components in a single causal quadrant, as shown in Fig-

ure 3.9C.

At this point, our implementation differs slightly. In our setup, the 2DES signal is heterodyne detected by a local oscillator that precedes the probe pulse by 1.1 ps. Consequently, the LO heterodyne detected signal appears at positive 1.1 ps in the t_3 domain. We isolate the signal peak by applying a Tukey window centered at 1.1 ps. All signal and scatter outside this window, including non-causal signal at negative t_3, are set to zero.

The causal signal is then Fourier transformed back to emission frequency, which does not produce any further quadrant separation of the rephasing and non-rephasing components, as shown in Figure 3.9D. Lastly, the signal is Fourier transformed over coherence time to coherence frequency. This step further separates the rephasing and non-rephasing contributions into distinct ω_1 quadrants because of their opposite phase evolution during coherence time, as shown in Figure 3.9E. The rephasing and non-rephasing signal components are then fully isolated and can be individually analyzed or combined to yield the absorptive signal.

3.2.3 Phase Corrections

Phasing 2DES Data

Accurate isolation of the real and imaginary components of the 2DES signal requires precise phase correction protocols that account for phase accumulated by each interacting electric field. The phase stability and formal definitions are introduced in Chapter 3.1.4. For the 2DES setup described in this thesis, the phase differences between pulses 1 and 2, $\Delta\phi_{12}$, and between pulses 3 and 4, $\Delta\phi_{34}$, must be measured and set to zero to isolate the absorptive signal.

As mention in Chapter 3.1.4, an ND filter in the pump path directs a small component of the beam towards a second spectrometer. This spectrometer records the interferogram between pump pulses 1 and 2 as the coherence time delay is scanned during an experiment. Prior to phasing, the coherence frequency domain is first calibrated using previously

described methods [3, 36]. The interferograms are plotted as a two-dimensional map as a function of the GEMINI-2D motor position and camera frequency. Fourier transforming over the motor position axis yields a series of frequency domain peaks whose locations depend on wavelength. The peak positions in the motor frequency domain are then correlated with the calibrated spectrometer frequency domain, and a frequency calibration factor is determined from a linear fit.

The same set of interferograms is used to phase the coherence frequency domain. Determining the phase requires precise knowledge of the coherence time zero and the absolute phase difference between the two pump pulses. This procedure is described by Helbing and Hamm [37]. Briefly, each coherence time point corresponds to a discrete time step, or bin, κ. Around time zero, the interferogram is cut at a selected bin, denoted κ_0, and the first $\kappa_0 - 1$ points are shifted to the end of the array prior to Fourier transforming from the time domain to the frequency domain. The amplitude and phase are then extracted for all optical frequencies, and a phase vs. frequency plot is generated. The phase across the optical spectrum is fit with a linear function. This procedure is repeated for the time bins near the approximate time zero.

The approximate time zero is expected to occur near the maximum intensity of the interferogram. However, because a phase offset can exist at time zero, the interferogram intensity alone cannot be used to identify the exact time zero bin. Instead, the time bin with the smallest slope is assigned as the bin closest to time zero. If the selected bin is negative relative to the true time zero bin, the slope of the phase with respect to frequency is negative. Conversely, if the selected bin is positive relative to time zero, the slope is positive. During data processing, data points preceding the time zero bin are discarded prior to Fourier Transformation. The total phase correction consists of the first-order frequency dependent slope and the zeroth-order absolute phase determined from the linear fit. For the 2DES data, conjugate phase corrections are applied independently to the rephasing and non-rephasing

signal components before they are combined to recover the complete absorptive signal [34].

Before beginning a series of 2DES measurements, we typically collect approximately three finely spaced interferograms. We then use the calculated time zero to calibrate the time zero stage position in the acquisition software. This procedure minimizes first-order phase correction required during post-processing. Despite these preemptive steps, a residual phase slope is typically measured, corresponding to a slight temporal offset in the assigned coherence time zero.

An additional phase correction is applied over the emission frequency domain. Introducing a time domain local oscillator with a temporal separation from the probe of approximately Δt_{LO} adds an emission frequency phase factor, $\omega_3 \Delta t_{LO}$, which produces interference fringes in the frequency domain [25]. As discussed in Chapter 3.1.4, the interferogram between collinear probe and local oscillator pulses is measured directly on the detection camera. Fourier transform spectral interferometry (FTSI) is then used to measure the phase difference between the probe and local oscillator. In post-processing, the interferogram is Fourier transformed from the frequency to the time domain. The positive time component is isolated by applying a spectral filter, while the DC and negative time components are removed. After Fourier transforming back to the frequency domain, the phase is extracted. Phase corrections up to second order are then applied to the detection frequency domain of the 2DES data.

Phasing TA Data

Traditionally, transient absorption (TA) data do not require phasing to accurately recover the signal phase. This is the primary reason TA spectra are commonly used as a point of comparison for phasing strategies based on projection-slice theorem [17]. In the experimental setup described in this thesis, chiral probe TA polarization conditions are measured by heterodyne detecting the TA signal with a time separated local oscillator, enabling mea-

surements in which the third and fourth fields are orthogonally polarized, as described in Chapter 3.1.3. As in the 2DES measurement, this heterodyne-detection scheme introduces an additional phase contribution from the relative phase accumulated between the probe and LO. Therefore, a phase correction must be applied to the TA data to isolate the phase of the emitted signal. Conveniently, the phase extraction and correction procedure is identical to the probe-LO phase correction procedure described in the previous section. An example TA spectrum before and after applying the probe-LO phase correction is demonstrated in Figure 3.10.

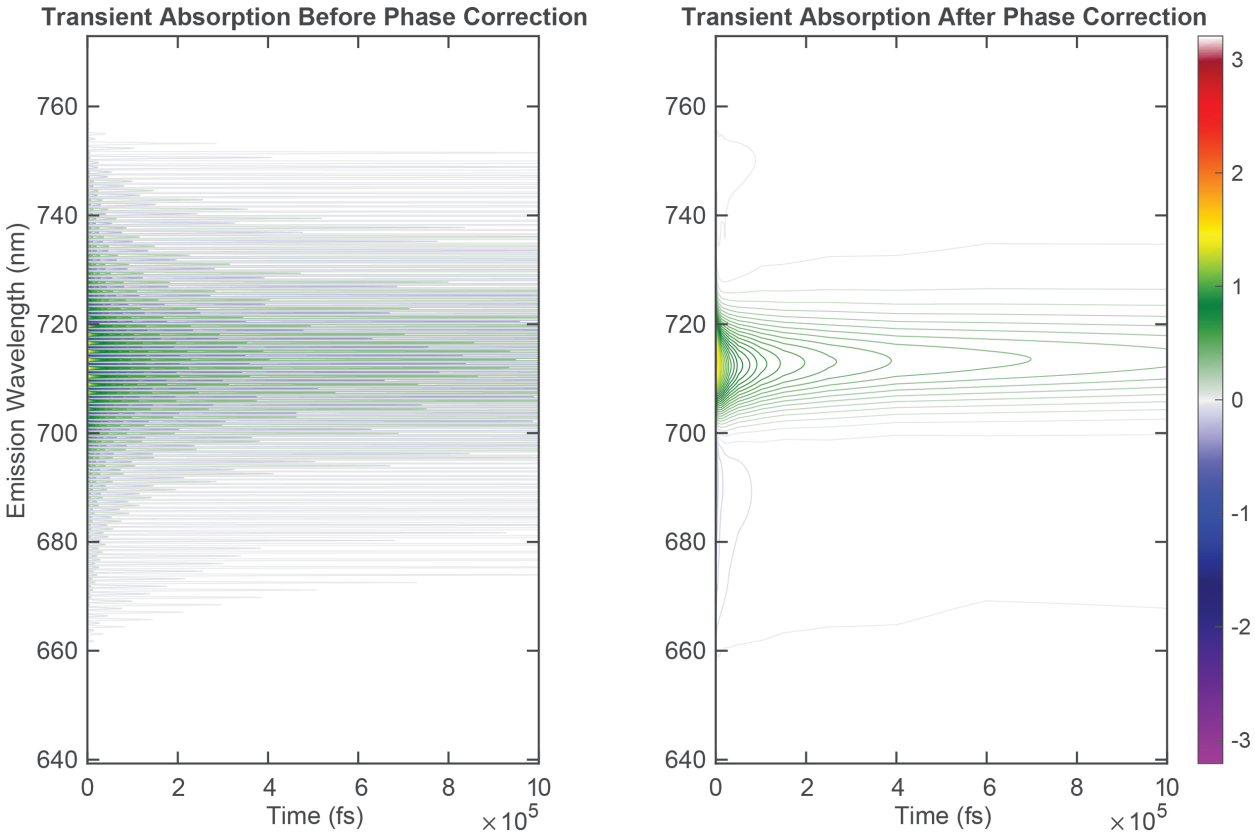

Figure 3.10: Local oscillator (LO) heterodyne detected transient absorption spectra before (left) and after (right) applying a phase correction that compensates for the relative phase accumulated between the emitted signal and LO.

3.3 Generality of Chiral Data and Amenability to Traditional 2DES Analysis

3.3.1 Effect of Chirality on Excited-State Evolution

As discussed theoretically in Chapter 2, spectroscopic experiments measure the signal field emitted by the induced macroscopic polarization generated through light-matter interactions. In third-order nonlinear 2DES experiments, this emitted signal field depends on interactions with three radiation fields at distinct time points. Each interaction probes a transition dipole moment connecting two molecular states, such that the detected third-order signal is proportional to the product of four transition dipole moments. This transition-dipole dependence allows 2DES measurements to characterize excited state phenomena such as energy transfer and vibronic coherences.

The same excited-state processes that govern the dynamics observed in achiral 2DES also contribute to the dynamics observed in chiral 2DES spectra. Experimentally, we can selectively measure the chiral contributions to the response function by employing odd polarization conditions. In a chiral 2DES experiment, the orthogonal field polarization can be placed in any one of the four field positions. These odd-polarization sequences are analogous to the difference between two measurements, in which three fields are linearly polarized along the same axis, while the remaining field is left circularly polarized for one measurement and right circularly polarized for the second measurement. For example, $(X,X,X,Y) \propto (X,X,X,R) - (X,X,X,L)$ [38]. The circular polarization difference can be applied to any of the four field positions, giving four chiral linear polarization conditions: XXXY, XXYX, XYXX, and YXXX. The chiral polarization conditions are further categorized by the location of the orthogonal field, with XYXX and YXXX being chiral "pump" polarization conditions, and XXXY and XXYX being chiral "probe" polarization conditions [27].

Early theoretical descriptions of chiral 2DES simulated chiral pump measurements by taking the difference between experiments performed with left and right circularly polarized pump excitations [39, 40]. Chiral pump polarization conditions are most closely related to the transitions from the ground state to one-exciton manifold probed in steady-state circular dichroism measurements, while adding the temporal resolution needed to monitor nonequilibrium excited state dynamics [40]. In contrast, chiral probe polarization conditions provide sensitivity to chiral contributions associated with later interactions. Differences between the dynamics observed under chiral pump and probe polarization conditions can therefore be rationalized by considering where the chiral-sensitive interaction occurs relative to the excited state evolution.

The observed density matrix evolution depends on the field interaction that imparts chiral selectivity into the nonlinear response. For the chiral pump polarization conditions YXXX and XYXX, one of the two pump pulses is orthogonal relative to the other three field polarizations. In both cases, amplitude transfer occurs between states selected by orthogonal Y and X polarized interactions during coherence time [41]. As a result, the signal evolution during t_1 is similar for the two chiral pump polarization conditions. However, under XYXX polarization conditions, there is an additional redistribution of exciton amplitude from states selected by the Y polarized interaction to those selected by the X polarized interactions during the waiting time, t_2. Similarly, the chiral probe polarization condition, XXYX, exhibits amplitude transfer between the states with X and Y polarized properties during t_2, but does not involve the same amplitude transfer during coherence time. For the remaining chiral probe polarization condition, XXXY, the amplitude transfer occurs during the final emission time, t_3.

Using these relationships, the chiral polarization conditions can be used to infer how the timing of amplitude transfer processes affects the observed density matrix evolution. When the orthogonal field interaction prepares a chiral-sensitive coherence that evolves during t_1

or t_3, we know the observed response is directly linked to the coherence evolution during the initial excitation or final emission time periods. In contrast, when the amplitude transfer occurs during t_2, the density matrix evolves as either a population, or vibronic or vibrational coherence. Therefore, as an example, if the goal is to isolate how an initially prepared chiral coherence in t_1 influences subsequent t_2 dynamics, the YXXX polarization condition is most informative. In contrast, if the desire is to prepare an achiral population, then monitor how chiral sensitivity emerges over waiting time, the XXYX polarization condition is ideal.

3.3.2 Chiral 2DES Liouville Pathway Dependence

In addition to its temporal evolution, the measured signal is shaped by the orientational factors that weight the contributing Feynman pathways. The following discussion builds on the theoretical formalism detailed in Chapter 2.4, with the shared assumption that the beam propagation is collinear with a propagation direction along the Z-axis in the laboratory fixed frame.

For an isotropic ensemble, each contributing Feynman pathway is weighted by an orientational factor determined by the tensor products of the laboratory frame field polarizations and the molecular transition moments associated with each field-matter interaction. Under the dipole approximation, the third-order signal arises from four electric dipole interactions, one for each field interaction and heterodyne detection. Beyond the dipole approximation, the signal contains additional tensor elements resulting from the magnetic field interactions with the magnetic dipoles, and the electric field interactions with the electric quadrupoles. These higher order contributions are sensitive to chirality, and therefore produce signals that are equal amplitude and opposite signs for opposite enantiomers. However, because the sign of the 2DES signal is dependent on the molecular geometry, and the Feynman pathway, there is additional sign ambiguity that must be considered when assigning features to specific Feynman pathways.

Conventional dipolar 2DES spectra contain positive ground state bleach (GSB) and stimulated emission (SE) contributions and negative excited-state absorption (ESA) contributions. In chiral 2DES spectra, however, the sign of features also depends on the signs and relative magnitudes of the magnetic dipole and electric quadrupole contributions, as well as on the specific chiral polarization conditions and their associated orientational factors. For the magnetic dipole interactions, the sign reflects the GSB/SE or ESA identity, the polarization conditions, and the sign of the relevant rotational strengths [38]. Consequently, two SE features that were both positive in a dipolar spectrum may have opposite signs in a chiral 2DES spectrum if their chiral orientational weighting factors are opposite in sign. Feature sign alone therefore cannot be used to distinguish ESA from GSB and SE pathways in chiral 2DES spectra. Instead, the sign ambiguity can be navigated through modeling and comparisons with spectra acquired under dipolar polarization conditions.

Changing the polarization conditions between chiral and dipolar measurements does not alter the underlying molecular transition frequencies. However, the different orientational factors between the two polarization conditions can enhance, suppress, or invert the signs of specific pathways [42]. Dipolar measurements can therefore aid the assignment of features although spectral congestion and differing orientational weights may prevent absolute certainty.

The geometry-dependent signs of chiral features provide several unique advantages. In congested spectra, features with opposite-signed chiral weights can become more readily distinguishable than features that overlap with the same sign under dipolar polarization conditions [43]. Additionally, the sign variation can be used to directly track the handed arrangement of transition dipole moments, information invisible under dipolar measurements. For example, consider two off diagonal ground state bleach features excited at the same excitation energy, but emitted at different emission energies. If the features are opposite in sign, this would indicate the chiral weights are also opposite in sign. For pathways domi-

nated by the magnetic dipole contribution, the opposite signed features would correspond to opposite signed net rotational strengths weighting the two features. These sign patterns provide insight into the local transition dipole environments, the handed arrangement of coupled transition dipoles, and the subsequent influence of this chiral organization on the observed excited-state dynamics.

References

(1) Novanta Photonics DCM Dispersion Compensating Mirror Pairs for Femtosecond Pulse Compression, FindLight Photonics Marketplace, `https://www.findlight.net/lasers/ultrafast-lasers/accessories/dispersion-compensating-mirrors-femtosecond-pulse-compression`, Accessed: 2026-04-27, 2025.

(2) Brida, D.; Manzoni, C.; Cerullo, G. Phase-locked pulses for two-dimensional spectroscopy by a birefringent delay line. *Opt. Lett.* **2012**, *37*, 3027–3029.

(3) Réhault, J.; Maiuri, M.; Manzoni, C.; Brida, D.; Helbing, J.; Cerullo, G. 2D IR spectroscopy with phase-locked pulse pairs from a birefringent delay line. *Opt. Express* **2014**, *22*, 9063–9072.

(4) Perri, A. Visible and near-infrared Fourier transform spectroscopy with a common-path interferometer. *Journal of Physics B: Atomic, Molecular and Optical Physics* **2021**, *54*, 113001.

(5) Gallagher Faeder, S. M.; Jonas, D. M. Two-Dimensional Electronic Correlation and Relaxation Spectra: Theory and Model Calculations. *The Journal of Physical Chemistry A* **1999**, *103*, 10489–10505.

(6) Shim, S.-H.; Strasfeld, D. B.; Ling, Y. L.; Zanni, M. T. Automated 2D IR spectroscopy using a mid-IR pulse shaper and application of this technology to the human islet amyloid polypeptide. *Proceedings of the National Academy of Sciences* **2007**, *104*, 14197–14202.

(7) DeFlores, L. P.; Nicodemus, R. A.; Tokmakoff, A. Two-dimensional Fourier transform spectroscopy in the pump-probe geometry. *Opt. Lett.* **2007**, *32*, 2966–2968.

(8) Hamm, P.; Zanni, M. *Concepts and Methods of 2D Infrared Spectroscopy*; Cambridge University Press: 2011.

(9) Khalil, M.; Demirdöven, N.; Tokmakoff, A. Obtaining Absorptive Line Shapes in Two-Dimensional Infrared Vibrational Correlation Spectra. *Phys. Rev. Lett.* **2003**, *90*, 047401.

(10) Myers, J. A.; Lewis, K. L. M.; Tekavec, P. F.; Ogilvie, J. P. Two-color two-dimensional Fourier transform electronic spectroscopy with a pulse-shaper. *Opt. Express* **2008**, *16*, 17420–17428.

(11) Andrews, D. L.; Thirunamachandran, T. On three-dimensional rotational averages. *The Journal of Chemical Physics* **1977**, *67*, 5026–5033.

(12) Cowan, M.; Ogilvie, J.; Miller, R. Two-dimensional spectroscopy using diffractive optics based phased-locked photon echoes. *Chemical Physics Letters* **2004**, *386*, 184–189.

(13) Albrecht, A. W.; Hybl, J. D.; Gallagher Faeder, S. M.; Jonas, D. M. Experimental distinction between phase shifts and time delays: Implications for femtosecond spectroscopy and coherent control of chemical reactions. *The Journal of Chemical Physics* **1999**, *111*, 10934–10956.

(14) Lloyd, L. T.; Wood, R. E.; Allodi, M. A.; Sohoni, S.; Higgins, J. S.; Otto, J. P.; Engel, G. S. Leveraging scatter in two-dimensional spectroscopy: passive phase drift correction enables a global phasing protocol. *Opt. Express* **2020**, *28*, 32869–32881.

(15) Fuller, F. D.; Ogilvie, J. P. Experimental Implementations of Two-Dimensional Fourier Transform Electronic Spectroscopy. *Annual Review of Physical Chemistry* **2015**, *66*, 667–690.

(16) Hybl, J. D.; Albrecht, A. W.; Gallagher Faeder, S. M.; Jonas, D. M. Two-dimensional electronic spectroscopy. *Chemical Physics Letters* **1998**, *297*, 307–313.

(17) Brixner, T.; Mančal, T.; Stiopkin, I. V.; Fleming, G. R. Phase-stabilized two-dimensional electronic spectroscopy. *The Journal of Chemical Physics* **2004**, *121*, 4221–4236.

(18) Fresch, E.; Camargo, F. V. A.; Shen, Q.; Bellora, C. C.; Pullerits, T.; Engel, G. S.; Cerullo, G.; Collini, E. Two-dimensional electronic spectroscopy. *Nature Reviews Methods Primers* **2023**, *3*, 84.

(19) Hybl, J. D.; Albrecht Ferro, A.; Jonas, D. M. Two-dimensional Fourier transform electronic spectroscopy. *The Journal of Chemical Physics* **2001**, *115*, 6606–6622.

(20) Jonas, D. M. Two-Dimensional Femtosecond Spectroscopy. *Annual Review of Physical Chemistry* **2003**, *54*, 425–463.

(21) Selig, U.; Langhojer, F.; Dimler, F.; Löhrig, T.; Schwarz, C.; Gieseking, B.; Brixner, T. Inherently phase-stable coherent two-dimensional spectroscopy using only conventional optics. *Opt. Lett.* **2008**, *33*, 2851–2853.

(22) Spencer, A. P.; Chen, L. X. Rapid acquisition of broadband two-dimensional electronic spectra by continuous scanning with conventional delay lines. *Opt. Lett.* **2020**, *45*, 2942–2945.

(23) Gellen, T. A.; Bizimana, L. A.; Carbery, W. P.; Breen, I.; Turner, D. B. Ultrabroadband two-quantum two-dimensional electronic spectroscopy. *The Journal of Chemical Physics* **2016**, *145*, 064201.

(24) Shim, S.-H.; Zanni, M. T. How to turn your pump–probe instrument into a multidimensional spectrometer: 2D IR and Vis spectroscopiesvia pulse shaping. *Phys. Chem. Chem. Phys.* **2009**, *11*, 748–761.

(25) Schlau-Cohen, G. S.; Ishizaki, A.; Fleming, G. R. Two-dimensional electronic spectroscopy and photosynthesis: Fundamentals and applications to photosynthetic light-harvesting. *Chemical Physics* **2011**, *386*, 1–22.

(26) Holdaway, D. I. H.; Collini, E.; Olaya-Castro, A. Isolating the chiral contribution in optical two-dimensional chiral spectroscopy using linearly polarized light. *Opt. Express* **2017**, *25*, 6383–6401.

(27) Fidler, A. F.; Singh, V. P.; Long, P. D.; Dahlberg, P. D.; Engel, G. S. Dynamic localization of electronic excitation in photosynthetic complexes revealed with chiral two-dimensional spectroscopy. *Nature communications* **2014**, *5*, 3286.

(28) Hecht, E. *Optics*; Pearson: 2012.

(29) Paschotta, R. Sellmeier Formula RP Photonics AG, `https://www.rp-photonics.com/sellmeier_formula.html` (accessed 04/23/2026).

(30) Lichten, W. Precise wavelength measurements and optical phase shifts. I. General theory. *J. Opt. Soc. Am. A* **1985**, *2*, 1869–1876.

(31) Swindell, W. Handedness of Polarization after Metallic Reflection of Linearly Polarized Light. *Journal of the Optical Society of America* **1971**, *61*, 212–215.

(32) Stibenz, G.; Steinmeyer, G. Interferometric frequency-resolved optical gating. *Opt. Express* **2005**, *13*, 2617–2626.

(33) Timmer, D.; Lünemann, D. C.; Gittinger, M.; Sio, A. D.; Manzoni, C.; Cerullo, G.; Lienau, C. Phase-cycling and double-quantum two-dimensional electronic spectroscopy using a common-path birefringent interferometer. *Optica* **2024**, *11*, 1646–1653.

(34) Timmer, D.; Lünemann, D. C.; De Sio, A.; Cerullo, G.; Lienau, C. Disentangling signal contributions in two-dimensional electronic spectroscopy in the pump–probe geometry. *The Journal of Chemical Physics* **2025**, *162*, 124202.

(35) Zhang, Z.; Wells, K. L.; Hyland, E. W. J.; Tan, H.-S. Phase-cycling schemes for pump–probe beam geometry two-dimensional electronic spectroscopy. *Chemical Physics Letters* **2012**, *550*, 156–161.

(36) Réhault, J.; Maiuri, M.; Oriana, A.; Cerullo, G. Two-dimensional electronic spectroscopy with birefringent wedges. *Review of Scientific Instruments* **2014**, *85*, 123107.

(37) Helbing, J.; Hamm, P. Compact implementation of Fourier transform two-dimensional IR spectroscopy without phase ambiguity. *J. Opt. Soc. Am. B* **2011**, *28*, 171–178.

(38) Choi, J.-H.; Cho, M. Quadrupole contribution to the third-order optical activity spectroscopy. *The Journal of Chemical Physics* **2007**, *127*, 024507.

(39) Cho, M. Two-dimensional circularly polarized pump–probe spectroscopy. *The Journal of Chemical Physics* **2003**, *119*, 7003–7016.

(40) Choi, J.-H.; Cho, M. Nonlinear optical activity measurement spectroscopy of coupled multi-chromophore systems. *Chemical Physics* **2007**, *341*, Ultrafast Dynamics of Molecules in the Condensed Phase: Photon Echoes and Coupled Excitations, 57–70.

(41) Abramavicius, D.; Mukamel, S. Time-domain chirally-sensitive three-pulse coherent probes of vibrational excitons in proteins. *Chemical Physics* **2005**, *318*, Molecular Nanoscience, 50–70.

(42) Abramavicius, D.; Mukamel, S. Coherent third-order spectroscopic probes of molecular chirality. *The Journal of Chemical Physics* **2005**, *122*, 134305.

(43) Voronine, D. V.; Abramavicius, D.; Mukamel, S. Chirality-Based Signatures of Local Protein Environments in Two-Dimensional Optical Spectroscopy of Two Species Photosynthetic Complexes of Green Sulfur Bacteria: Simulation Study. *Biophysical Journal* **2008**, *95*, 4896–4907.

CHAPTER 4

CHIRAL EXCITONIC DYNAMICS IN PORPHYRIN AGGREGATES

4.1 Abstract

An example application of the instrument approach discussed in Chapter 3 will be detailed within this chapter, which describes the results of a current manuscript in preparation. Parts of this chapter were co-written by the corresponding first authors, Elizabeth Bain, Olivia Wedig, and myself.

Chirality is fundamentally intertwined with the mechanisms underlying ultrafast photophysical processes in biological systems and chiral materials. Extending our static understanding of chirality to a dynamic perspective is critical for the rational design of next-generation chiral materials. Chiral two-dimensional electronic spectroscopy (2DES) provides the insight required to identify key couplings driving the chiral response by mapping the excited state's evolution onto an excitation and emission energy 2D correlation map with femtosecond temporal resolution [1]. However, routine execution of chiral 2DES has been hindered by the experimental difficulty of isolating the inherently weak chiral response from the dominant achiral response. Here, we report chiral 2DES of helical porphyrin J-aggregates. The chiral 2D spectra show enhanced spectral resolution and reveal unique information about the system's excitonic chirality. The spectra are collected with a 2DES instrument that leverages the axes of birefringent crystals to generate background-free chiral signals, eliminating parasitic achiral artifacts. We demonstrate the purity of the measured response by showing mirror-image symmetry between chiral 2D spectra of aggregate enantiomers. Chiral 2DES is established as a powerful tool for probing ultrafast chiral photophysics.

4.2 Introduction

A system is chiral if it cannot be superimposed on its mirror image under any combination of rotations and translations in three-dimensional space. Chirality is inherent in biological systems, with nature exhibiting a preference for a particular handedness in biomolecules and helical structures. Chirality is also increasingly incorporated as a design parameter to expand the functional capabilities of materials and devices across wide-ranging fields, including 2D and topological materials [3–5], valleytronics and quantum information [6–9], biosensing [10, 11], solar energy [12–14], spintronics [15–18], and plasmonics [19–21]. Crucially, chirality is not merely a static structural property, it actively governs the excited state dynamics of the system [22–24]. Understanding how chirality influences ultrafast photophysical processes, such as energy and charge transfer, relaxation, coherence, and emission, is therefore essential for both designing next-generation chiral materials and elucidating the photophysics of biological systems.

Probing ultrafast chiral dynamics requires combining circular dichroism (CD) with time-resolved spectroscopy. CD measures the differential absorption of left- and right-circularly polarized light by a chiral sample, while time-resolved spectroscopy monitors pump-induced changes in probe absorption as a function of the time delay between the pump and probe pulses. Combining these two techniques is challenging, because chiral signals are several orders of magnitude weaker than the achiral signals of conventional time-resolved measurements, which are already weak perturbative effects. In transient absorption (TA) spectroscopy, the most straightforward time-resolved technique, recent experimental developments have largely overcome the susceptibility of the weak chiral signal to laser source instability, polarization impurity, and pump-induced artifacts to enable collection of time-resolved CD (TRCD) spectra with high sensitivity, broadband excitation, and ultrafast temporal resolution [22, 25–27].

Chiral two-dimensional electronic spectroscopy (2DES) provides deeper insight into how

chirality influences excited state photophysics by recovering excitation frequency resolution unavailable to TRCD. 2DES is a time-resolved technique like TA, but it also resolves the pump excitation frequency, effectively separating the information contained in a TA spectrum along an extra dimension and creating a two-dimensional correlation map of excitation and emission frequencies. 2DES can elucidate electronic and vibrational couplings and coherences, energy transfer rates, and timescales of environmental interactions [1]. Chiral 2DES has been explored extensively in theoretical and computational works [28–30]. However, its experimental realization remains limited to a single study of a biological system that exists in only one enantiomeric form [31], precluding direct comparison between enantiomers and leaving significant opportunity for experimental development.

Here, we interrogate the excitonic chirality of helical porphyrin J-aggregates using chiral 2DES. The aggregates are comprised of achiral meso-tetrakis-(4-sulfonatophenyl)porphyrin (TPPS) monomers that stack head-to-tail with a slight angle offset in the presence of L- or D-valine, creating helical chains of different handedness that stack to form nanotubes (Figure 4.1a-d). Using a chiral 2DES instrument that exploits the natural optical axes of birefringent crystals to achieve exquisite chiral sensitivity, we examine the excitonic chirality in the Q-band region (660-750 nm), which arises from the helical arrangement of coupled monomer transition dipoles [32]. We show that chiral 2DES enhances spectral resolution and amplifies weak transitions relative to traditional 2DES, allowing identification of spectral features that are otherwise obscured. The chiral 2D spectra directly report on the rotational strength of the transitions that give rise to the spectral features, revealing their handedness, i.e., their preferential coupling to either right- or left-handed circularly polarized light. Successful isolation of the chiral signal is evidenced by a clear mirror image sign inversion between enantiomers. Finally, we propose Feynman pathways to aid in the clear interpretation of spectral features in the chiral 2D spectra. Overall, our application of chiral 2DES to helical porphyrin aggregates establishes its power as a tool to improve spectral

resolution, reveal weak transitions, and interrogate the fundamental chirality of transitions between electronic states.

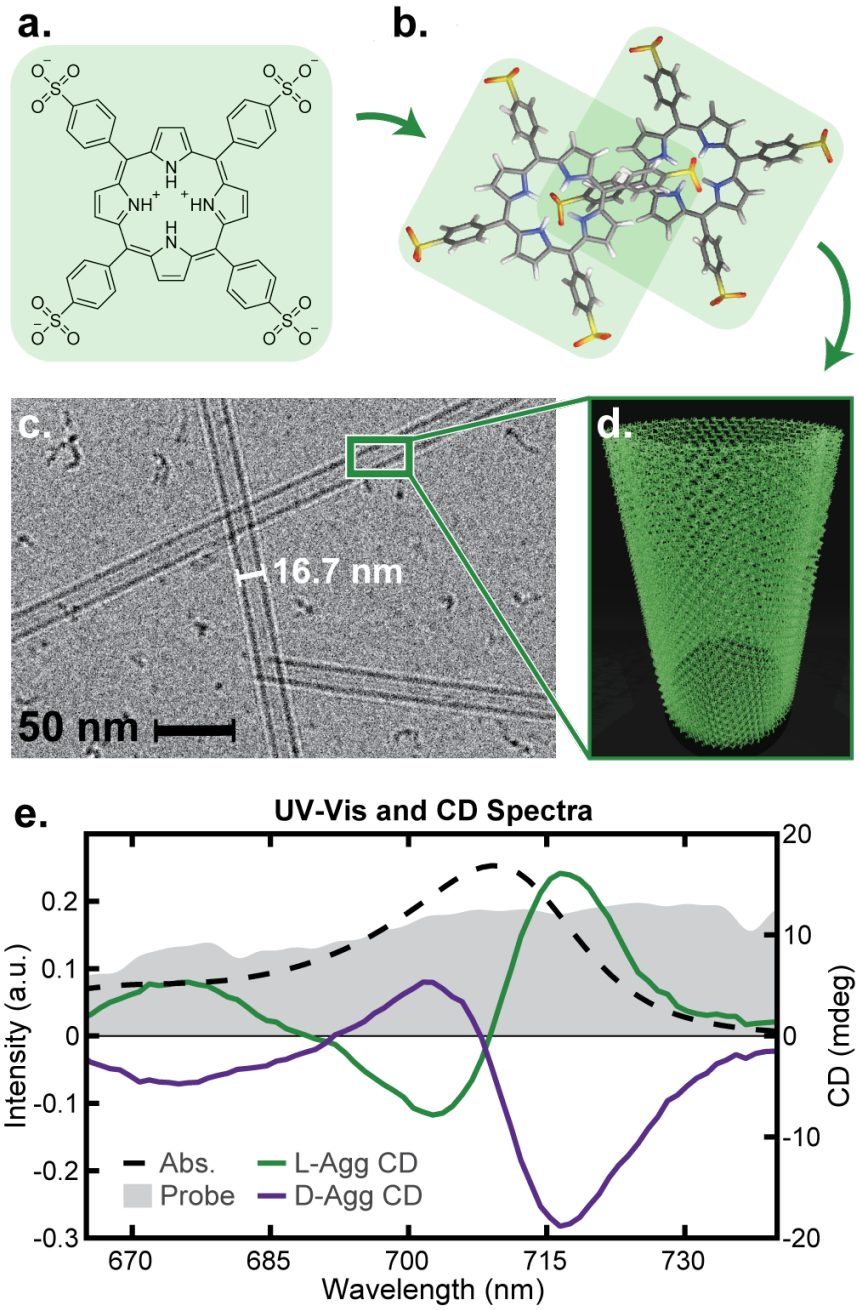

Figure 4.1: Spectral and Structural Characterization of Chiral TPPS J-Aggregates. (a) Chemical structure of the meso-tetrakis-(4-sulfonatophenyl)porphyrin (TPPS) monomer. (b) Depiction of a TPPS J-aggregate dimer subunit. (c) Cryo-transmission electron microscopy imaging of the L-TPPS aggregate, forming 16.7 nm diameter single walled nanotubes. (d) Schematic of a L-TPPS aggregate, depicted here as a 26-start helix with 3.6 angstrom vertical spacing and 5° angle between monomers based on literature values reported for a similar aggregate [2]. (e) Absorption and circular dichroism spectra of L-TPPS and D-TPPS aggregates, overlaid with the probe spectrum used in this work.

4.3 Instrument Approach

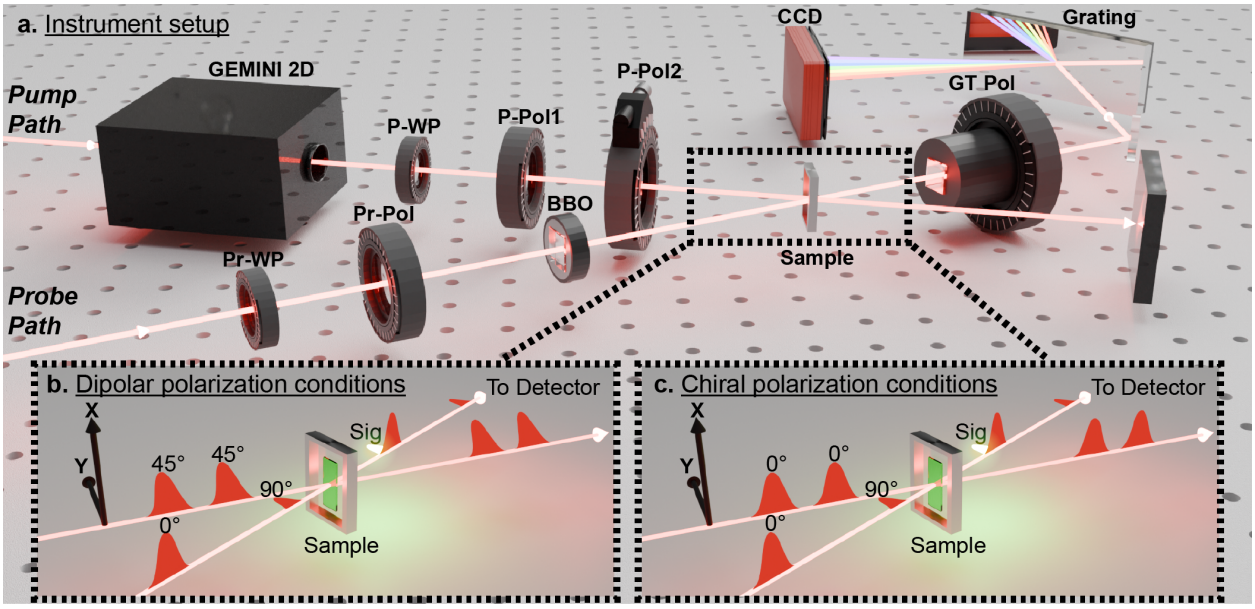

Figure 4.2: Overview of Chiral Two-dimensional Electronic (2DES) Spectrometer. (a) Simplified schematic of the chiral transient absorption (TA) and 2DES instrument. An orthogonal probe and local oscillator pulse pair with a constant delay of 1.1 ps is generated by passing the pulse through an α-BBO crystal of fixed thickness. A half-waveplate (Pr-WP) and polarizer (Pr-Pol) rotate the input polarization to control the ratio of probe to local oscillator and improve polarization purity, respectively. A phase-stable, orthogonal pump pulse pair with tunable delay is generated with the Gemini 2D by NIREOS. A half-waveplate (P-WP) then rotates the pump pulse pair relative to the probe and local oscillator pulse pair, and a polarizer (P-Pol1) then projects the pump pulses in equal amount onto a parallel polarization. Finally, a polarizer (P-Pol2) in a precision rotation mount (Thorlabs) improves polarization purity and aligns the pump pulses with either the probe polarization (in the chiral polarization condition) or 45° relative to the probe polarization (in the dipolar polarization condition). After passing through the sample, a high extinction ratio Glan-Thompson polarizer (GT Pol) filters out the probe background and passes the orthogonal local oscillator and emitted signal, which is heterodyne-detected with a spectrometer and charge-coupled device (CCD). (b) Polarization conditions for collecting the dipolar signal: $(45°, 45°, 0°, 90°)$. (c) Polarization conditions for collecting the chiral signal: $(0°, 0°, 0°, 90°)$.

4.3.1 Isolating the Chiral Component of the Third-Order Response

The signal measured in a TA or 2DES experiment is the nonlinear third-order response of the system following interaction with the excitation and detection electric fields. This

response contains information about photophysical processes of interest, including ground state bleaching (GSB), stimulated emission (SE), and excited-state absorption (ESA). The third-order response is conventionally expressed within the electric dipole approximation, which neglects both the spatial dependence of the incident electric fields and all interactions with the magnetic field. This approximation is justified because such contributions to the molecular response are two to five orders of magnitude smaller than those arising from electric dipole interactions [33]. However, only the response components arising from these weak spatially-dependent electric and magnetic field interactions change sign under spatial inversion and thus report on the system's chirality. Consequently, it is necessary to move beyond the electric dipole approximation to understand the theoretical origin of a chiral response, i.e. how systems of opposite chirality can yield different signals. In turn, experimental techniques are insensitive to molecular handedness unless the large electric dipole response can be eliminated to reveal the weaker chiral components.

Here, we isolate the chiral component of the response by employing the pulse polarization condition first proposed by Abramavicius and Mukamel [34] and utilized by Fidler and coworkers [31]: $(0°, 0°, 0°, 90°)$ (Figure 4.2c), where the notation $(\theta_1, \theta_2, \theta_3, \theta_4)$ gives the polarization of the two collinear pump pulses followed by the polarization of the collinear probe and local oscillator pulses. In odd polarization conditions such as this one, comprised of three parallel pulses and one orthogonal pulse, only terms of the molecular response that change sign upon spatial inversion survive the rotational average over different orientations in an isotropic ensemble. Therefore, any odd polarization condition isolates chiral components of the response. By contrast, the dipolar response is collected with even pulse polarization conditions such as $(45°, 45°, 0°, 90°)$ (Figure 4.2b) [35]. This polarization condition can be decomposed into the two even polarization conditions $(0°, 90°, 0°, 90°)$ and $(90°, 0°, 0°, 90°)$, which enable the large probe background to be filtered out by polarization discrimination.

4.3.2 Chiral Two-Dimensional Electronic Spectrometer Design

The dipolar and chiral polarization conditions are implemented experimentally by generating purely orthogonal pulse pairs with birefringent crystals and then manipulating them with half-waveplates and polarizers (Figure 4.2a). The 2DES setup employs a partially collinear geometry in which collinear pumps are crossed in the sample with a collinear probe and time-separated local oscillator (LO). In the probe path, the beam travels through an α-BBO crystal with a fixed thickness, where the difference in index of refraction along the ordinary and extraordinary crystal axes splits the transmitted beam into two orthogonally polarized components with a 1.1 ps time delay. The leading pulse serves as the local oscillator, while the lagging pulse is the probe. A half-waveplate and polarizer control the probe-to-local-oscillator ratio by rotating the polarization of the input beam relative to the α-BBO crystal axes. In the pump path, a modified NIREOS GEMINI-2D creates a phase-stable orthogonal pulse pair with a precisely tunable delay using a series of birefringent wedges. A half-waveplate rotates the pump pulse pair relative to the probe. Two polarizers then project the pump pulses onto a common axis in equal amounts, fine-tuning the final polarization to be precisely parallel to the probe with a high extinction ratio. In addition, rearranging the half-waveplates and polarizers in the two paths allows for implementation of any of the following chiral polarization conditions with high purity: $(90°, 0°, 0°, 0°)$, $(0°, 90°, 0°, 0°)$, and $(0°, 0°, 90°, 0°)$. Transient absorption measurements are natively heterodyne-detected in the same experimental setup by adjusting the polarizers in the pump path to eliminate one of the two pulses. For a given polarization condition, the only experimental change between measurements is the replacement of the sample with its enantiomer.

Our instrument is designed to mitigate the effects of small polarization errors and impurities, which can introduce dipolar signal contamination from the $(0°, 90°, 0°, 90°)$ and $(90°, 0°, 0°, 90°)$ polarization conditions and can quickly obscure and distort weak chiral signals. Utilizing a partially collinear geometry provides an advantage over the fully non-

collinear geometry previously reported by Fidler and coworkers [31] because it decreases the number of pulse polarizations that must be manually aligned relative to each other. Polarization purity is maximized through careful optical ordering: high-fidelity polarizers follow the more wavelength-dependent half waveplates, final polarization optics follow silver mirrors that necessarily introduce elliptical polarization impurities, and samples are mounted in custom holders that reduce strain-induced birefringence. With these considerations, we achieved a polarization extinction ratio for the pump pulse pair of 352:1 with the chiral polarization condition and 151:1 with the dipolar polarization condition.

4.4 Results

Dipolar and chiral 2DES frames at a waiting time of 200 fs and full TA spectra for both the TPPS L- and D-aggregates are reported in Figure 4.3. The real component of the isolated electric field is shown.

4.4.1 Sign Inversion of Chiral Signal Between Enantiomers

The relative signs and magnitudes of the 2DES and TA signals indicate that the chiral polarization conditions successfully isolated the chiral components of the third-order nonlinear response. Firstly, the chiral 2DES and TA spectra exhibit clear sign inversion of the real signal amplitude between the two enantiomers for all features above the signal-to-noise (SNR) ratio (Figure 4.3). Overlaying emission energy slices for the two enantiomers reveals mirror image symmetry consistent with minimal dipolar contamination of the chiral signal. As a control, traditional dipolar measurements were also carried out for each enantiomer. These spectra were nearly identical between the enantiomers, suggesting that any difference in dipolar electronic state features between the samples is negligible.

Comparing the relative signal strength between the chiral and dipolar data is an additional way to confirm the measurement purity. The ratio of maximum real dipolar signal

strength to maximum real chiral signal strength at the earliest available waiting time of 200 fs in the 2D data is 544:1 for the TPPS L-aggregate and 839:1 for the TPPS D-Aggregate. This drastic reduction in overall aggregate signal strength between the dipolar and chiral polarization conditions indicates that the dipolar signal is almost entirely suppressed, leaving only the weak chiral signal.

4.4.2 Spectral Features Under Chiral vs. Dipolar Polarization Conditions

Under both dipolar and chiral polarization conditions, the 2DES and TA spectra exhibit a dominant GSB/SE transition centered near 712 nm (labeled as Feature B in Figure 4.4a), accompanied by a broad, blue-shifted ESA feature that peaks near 690 nm and extends along the emission axis to the bluest end of our spectral range (labeled as Feature D in Figure 4.4a). Qualitatively, these spectral features do not differ between polarization conditions. The 2DES spectra additionally contain a diagonal peak and two cross peaks (CPs) that have different signs and/or shapes under chiral polarization conditions relative to the same feature under dipolar polarization conditions. Since these CPs have a positive sign under dipolar polarization conditions, they could arise from either coupling or fast downhill energy transfer and vibrational cooling within the Q-band manifold. If these features arise due to coupling, then symmetric positive features should also appear above the diagonal. However, since those regions overlap with ESA features, it is possible that no such positive diagonal features are observed simply due to cancellation with the ESAs.

One CP is located at an emission wavelength of 712 nm and spans excitation wavelengths from 712 nm to 670 nm (labeled as Feature E in Figure 4.4a). Under chiral polarization conditions, Feature E becomes more resolved from the main diagonal Feature B. In the dipolar response, the amplitude extends continuously from the main peak and gradually decreases at lower excitation wavelengths. In the chiral response, the peak is more rounded and localized, with a small but apparent dip in amplitude between the main diagonal bleach

and the CP. This localization in the chiral CP likely arises from a change in sign of a diagonal bleach feature at approximately 700 nm (labeled Feature A in Figure 4.4a). Overlap between the opposite amplitude diagonal Feature A at 700 nm with an intermediate portion of the broad Feature E CP leads to partial amplitude cancellation between the features, producing a more rounded CP line shape and enhancing the apparent resolution.

The second CP lies in the region just below the main 712 nm diagonal peak at an emission wavelength of approximately 735 nm (labeled as Feature C in Figure 4.4a). Feature C is comparatively narrower and substantially weaker in amplitude than Feature E. Feature C changes sign relative to the main diagonal peak under chiral polarization conditions as compared to dipolar polarization conditions. In the dipolar response, both Feature B and Feature C are positive. But in the chiral response, Feature B and Feature C have opposite signs. Similarly to Feature E, this results in a cancellation of amplitude that causes Feature C to be more localized and better resolved in the chiral spectra.

4.4.3 Assignment of Spectral Features to Aggregate Photophysics

Based on a combination of 2DES, UV-Vis, and fluorescence data, the relevant electronic states of the TPPS aggregate are given in Figure 4.4b. Briefly, three manifolds of singlet states exist in the near IR to near UV wavelength range: the Q-band ($|S_1\rangle$) centered near 712 nm, the Soret or B-band ($|S_2\rangle$) from 400 to 500 nm, and a band of higher-lying states ($|S_3\rangle$) with excitation wavelengths less than 300 nm. Note that the one-exciton $|S_3\rangle$ states overlap in energy with two-exciton states $|S_1, S_1\rangle$ comprised of two excitations into the Q-band [36]. In our steady-state CD measurement, we resolved three primary resonances within our 2DES spectral range, centered at approximately 675, 704, and 709 nm. The diagonal peaks, Features A and B, correspond to the two lowest energy steady-state CD transitions. The highest energy transition at 675 nm is not observable on the diagonal of our 2DES data. The absence of this feature can be attributed to overlap and cancellation with the above

diagonal ESA and/or decay of the state's population at a faster timescale than measured by our experiment.

To further understand the photophysics underlying the observed spectral features, we employ analysis with Feynman pathways, which graphically trace the evolution of the density matrix of the system through its interactions with each of the electric fields. Let us consider Feature C, the below-diagonal cross peak present in the chiral spectra at 712 nm excitation and 735 nm emission that changes sign relative to Feature B under chiral versus dipolar polarization conditions. Since the signs of chiral features do not unambiguously differentiate between ESA and GSB/SE, all three types of pathways could plausibly give rise to this feature. Possible Feynman diagrams for Feature C under chiral polarization conditions are given in Figure 4.4c.

The lowest energy electronic transition observed in the linear absorption and CD spectra is centered in the 712-715 nm range (Figure 4.1e). This agrees well with models of similar porphyrin J-aggregates from literature, which assign the main peak at 707 nm as the lowest energy Q band transition [36, 37]. However, there is a small but non-negligible intensity in both spectra at longer wavelengths up to 740 nm. As such, a GSB or SE process involving a transition between the ground state $|S_0\rangle$ and a $|S_1\rangle$ band edge state near 735 nm is possible but would likely be quite weak. Another possibility is an SE from the bright 712 nm Q-band state to a vibronically hot ground state (Figure 4.4ci). This would correspond to a positive feature under dipolar polarization conditions, which agrees with our results. Using fluorescence spectroscopy, we resolved spontaneous emission from approximately 735 nm following excitation at higher energies, confirming that Feature C can arise from SE. Alternatively, Feature C can be attributed to an excited state absorption from the 712 nm state to higher-lying excited states (Figure 4.4cii). While no negative ESA feature was observed at this location in our dipolar spectra, this does not necessarily rule out the possibility, as an ESA could be present but canceled out by stronger positive amplitude

features. Depending on which of these photophysical processes gives rise to Feature C, its sign under chiral polarization conditions can provide different insights into the chirality of the underlying transitions.

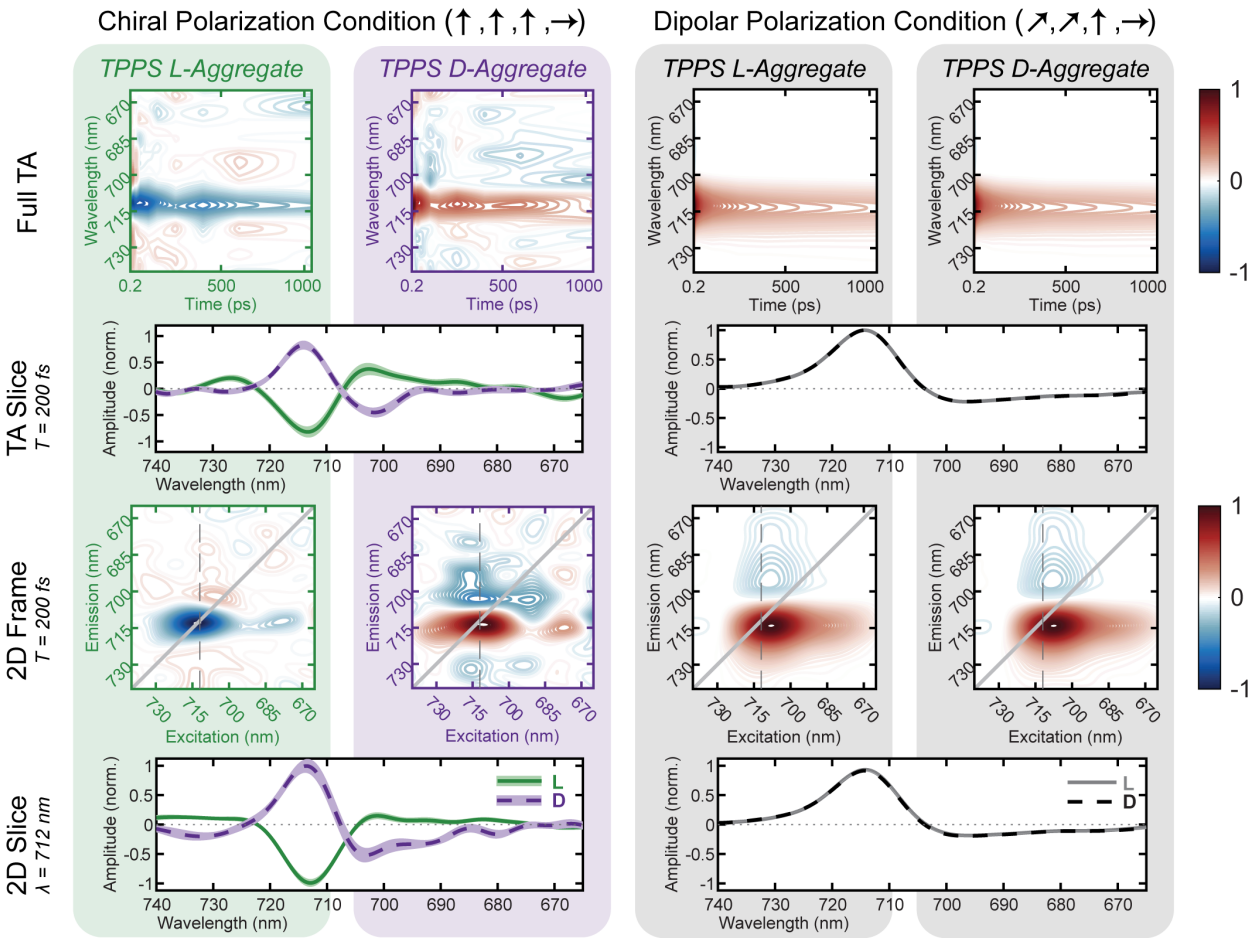

Figure 4.3: TA and 2DES data under chiral and dipolar polarization conditions for the TPPS L- and D-Aggregates. Spectra of the TPPS L-Aggregate under the chiral polarization condition are denoted in green (first column); spectra of the TPPS D-Aggregate under the chiral polarization condition are denoted in purple (second column). Spectra of the TPPS L- and D-Aggregates under the dipolar polarization conditions are denoted in black and gray (third and fourth columns). All spectra are normalized. Full TA spectra (over 200 fs to 1 ns) are shown in the first row. Slices through the TA spectra at 200 fs are shown in the second row. Real-valued, absorptive 2DES frames at 200 fs are shown in the third row. Slices through the 2D frames at an excitation wavelength of 712 nm (marked as a dotted gray line in the 2DES frames) are shown in the fourth row. Error bars reporting the standard error of the mean are reported for the chiral polarization conditions. Error bars for the dipolar polarization conditions are too small to be visible here.

4.5 Discussion

To understand what the sign of the chiral signal reveals about the system's excitonic chirality, we must consider more generally what information is contained in the chiral response. In conventional dipolar 2DES and TA measurements, positive signal amplitudes correspond to SE or GSB pathways, whereas negative signal amplitudes correspond to ESA pathways. Peak intensities are governed by the product of transition dipoles associated with the four field interactions in a given Liouville pathway. For example, in a diagonal GSB pathway between ground state, $|g\rangle$, and first excited state, $|a\rangle$, the peak signal intensity scales with the fourth power of the $|g\rangle \leftrightarrow |a\rangle$ transition dipole strength, $|\mu_{ag}|^4$. However, under chiral polarization conditions, the sign of the signal no longer directly translates to SE/GSB or ESA transitions. Chiral 2DES and TA measurements can be understood as a double difference measurement: the difference in absorption with and without pump excitation is combined with the difference in absorption of right- and left-circularly polarized light for a given field interaction. Thus, the signal can be interpreted as the subtraction of two Feynman diagrams, where the respective fourth interactions are with left- and right-circularly polarized light (Figure 4.4c). Alternatively, this can be understood by expressing the orthogonal pulse as a linear combination of left- and right-circularly polarized light: for example, with $\vec{V} \propto \vec{L} - \vec{R}$, the chiral polarization condition $(0°, 0°, 0°, 90°)$ is equivalent to taking the difference of $(0°, 0°, 0°, R)$ and $(0°, 0°, 0°, L)$ [38]. As a result, two features that have the same sign in the dipolar 2DES and TA spectra, such as two positive-signed features arising from SE, can have opposite signs in chiral spectra. While the dipolar and chiral 2DES measurements measure the same transition energies, the amplitudes and signs of features are governed by the chiral response, which includes both electric and effective magnetic transition dipole terms. In the TPPS J-aggregates studied here, the origin of chirality is excitonic in nature, and as such, rotational strength arises from the relative orientations and separation between transition dipoles, $r_{ij} \cdot (\mu_i \times \mu_j)$.

Sign variation across neighboring peaks can enhance the resolution of spectrally congested features in the same way that steady-state CD improves resolution. Neighboring peaks that are not resolvable when they are the same sign become clearly resolved when they are opposite signs, since cancellation between the features creates a node. As noted above, this resolution enhancement can be seen in Feature E in the chiral spectra, which we hypothesize has the same sign as Feature A under dipolar polarization conditions, but the opposite sign as Feature A under chiral polarization conditions. This interpretation is supported by comparison to the linear CD spectrum, which directly measures the rotational strengths for transitions from the ground state to the one-exciton manifold. In the chiral probe polarization conditions utilized in this experiment, the emitted signal is related to the rotational strength of the final electronic transition, though this transition may include the two-exciton manifold as well. In the case of diagonal GSB or SE features, these transitions are between the ground and one-exciton manifold, so the associated rotational strengths and relative signs of features in the chiral 2DES spectra correspond to those measured with steady-state CD [39]. Consequently, the linear CD spectra suggest Features B and A should have opposite signs under chiral polarization conditions.

Finally, we comment further on the interpretation of Feature C. In the case that Feature C is an SE to a hot ground state, the last Feynman pathway interaction couples the $S_0' \leftrightarrow S_1$ states, indicating that this transition results from a differential interaction between left- and right- circularly polarized light. Interestingly, this feature is a different sign than the main diagonal Feature B, suggesting that the $S_0' \leftrightarrow S_1$ transition has a different handedness or chirality than the $S_0 \leftrightarrow S_1$ transition. In contrast, if this feature arises from the ESA pathway, then the chiral interaction involves a transition from S_1 to a higher-lying excited state, providing unique insight into the chirality of the excited state, rather than just the ground state as in steady-state CD.

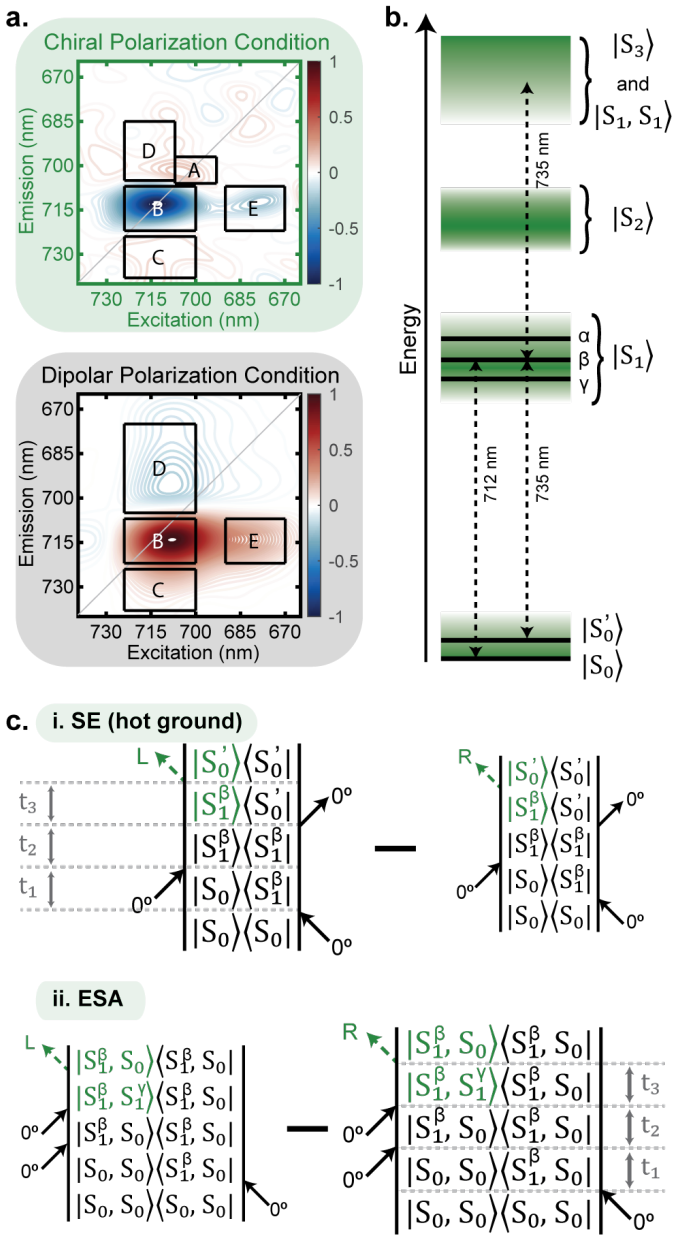

Figure 4.4: Interpretation of TPPS Aggregate Nonlinear Chiral Signal. (a) 2DES Frames of TPPS L-Aggregate with boxes marking primary features observed under chiral (Features A, B, C, D, and E) and dipolar (Features B, C, D, and E) polarization conditions. (b) Energy level diagram of TPPS aggregates, illustrating Feature C's two candidate emission transitions at 735 nm and excitation transition at 712 nm. (c) Proposed Feynman diagrams for Feature C as a (i) stimulated emission to a hot vibronic ground state and excited state absorption (ii) from the $|S_1\rangle$ band to higher energy one-exciton states in $|S_3\rangle$ band.

4.6 Conclusion

In this work, chiral 2DES was employed to interrogate the excitonic chirality of helical porphyrin J-aggregates. Differences in relative sign and amplitude of spectral features in the chiral and dipolar 2D spectra were observed. Conceptually, these differences can be understood as arising from the relative orientations of monomer transition dipoles, which give rise to electronic transitions that couple more strongly to either left- or right-circularly polarized light. The chiral 2D spectra displayed increased spectral resolution, amplified certain weak features, and informed about the rotational strength of excitonic transitions in both the ground and excited states. The fidelity of the chiral signal is evident in the first demonstration of a mirror-image sign inversion of the 2D signal between enantiomers. To achieve this, a novel instrument was introduced for measurement of the chiral third-order nonlinear response that utilizes the axes of birefringent crystals to generate an orthogonal pulse pair with high polarization purity. Overall, the experimental techniques presented here constitute a valuable new tool for studying the intricate interplay between chirality and electronic dynamics. Application of chiral 2DES is now set to provide new insights into both design and function of natural and engineered chiral systems.

References

(1) Fresch, E.; Camargo, F. V. A.; Shen, Q.; Bellora, C. C.; Pullerits, T.; Engel, G. S.; Cerullo, G.; Collini, E. Two-dimensional electronic spectroscopy. *Nature Reviews Methods Primers* **2023**, *3*, 84.

(2) Short, J. M.; Berriman, J. A.; Kübel, C.; El-Hachemi, Z.; Naubron, J.-V.; Balaban, T. S. Electron Cryo-Microscopy of $TPPS_4$·2HCl Tubes Reveals a Helical Organisation Explaining the Origin of their Chirality. *ChemPhysChem* **2013**, *14*, 3209–3214.

(3) Rong, R.; Liu, Y.; Nie, X.; Zhang, W.; Zhang, Z.; Liu, Y.; Guo, W. The interaction of 2D materials with circularly polarized light. *Advanced Science* **2023**, *10*, 2206191.

(4) Bao, C.; Tang, P.; Sun, D.; Zhou, S. Light-induced emergent phenomena in 2D materials and topological materials. *Nature Reviews Physics* **2022**, *4*, 33–48.

(5) Zhu, H.; Yakobson, B. I. Creating chirality in the nearly two dimensions. *Nature Materials* **2024**, *23*, 316–322.

(6) Mak, K. F.; He, K.; Shan, J.; Heinz, T. F. Control of valley polarization in monolayer MoS2 by optical helicity. *Nature nanotechnology* **2012**, *7*, 494–498.

(7) Vitale, S. A.; Nezich, D.; Varghese, J. O.; Kim, P.; Gedik, N.; Jarillo-Herrero, P.; Xiao, D.; Rothschild, M. Valleytronics: opportunities, challenges, and paths forward. *Small* **2018**, *14*, 1801483.

(8) Liu, J.-W.; Liu, G.-G.; Zhang, B.; Mo, H.-C.; Li, R.; Li, M.; Chen, X.-D.; Zhang, B.; Chen, W.-J.; Dong, J.-W. Chiral valley edge states based on Dirac mass engineering. *Nature Communications* **2025**.

(9) Jiang, H.; Zhang, Y.; An, L.; Tan, Q.; Dai, X.; Chen, Y.; Chen, W.; Cai, H.; Fu, J.; Zúñiga-Pérez, J., et al. Chiral light detection with centrosymmetric-metamaterial-assisted valleytronics. *Nature Materials* **2025**, *24*, 861–867.

(10) Ziv, A.; Shoseyov, O.; Karadan, P.; Bloom, B. P.; Goldring, S.; Metzger, T.; Yochelis, S.; Waldeck, D. H.; Yerushalmi, R.; Paltiel, Y. Chirality nanosensor with direct electric readout by coupling of nanofloret localized plasmons with electronic transport. *Nano Letters* **2021**, *21*, 6496–6503.

(11) Ouyang, Y.-C.; Yeom, B.-J.; Zhao, Y.; Ma, W. Progress and prospects of chiral nanomaterials for biosensing platforms. *Rare Metals* **2024**, *43*, 2469–2497.

(12) Xue, G.; Zhou, Z.; Guo, Q.; Zuo, Y.; Wei, W.; Yang, J.; Yin, P.; Zhang, S.; Zhong, D.; You, Y., et al. WS2 ribbon arrays with defined chirality and coherent polarity. *Science* **2024**, *384*, 1100–1104.

(13) Fu, W.; Gao, Q.; Zhang, C.; Tan, L.; Jiang, B.; Xiao, C.; Liu, M.; Wang, P.-p. Exploring Geometric Chirality in Nanocrystals for Boosting Solar-to-Hydrogen Conversion. *Angewandte Chemie International Edition* **2024**, *63*, e202411871.

(14) Han, J.; Dai, X.; Hettiarachchi, S.; The, Z. L.; Park, S.; Chen, S.; Veettil, B. P.; Huang, S.; Kim, D. J.; Kim, J. High-Performance Perovskite Solar Cell via Chirality-Engineered Graphene Quantum Dot Interface Passivation. *Solar RRL* **2024**, *8*, 2400367.

(15) Suda, M.; Thathong, Y.; Promarak, V.; Kojima, H.; Nakamura, M.; Shiraogawa, T.; Ehara, M.; Yamamoto, H. M. Light-driven molecular switch for reconfigurable spin filters. *Nature communications* **2019**, *10*, 2455.

(16) Zhu, Q.; Danowski, W.; Mondal, A. K.; Tassinari, F.; van Beek, C. L.; Heideman, G. H.; Santra, K.; Cohen, S. R.; Feringa, B. L.; Naaman, R. Multistate switching of spin selectivity in electron transport through light-driven molecular motors. *Advanced science* **2021**, *8*, 2101773.

(17) Oppermann, M.; Zinna, F.; Lacour, J.; Chergui, M. Chiral control of spin-crossover dynamics in Fe (II) complexes. *Nature Chemistry* **2022**, *14*, 739–745.

(18) Babu, R.; Heger, J. E.; Dutta, T.; Hu, X.; Pradhan, N.; Muller-Buschbaum, P.; Gómez-Graña, S.; Polavarapu, L. Chiral Molecules in Action: Chemistry of Chiral Perovskite and Perovskite-Inspired Materials. *ACS Energy Letters* **2025**, *10*, 5703–5721.

(19) Hentschel, M.; Schäferling, M.; Duan, X.; Giessen, H.; Liu, N. Chiral plasmonics. *Science advances* **2017**, *3*, e1602735.

(20) Zheng, J.; Fu, Y.; Wang, J.; Zhang, W.; Lu, X.; Lin, H.-Q.; Shao, L.; Wang, J. Circularly polarized OLEDs from chiral plasmonic nanoparticle-molecule hybrids. *Nature Communications* **2025**, *16*, 1658.

(21) Kuzyk, A.; Schreiber, R.; Fan, Z.; Pardatscher, G.; Roller, E.-M.; Högele, A.; Simmel, F. C.; Govorov, A. O.; Liedl, T. DNA-based self-assembly of chiral plasmonic nanostructures with tailored optical response. *Nature* **2012**, *483*, 311–314.

(22) Liu, H.; Ouyang, M. Chirality-driven spin dynamics and manipulation in all-inorganic chiral heterostructures. *Nature Communications* **2025**, *16*, 8382.

(23) Mantel, G. C.; Kairys, K. T.; Williams, M. L.; Krzyaniak, M. D.; Young, R. M.; Tempelaar, R.; Wasielewski, M. R. Effect of chirality on ultrafast triplet exciton formation in electron donor–acceptor cocrystals. *Journal of the American Chemical Society* **2025**, *147*, 29592–29601.

(24) Tong, L.; Xie, F.; Gao, X.; Chen, Y.; Ji, S.; Zhang, B.; Li, J.; Guo, J.; Liu, F.; Gao, C., et al. Deciphering light transformation in chiral metasurface in real space and time by ultrafast electron microscopy. *Light: Science & Applications* **2026**, *15*, 70.

(25) Monti, M.; Biancorosso, L.; Coccia, E. Time-resolved circular dichroism in molecules: experimental and theoretical advances. *Molecules* **2024**, *29*, 4049.

(26) Cui, T.; Wang, X.; Pan, H.; Chen, J. Unravel excited state chirality dynamics during symmetry-breaking charge separation. *Science China Materials* **2026**, 1–7.

(27) Schirato, A.; Crotti, G.; Kim, R. M.; Lee, S. M.; Han, J. H.; Villa, A.; Ali, D.; Rizzo, A.; Maiuri, M.; Nam, K. T., et al. Broadband ultrafast self-heterodyned chiro-optical spectroscopy. *arXiv preprint arXiv:2511.10574* **2025**.

(28) Liu, Z.; Jha, A.; Liang, X.-T.; Duan, H.-G. Transient chiral dynamics revealed by two-dimensional circular dichroism spectroscopy. *Phys. Rev. E* **2023**, *107*, 054119.

(29) Liu, Z.; Zhang, P.; Mei, C.; Liang, X.-T.; Jha, A.; Duan, H.-G. Transient Chiral Dynamics in the Fenna–Matthews–Olson Complex Revealed by Two-Dimensional Circular Dichroism Spectroscopy. *The Journal of Physical Chemistry Letters* **2024**, *15*, PMID: 38885182, 6550–6559.

(30) Yang, Y.; Liu, Z.; Zheng, F.; Zhang, P.; He, H.; Jha, A.; Duan, H.-G. Diverse Transient Chiral Dynamics in Evolutionary Distinct Photosynthetic Reaction Centers. *Journal of Chemical Theory and Computation* **2025**, *21*, PMID: 39718439, 321–332.

(31) Fidler, A. F.; Singh, V. P.; Long, P. D.; Dahlberg, P. D.; Engel, G. S. Dynamic localization of electronic excitation in photosynthetic complexes revealed with chiral two-dimensional spectroscopy. *Nature communications* **2014**, *5*, 3286.

(32) Didraga, C.; Knoester, J. Optical spectra and localization of excitons in inhomogeneous helical cylindrical aggregates. *The Journal of chemical physics* **2004**, *121*, 10687–10698.

(33) Berova, N.; Nakanishi, K.; Woody, R. W. *Circular dichroism: principles and applications*; John Wiley & Sons: 2000.

(34) Abramavicius, D.; Mukamel, S. Coherent third-order spectroscopic probes of molecular chirality. *The Journal of Chemical Physics* **2005**, *122*, 134305.

(35) Fuller, F. D.; Wilcox, D. E.; Ogilvie, J. P. Pulse shaping based two-dimensional electronic spectroscopy in a background free geometry. *Optics Express* **2014**, *22*, 1018–1027.

(36) Wan, Y.; Stradomska, A.; Fong, S.; Guo, Z.; Schaller, R. D.; Wiederrecht, G. P.; Knoester, J.; Huang, L. Exciton level structure and dynamics in tubular porphyrin aggregates. *The Journal of Physical Chemistry C* **2014**, *118*, 24854–24865.

(37) Stradomska, A.; Knoester, J. Shape of the Q band in the absorption spectra of porphyrin nanotubes: Vibronic coupling or exciton effects? *The Journal of Chemical Physics* **2010**, *133*.

(38) Choi, J.-H.; Cho, M. Quadrupole contribution to the third-order optical activity spectroscopy. *The Journal of Chemical Physics* **2007**, *127*, 024507.

(39) Choi, J.-H.; Cho, M. Nonlinear optical activity measurement spectroscopy of coupled multi-chromophore systems. *Chemical Physics* **2007**, *341*, Ultrafast Dynamics of Molecules in the Condensed Phase: Photon Echoes and Coupled Excitations, 57–70.

CHAPTER 5

FUTURE DIRECTIONS

5.1 Single-Experiment Measurement of Multiple Polarization Conditions

The 2DES setup presented in this thesis employs a modified pump-probe geometry in which a time-separated local oscillator (LO) heterodynes the emitted third-order signal, thereby preserving the spectral phase that would be lost by homodyne detection. This configuration is particularly advantageous for polarization conditions in which the probe and LO are orthogonally polarized. Under these conditions, a Glan-Thompson polarizer positioned immediately downstream of the sample acts as an analyzer, transmitting the LO and emitted signal components aligned with its transmission axis while rejecting the orthogonally polarized probe field. Blocking the probe from reaching the detector prevents detector saturation without requiring additional attenuation that would also reduce the detected amplitude of the emitted signal. This section examines an alternative detection strategy in which the Glan-Thompson polarizer is removed. Without the analyzer, multiple polarization-dependent signal contributions can reach the detector within a single measurement, potentially reducing the total acquisition time by a factor of two.

When the Glan-Thompson polarizer is removed from the detection beam path, both the probe and LO fields reach the detector. The emitted third-order signal can therefore be heterodyne detected by both fields. Because the probe and LO are temporally separated by approximately 1.1 ps, their respective heterodyne-detected fields are also separated by 1.1 ps in the detection time domain. The LO-heterodyned signal appears near $t_3 = 1.1$ ps, whereas the probe-heterodyned signal appears near $t_3 = 0$ ps, as described in Chapter 3.2.1. The two contributions can therefore be isolated during post-processing by applying temporal windows centered at 1.1 ps and 0 ps, respectively. Because the probe and LO can have

different polarization states, the isolated heterodyne contributions can correspond to distinct polarization conditions. Removing the Glan-Thompson polarizer therefore enables two polarization-dependent signals to be acquired simultaneously within a single experiment.

For example, consider the (45°, 45°, 90°, 0°) polarization condition [1]. When the detector polarizer is removed, the LO heterodyne detected contribution retains the (45°, 45°, 90°, 0°) polarization-dependence, whereas the probe heterodyne detected signal corresponds to (45°, 45°, 90°, 90°). The isolated probe-heterodyned signal would require the same ϕ_{12} phase correction as the LO-heterodyned signal. However, it does not require a ϕ_{34} phase correction because the probe serves as both the third interaction field and the heterodyne field.

This strategy could be particularly beneficial for chiral probe measurements such as the XXXY polarization condition. In this case, the probe-heterodyned contribution corresponds to the dipolar XXXX polarization sequence, whereas the LO-heterodyned contribution corresponds to the chiral XXXY polarization sequence. Without polarization based probe rejection, however, the transmitted probe field may need to be attenuated to prevent detector saturation. Because the probe, LO, and signal propagate along the same wavevector, attenuation introduced downstream of the sample would reduce both XXXX and XXXY contributions. This loss is particularly undesirable for detecting the much weaker chiral signal.

A Wollaston prism positioned downstream of the sample could eliminate the need for common-path attenuation while preserving the dual-signal detection. The prism would angularly separate the orthogonally polarized field components, allowing the XXXX signal and probe field to be directed to a second spectrometer, while the LO field and XXXY signal are directed to the primary spectrometer. The probe amplitude and associated XXXX signal could then be attenuated independently without reducing the much weaker XXXY signal contribution. By acquiring the dipolar and chiral polarization sequences simultaneously,

this dual-channel detection scheme could substantially reduce the total acquisition time and thereby lessen the demands on long term laser stability and sample stability.

The preceding description neglects important experimental consequences that arise at longer waiting time delays. When t_2 exceeds the approximately 1.1 ps temporal separation between the LO and probe fields, the pump interactions occur before the LO arrives at the sample. The LO field can then act as the third interaction field, and/or the heterodyne reference and generate additional third-order signal contributions. As an example, consider again the XXXY polarization condition.

Under nominal XXXY polarization conditions and at waiting times longer than 1.1 ps, four third-order signal contributions can reach the detector. First, the E_{LO} field can serve as both the third interaction field and heterodyne reference field, producing the XXYY signal contribution. Second, E_{LO} can serve as the third interaction field while E_{probe} serves as the heterodyne reference, producing a XXYX contribution. Third, E_{probe} can serve as both the third interaction field and the heterodyne reference, producing a XXXX contribution. Finally, in the intended XXXY pathway, E_{probe} serves as the third interaction field and E_{LO} serves as the heterodyne reference.

Contributions for which the same field serves as both the third interaction field and the heterodyne reference field appear near t_3=0 ps in the detection time domain. In this example, the XXYY and XXXX contributions therefore overlap near t_3=0. The XXYX and XXXY signals involve a third interaction and heterodyne reference with fields temporally separated by 1.1 ps and therefore will appear at t_3=1.1 ps in the detection time domain. Therefore, both t_3=0 ps and t_3=1.1 ps will contain overlapping signals that cannot be isolated by temporal windowing alone.

This overlap of signals is potentially problematic because signals generated by the LO serving as the third interaction field evolve during an effective waiting time that is offset by 1.1 ps relative to the signals generated by the probe serving as the third field. The

severity of the resulting distortion depends on the amplitudes of the third interaction field and heterodyne reference field for a given contribution, the polarization sequence associated with that contribution, and the timescale of the dynamics being observed. However, under polarization conditions in which the probe and local oscillator are orthogonally polarized, a Glan-Thompson polarizer can be installed to reject the otherwise inseparable signal contributions.

When the Glan-Thompson polarizer is installed immediately downstream of the sample and aligned to transmit the Y polarized LO and signal, the X polarized probe and signal components are rejected. Consequently, the XXXX and XXYX signal contributions are blocked and the signals reaching the detector include the XXYY and XXXY contributions. Although the effective waiting times of these contributions are still offset by approximately 1.1 ps, the signals can be fully separated by applying a window in the detection-time domain centered at $t_3 = 0$ to isolate the XXYY contribution, or at $t_3 = 1.1$ ps to isolate the XXXY contribution.

This separation was validated by reprocessing the data shown in Chapter 4. In that experiment, the nominal polarization condition was XXXY, with the probe and LO assigned to orthogonal X and Y polarizations, respectively. The signal appearing near t_3=1.1 ps corresponds to the chiral XXXY contributions, whereas the dipolar XXYY contribution appears near t_3=0 ps. Figure 5.1 compares the isolated XXYY and XXXY 2DES spectra. As expected, the dipolar signals measured for the two TPPS L- and D- aggregate enantiomers exhibit similar spectral shapes and the same sign, whereas the chiral XXXY signals reverse signs between enantiomers. Figure 5.2 shows the detection-time projection of the 2DES data as a function of waiting time. The XXYY contribution emerges only after the waiting time exceeds approximately 1.1 ps, as expected from causality, because the LO cannot serve as the third field interaction until it arrives after the two pump interactions. Note, the waiting time points in this experiment were selected to characterize the evolution of the XXXY chiral

signal rather than the onset of the XXYY contribution. Consequently, relatively few waiting-time points were acquired near 1.1 ps, causing the XXYY signal to appear to emerge closer to 2 ps in the plotted data. Instead of using the Glan-Thompson polarized to completely block

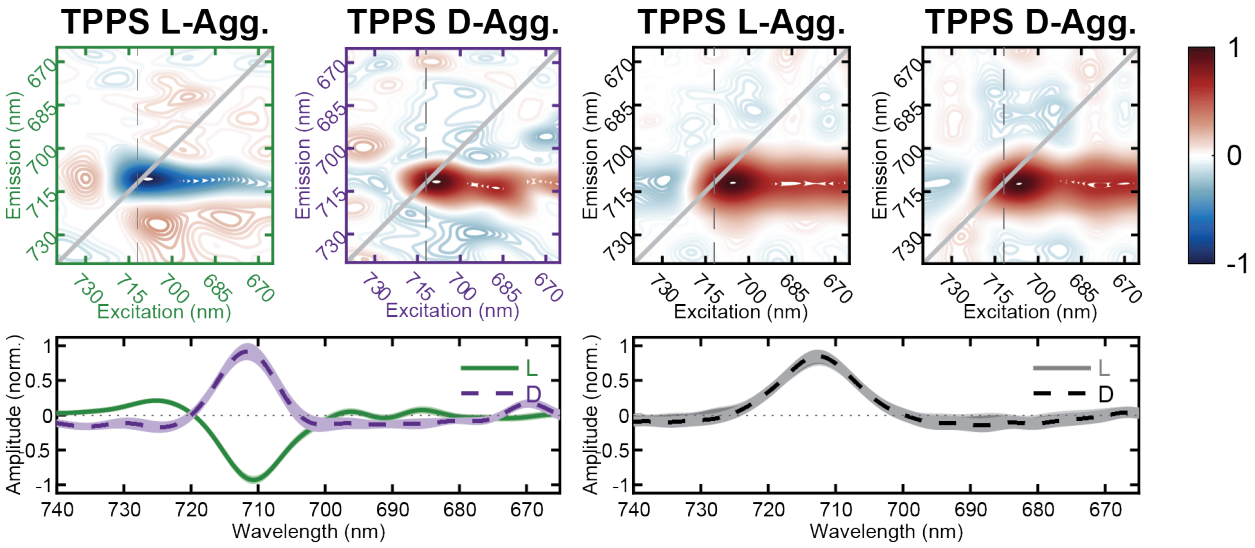

Figure 5.1: Normalized achiral and chiral 2DES data frames acquired at a waiting time of t_2=5000 fs. In the first row, columns 1 and 2 show the XXXY contributions measured for the TPPS L-aggregates and TPPS D-aggregates, respectively, while columns 3 and 4 show the corresponding XXYY contributions. The second row shows emission wavelength slices taken at an excitation wavelength of 712 nm. The left panel compares the TPPS L- and D- aggregates for the XXXY sequence, whereas the right panel shows the corresponding comparison for the XXYY polarization sequence.

the XXXX and XXYX contributions, a Wollaston prism could be installed downstream of the sample to angularly separate them from the XXYY and XXXY contributions. The XXXY and XXYY signals could be directed to the primary detector, while the XXXX and XXYX signals are directed to the secondary detector, or vice versa. For each detection channel, the two signals would be separable in the detection time domain. This configuration would therefore permit the simultaneous acquisition and independent analysis of four polarization sequences.

The four contributions would not, however, have comparable amplitudes. With the pump field amplitudes held constant, the heterodyne detected signal scales with the product of the

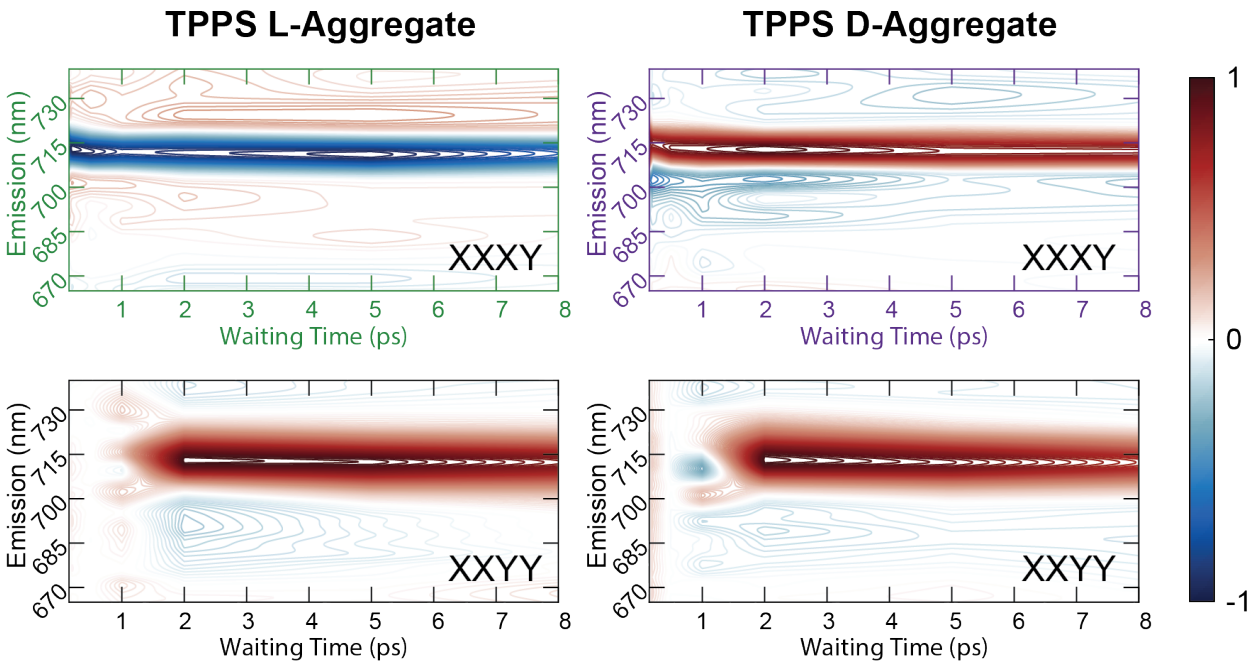

Figure 5.2: Projections of the achiral and chiral 2DES data over the excitation energy axis. The top row corresponds to the conventional pulse configuration, in which the probe serves as the third interaction field and the emitted signal is heterodyne detected by a temporally separated local oscillator field. This contribution is chiral and corresponds to the XXXY polarization sequence. The bottom row shows the contribution generated when the local oscillator serves as both the third interaction field and the heterodyne reference. This contribution is dipolar and corresponds to the XXYY polarization condition. The first and second columns show measurements of the TPPS L-aggregate and TPPS D-aggregate samples, respectively.

third interaction field amplitude and the heterodyne reference field amplitude. As a result, the scaling of the signal according to the field strength is given by

$$\begin{aligned} XXXX &\propto E_{\text{probe}}^2 \\ XXYX &\propto E_{\text{LO}} E_{\text{probe}} \\ XXXY &\propto E_{\text{probe}} E_{\text{LO}} \\ XXYY &\propto E_{\text{LO}}^2. \end{aligned} \tag{5.1}$$

where the nominal LO and probe field amplitudes are given by E_{LO}, and E_{probe}, respectively. Because the LO field amplitude is much weaker than the probe, the ordering expected from

the field amplitudes alone is

$$XXXX \gg XXYX = XXXY \gg XXYY. \tag{5.2}$$

This comparison does not include differences in orientational factors or the component of the intrinsic molecular response associated with each polarization sequence.

The XXYX and XXXY polarization sequences measure the chiral molecular response, so they are several orders of magnitude smaller than the XXYY and XXXX dipolar sequences. Because of this, in the detection channel measuring the XXXX and XXYX contributions, the weak XXYX signal may not be detectable due to the large attenuation of the X polarized fields required to prevent detector saturation. In contrast, simultaneous detection of the XXXY and XXYY contributions is feasible. Although the XXYY contribution depends on the weak LO serving as the third interaction field and the heterodyne reference, the polarization sequence measures the dipolar component of the molecular response, which is much stronger than the chiral XXXY polarization sequence detected along the same detection channel. This fact was shown in Figures 5.1 and 5.2. Even if only the XXXX, XXXY, and XXYY contributions can be resolved, their simultaneous acquisition could still be beneficial. One potential application is the measurement of anisotropy dynamics through comparison of the XXXX and XXYY signals.

One final case worth noting is when the probe and local oscillator are polarized parallel to one another. The rejection or redirection strategies described above rely on the probe and LO being orthogonally polarized. When their polarizations are parallel, the nominal signal and the additional contributions generated when the LO serves as the third interaction field cannot be separated using polarization optics. At waiting times longer than the probe-LO delay, these additional contributions are inseparable and contain shifted effective waiting time axes. This overlap can distort the measured signal and prevent accurate characterization of the dynamics associated with the nominal signal.

For this reason, employing an LO in the pump-probe geometry is not recommended for polarization conditions in which the LO and probe are parallel polarizations, unless the contributions generated when the LO acts as the third field interaction are negligible relative to the nominal signal generated when the probe acts as the third interaction field. For orthogonal probe/LO conditions, however, the separation strategies described above provide a unique opportunity to expand the information accessible in future 2DES measurements.

5.2 Experimental Considerations for Optimizing Routine 2DES Data Collection

Chiral 2DES is a technically demanding measurement because the chiral response is weak and can easily be obscured by the much larger achiral signal. Several approaches can be used to improve the signal to noise ratio and reduce contamination from the achiral signal. Considerations related to phase stability and polarization purity were already discussed in Chapter 3. Those strategies primarily aim to reduce the achiral signal contributions. This section instead focuses on alternative means of improving the fidelity of the detected signal through sample selection criteria, experimental modifications that can increase the signal-to-noise ratio of the detected signal, and post-processing strategies for noise reduction. While the data shown in Chapter 4 provides a strong initial demonstration of chiral 2DES, further optimization of the experimental and data processing methods could improve the technique and enable more detailed characterization of the chiral response.

5.2.1 Sample Selection Considerations

Several criteria were considered when selecting a suitable sample for the proof-of-concept experiments, including chiral signal strength, enantiomer availability, and sample stability. Selecting a chiral system with a relatively large rotational strength will likely yield a chiral

2DES signal with a higher signal-to-noise ratio. However, linear CD alone is not sufficient to predict the strength of a chiral 2DES signal. Linear CD contains magnetic dipole contributions and it probes transitions between the ground and one-exciton states with no temporal resolution. In contrast, chiral 2DES can contain both magnetic dipole and electric quadrupole contributions associated with one-exciton and two-exciton states.

The metric used to assess chiral signal strength in linear measurements is the dissymmetry factor or g-factor. The g-factor is the differential absorption of left- and right- circularly polarized light, divided by the corresponding non-polarized light absorption:

$$g = \frac{A^{LCP} - A^{RCP}}{A} \tag{5.3}$$

where A^{LCP} is the absorption of left circularly polarized light, A^{RCP} is the absorption of right circularly polarized light, and A is the absorption of non-polarized light [2].

Another important consideration is the availability of both sample enantiomers. The sample selected for the initial proof-of-concept 2DES measurements was a chiral porphyrin aggregate composed of achiral meso-tetrakis-(4-sulfonatophenyl)porphyrin (TPPS) monomers. Enantiomeric aggregates can be readily prepared by templating the aggregation with either L-valine or D-valine. The specific sample preparation details are in Appendix A.1. Measuring the chiral 2DES response of both enantiomers provided an important validation of signal purity, because a genuine chiral response should exhibit mirror-image signal symmetry between the corresponding spectra.

Without this enantiomer comparison, it would have been easy to interpret any measured signal that no longer resembled the conventional dipolar response as evidence of a successful chiral measurement. In practice, deviations from the expected mirror symmetry revealed polarization and phase induced artifacts that required months of experimental refinement to eliminate. These artifacts may not have been identified without the direct comparison between enantiomers. Although future chiral 2DES measurements may not always require

access to both enantiomers, appropriate control measurements remain essential for distinguishing genuine chiral signal from experimental artifacts.

While biological systems such as LH_2 exhibit some of the strongest rotational strengths, and may therefore be promising targets for chiral 2DES measurements, access to the opposite-handed structure is generally not possible. Chiral 2DES measurements on these systems remain feasible, provided the signal purity is confirmed using appropriate control measurements.

One approach to verify the performance of the experimental setup is to measure a control system for which both enantiomer forms are readily available, such as the TPPS aggregates. The TPPS aggregates exhibit a steady-state CD absorption over a wide range of the visible light spectrum, making them useful controls for chiral measurements performed at a variety of wavelengths. Their preparation is also relatively straightforward and generally requires one day of preparation. Measurements of the L- and D- aggregates can therefore be performed before investigating more complex systems to confirm the instrument reproduces the expected mirror-image spectra between enantiomers.

Another important consideration is sample stability. For the initial chiral measurements presented in Chapter 4, dipolar and chiral 2DES and TA data were collected for both TPPS enantiomers. Each 2DES acquisition consisted of 115 coherence time points and 11 waiting time points, with an integration time of 2 seconds at each time point. Each chiral 2DES data set was averaged 28 times, resulting in a total acquisition time of approximately 19.7 hours per sample. The sample must therefore remain stable over an extended period of time to prevent degradation-induced systematic trends in the measured dynamics.

One approach for mitigating these effects is to replace the static sample cell used in the current setup with a flow cell. Continuous circulation exchanges the sample volume at the laser focus, distributing the laser exposure over a larger sample volume. Flow can also reduce the effects of scatter from particulates in the sample by changing their positions within the

beam, allowing the resulting fluctuating scatter to average out over repeated measurements.

5.2.2 Noise Reduction Strategies

The proof of concept measurements presented in Chapter 4 demonstrated the ability of the chiral 2DES instrument to provide insight into the chiral excited-state evolution. However, the signal-to-noise ratio of these initial measurements was insufficient to reliably fit the observed dynamics to a dynamical model. Alternative measurement strategies will need to be explored to improve the signal to noise ratio enough to enable modeling of the chiral excited state evolution.

The chiral 2DES signal is several orders of magnitude weaker than the dipolar 2DES signal. Consequently, the signal to noise requirements to accurately characterize the dynamics and resolve spectral lineshapes are much more stringent. As shown in Figure 5.3, under dipolar polarization conditions, the features are clearly defined and remain observable throughout the 200 ps waiting time range shown. The signal amplitude remains well above the background noise, even though only 4 spectra were averaged to generate each of the displayed spectra. In contrast, under chiral polarization conditions, the noise is substantial at all waiting times despite averaging 28 spectra. Within picoseconds, the dominant features decay to the same order of magnitude as the background noise. One approach to improving the signal to noise ratio is to reduce noise contributions introduced during signal detection and readout. The total detection noise, (N), is dominated by contributions from readout noise (N_R), dark noise (N_D), and shot-noise (N_S) [3] .

$$N = (N_R^2 + N_S^2 + N_D^2)^{1/2}. \tag{5.4}$$

The readout noise and dark noise are both detector related noise sources. The readout noise arises from detector electronics and depends on the noise accumulated while the detected

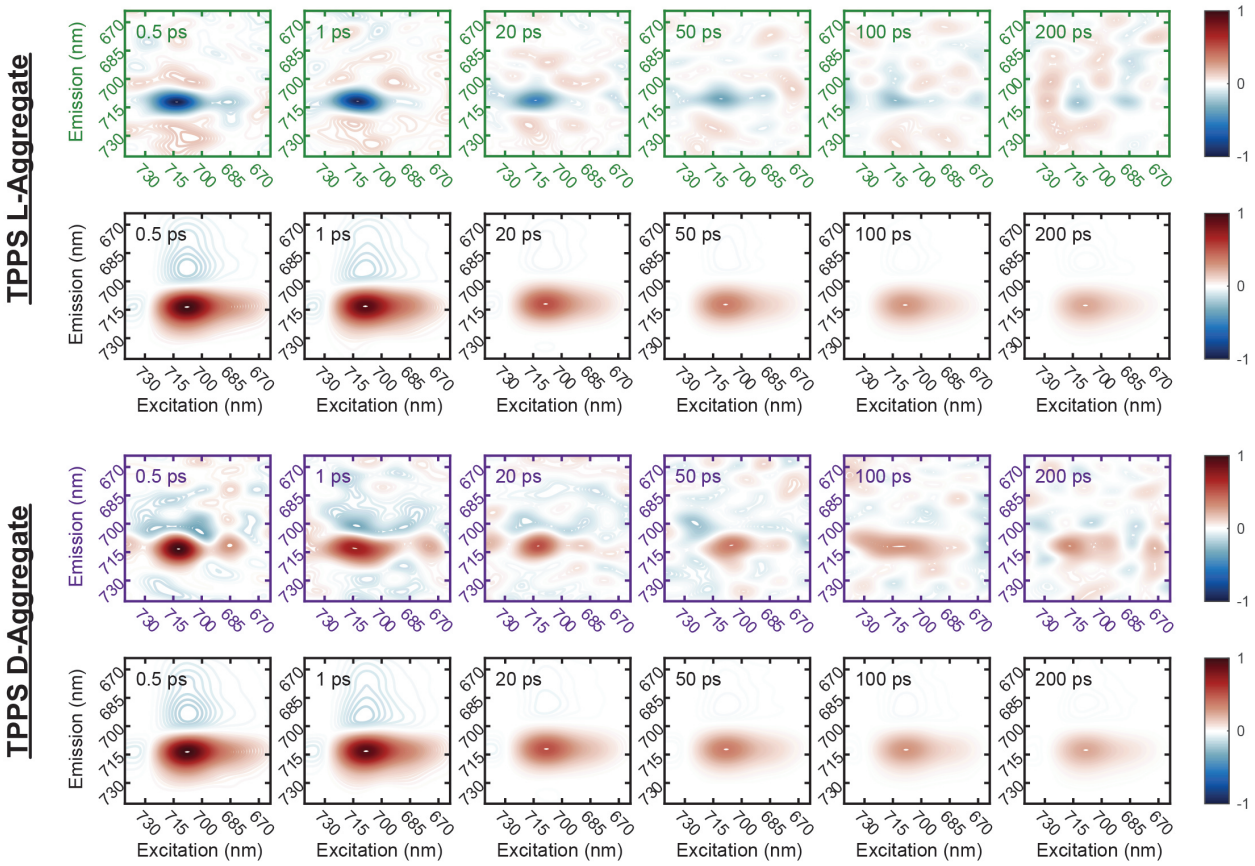

Figure 5.3: Time evolution of real 2DES frames measured under chiral (rows 1 and 3) and dipolar (rows 2 and 4) polarization conditions. TPPS L-aggregate data are compared in rows 1 and 2 and TPPS D-aggregate data are compared in rows 3 and 4.

signal is read out [4]. Dark current, in contrast, depends strongly on temperature. Detector temperature is therefore a parameter that can be varied to reduce noise by decreasing the amount of generated dark electrons and consequently, the associated dark noise [5]. Implementing a cooled detector therefore provides a route for reducing dark noise under low light conditions without requiring longer acquisition times and will be incorporated into future chiral measurements.

Enhancing the signal-to-noise by modifying the apparatus or acquisition settings is ideal, but several post-processing techniques can aid in the analysis of noisy data. One technique is singular value decomposition (SVD), which is a common dimensionality reduction technique used in spectroscopic analysis [6].

For a 2DES data set, the data is first reshaped along the excitation and emission frequency axes, yielding a two dimensional array of frequency and temporal information with dimensions given by [f x $(m \cdot n)$], where f defines the number of waiting time steps, n is the coherence frequency axis size, and m is the emission frequency axis size [7]. The reshaped 2D matrix, $\psi_{2DES}(\omega_{\omega_1,\omega_3}, t_2)$, is then deconstructed through SVD which is given by

$$\psi_{2DES}(\omega_{\omega_1,\omega_3}, t_2) = \mathbf{U} \cdot \mathbf{S} \cdot \mathbf{V^T} \tag{5.5}$$

where **U** and **V** are composed of the left and right singular vectors which correspond to the temporal and spectral singular vectors of the data, and **S** contains the singular values that weight the individual components.

Following this deconstruction, the dominant components can be isolated and either analyzed independently or used to reconstruct the data. By omitting the insignificant components from the data, SVD serves as an effective noise filter [8]. The reconstructed data is re-expressed using a prime notation to indicate the most significant elements of the original matrices, **U'**, **S'**, and **V'** were retained.

$$\psi'_{2DES}(\omega_{\omega_1,\omega_3}, t_2) = \mathbf{U'} \cdot \mathbf{S'} \cdot \mathbf{V'^T} \tag{5.6}$$

As an example, SVD analysis was performed on the chiral and achiral data sets shown in Chapter 4. In Figure 5.4, the singular value weights are plotted with respect to each component number. Under dipolar polarization conditions, the weights of the spectral components begin to plateau for component numbers exceeding two. This trend is also followed for the chiral conditions; however, the fractional weights of the larger component numbers are much larger relative to the first component. Using this trend, the first two components were used to reconstruct the chiral and achiral data for analysis, which are compared in Figure 5.5. 2DES spectra at waiting times = 1000 fs are compared. Under dipolar polarization conditions,

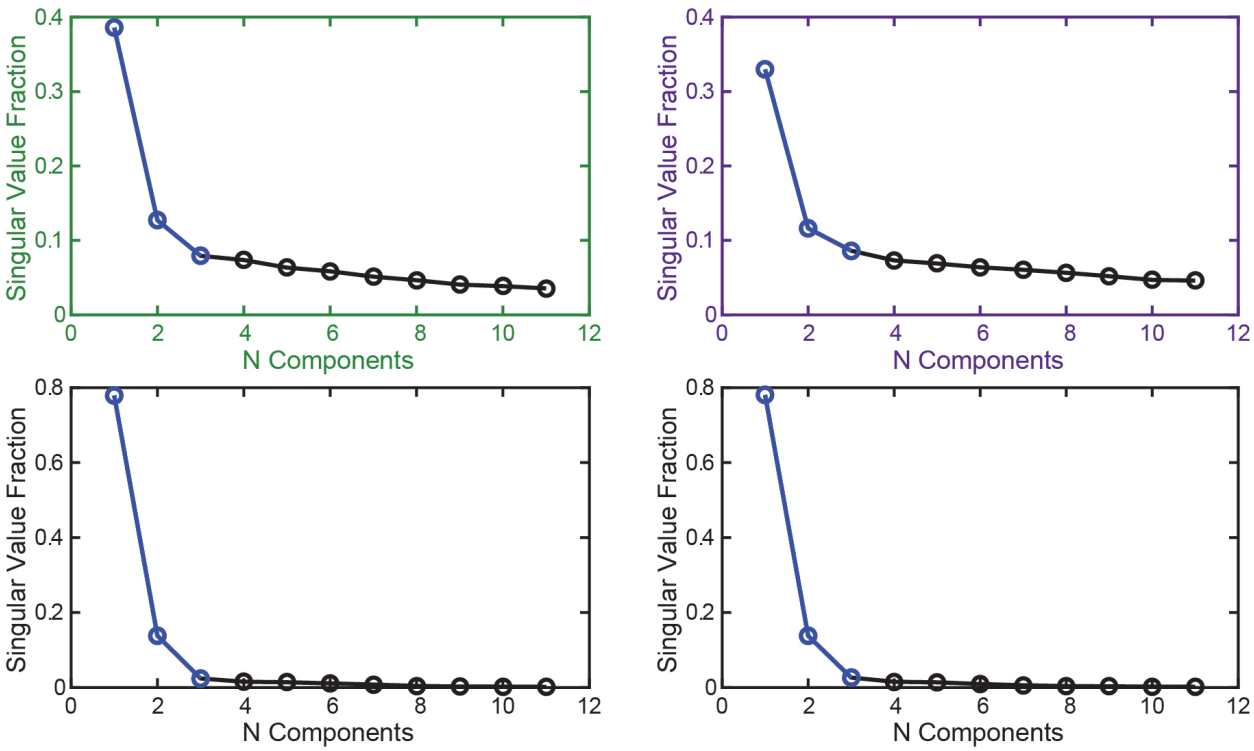

Figure 5.4: Singular value decomposition analysis on L- and D- aggregates acquired under chiral and achiral polarization conditions. Singular value weights are plotted as a function of the component number for L-TPPS aggregates (left column) and for D-TPPS aggregates (right column) with respect to the component number. The top row corresponds to the data acquired under chiral polarization conditions and the bottom row corresponds to the data acquired under dipolar polarization conditions. The blue markers represent the three most dominant components contributing to the signal

the spectra appear unchanged between the measured signal and the SVD reconstruction, indicating the first two spectral components are needed to describe the dominant features. However, under chiral polarization conditions, the lineshapes of the reconstructed data are much better defined relative to the original spectra. This improvement is further proof that SVD can aid in spectral analysis through noise omission.

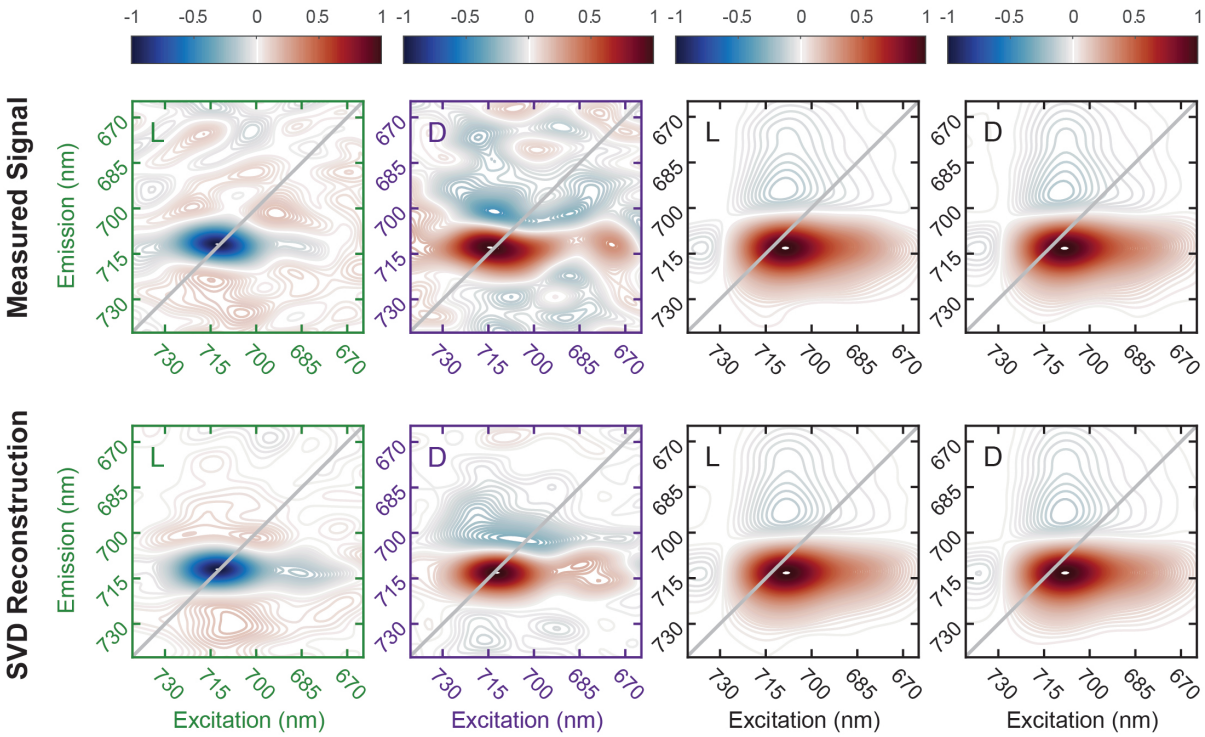

Figure 5.5: 2DES frames at waiting time = 1000 fs comparing the full measured signal (top row) to the SVD reconstruction. The 2DES reconstruction utilizes the first two SVD components. The first and second columns show spectra collected under chiral polarization conditions for the L- and D-TPPS aggregate samples, respectively. The third and fourth columns show the L- and D-TPPS aggregate data, respectively, measured under dipolar polarization conditions.

References

(1) Myers, J. A.; Lewis, K. L. M.; Tekavec, P. F.; Ogilvie, J. P. Two-color two-dimensional Fourier transform electronic spectroscopy with a pulse-shaper. *Opt. Express* **2008**, *16*, 17420–17428.

(2) Berova, N.; Bari, L. D.; Pescitelli, G. Application of electronic circular dichroism in configurational and conformational analysis of organic compounds. *Chemical Society Reviews* **2007**, *36*, 914–931.

(3) Zonios, G. Noise and stray light characterization of a compact CCD spectrophotometer used in biomedical applications. *Appl. Opt.* **2010**, *49*, 163–169.

(4) Thorlabs — thorlabs.com, `https://www.thorlabs.com/camera-noise-and-temperature-tutorial?tab{N}ame={C}amera%20{N}oise`, [Accessed 23-07-2026].

(5) Widenhorn, R.; Blouke, M. M.; Weber, A.; Rest, A.; Bodegom, E. In *Sensors and Camera Systems for Scientific, Industrial, and Digital Photography Applications III*, ed. by Sampat, N.; Canosa, J.; Blouke, M. M.; Canosa, J.; Sampat, N., SPIE: 2002; Vol. 4669, pp 193–201.

(6) Henry, E.; Hofrichter, J. In *Numerical Computer Methods*; Methods in Enzymology, Vol. 210; Academic Press: 1992, pp 129–192.

(7) Lee, Y.; Gorka, M.; Golbeck, J. H.; Anna, J. M. Ultrafast Energy Transfer Involving the Red Chlorophylls of Cyanobacterial Photosystem I Probed through Two-Dimensional Electronic Spectroscopy. *Journal of the American Chemical Society* **2018**, *140*, PMID: 30133281, 11631–11638.

(8) Schmidt, M.; Rajagopal, S.; Ren, Z.; Moffat, K. Application of singular value decomposition to the analysis of time-resolved macromolecular X-ray data. *Biophysical journal* **2003**, *84*, 2112–2129.

CHAPTER 6

CONCLUSIONS

Chirality is a geometric property that directly influences light-matter interactions and the ensuing excited-state dynamics. Harnessing chiral light-matter interactions can enable the development of smaller and more efficient devices that use sensitivity to optical helicity as an additional degree of freedom. Characterizing the underlying relationship between a material's chiral structure and its resulting excited-state dynamics remains an ongoing goal of chiral spectroscopy. However, measuring chiral dynamics is challenging, because the inherently weak chiral response must be isolated from a much stronger achiral contribution. Even small polarization impurities can introduce achiral signal leakage that overwhelms the chiral response.

This thesis describes the development of a chiral two-dimensional electronic spectrometer designed to mitigate common experimental errors that prevent the accurate measurement of third-order chiral signals. The instrument sensitively detects the weak chiral signal while minimizing polarization impurities that would otherwise prevent its isolation from the much stronger achiral signal. We employ a partially collinear pump-probe geometry in which two collinear pump pulses propagate along one wavevector, while the probe and local oscillator share a second propagation direction. This geometry improves phase stability and greatly simplifies the polarization control. To prepare the pulse polarizations with sufficient purity to suppress the achiral response, the instrument exploits the natural polarization axes of birefringent materials for both chiral pump and chiral probe 2DES measurements.

Despite the use of birefringent materials to generate pure polarizations, polarization impurities can nonetheless be introduced from metal mirror reflections and wave plates. To mitigate these common sources of polarization artifacts, the polarization optics, optical ordering, and beam propagation were strategically selected to minimize polarization contamination. For chiral probe polarization conditions, impurities introduced by metal mirror

reflections were removed by installing the final polarization setting optics immediately upstream from the sample cell. Modified mounts were machined for this purpose, enabling independent manipulation of the pump or probe path polarization while maintaining a small beam crossing angle at the overlap position within the sample.

Additional artifacts that obscure the chiral response can arise from phase inaccuracies, which cause the absorptive and dispersive signal components to mix. Phase measurement and correction procedures were therefore developed to ensure their accurate separation. In addition, a second spectrometer was employed to continuously measure phase drift for correction during post processing. Both phase and polarization errors can arise from strain-induced birefringence. To mitigate these effects, a low-strain sample mount was engineered and confirmed to have negligible influence on the polarization and phase fidelity of the beams.

Methods were developed to simplify pulse polarization preparation and validation. For experiments employing chiral probe polarization conditions, the reduced dimensionality of transient absorption measurements can be exploited to rapidly optimize the polarization angle. The polarization is finely adjusted near the ideal chiral polarization angle to minimize the response of an achiral reference sample, which should ideally produce negligible signal under these polarization conditions. The polarization setting is then further validated by comparing chiral 2DES spectra acquired from opposite molecular enantiomers. Equal and opposite signal symmetry indicates that the phase correction and polarization purity are sufficient for a given system. This symmetry test therefore provides a routine method for validating the instrument before investigating samples that may not have easily accessible enantiomers. Additional methods were developed to simultaneously measure and isolate chiral and achiral signals, thereby reducing acquisition time while providing an internal achiral signal control. The efficacy of these methods and instrument design choices was validated through initial proof of concept measurements presented in Chapter 4.

The excitonic chirality of helical porphyrin J-aggregates was investigated in an initial

proof-of-concept experiment. Chiral 2DES spectra of aggregate enantiomers were acquired under achiral and chiral probe polarization conditions. Under chiral polarization conditions, the differences in the signs and relative amplitudes of spectral features enhanced the visibility of weak features that were less apparent in achiral spectra. Chiral measurements are sensitive to the handed spatial arrangement of the coupled transition dipoles, which gives rise to their differential coupling to left and right circularly polarized light. This sensitivity produced mirrored spectra for aggregates of opposite handedness and provided information about both the spatial arrangement of coupled transition dipoles, and their role in chiral energy transfer. The mirror symmetry of the chiral spectra is evidence that the spectrometer achieved sufficient polarization purity and accurate phasing. In contrast, the achiral spectra of the two enantiomers were identical within experimental uncertainty, providing an experimental control.

In conclusion, a chiral two-dimensional electronic spectrometer was developed and validated through an initial proof-of-concept experiment establishing chiral 2DES as a tool for investigating the relationships between chiral structure and electronic dynamics. The enhanced visibility of weak spectral features demonstrates the potential advantage of chiral 2DES for resolving contributions to the excited state response that are obscured in traditional achiral measurements. The apparatus design and measurement procedures developed in this thesis enable the routine execution of chiral 2DES and provide a foundation for defining the structure-dynamics relationships in chiral systems. These capabilities can ultimately inform the design of chiral systems with tailored photophysical properties for specific device applications.

APPENDIX A

TPPS AGGREGATE SAMPLE INFORMATION

A.1 TPPS Aggregate Synthesis

Chiral TPPS aggregates were synthesized in-house approximately 30 days prior to the 2DES and TA measurements reported in Chapter 4. The synthesis began with the preparation of a monomer stock solution. 0.94 mg of TPPS monomer (purchased from Tokyo Chemical Industry) was dissolved in 4 mL of deionized (DI) water that was pre-adjusted to a pH of 3.13 by addition of H_2SO_4. This mixture was left to dissolve at room temperature for 25 minutes. While the monomer stock solution was dissolving, the amino acid templates were prepared. The L-and D-aggregate conditions were set by adding 1.56 mg of NaCl and into each of two Eppendorf tubes, followed by 7.06 mg (7.07 mg) of L(D)-valine into the first and second tubes, respectively. 1.2 mL of the TPPS monomer stock solution was then added to each Eppendorf tube. The Eppendorf tubes were lightly mixed through 20 inversions, followed by 2s of vortexing. The Eppendorf tubes were stored overnight. On day 2, an additional 0.3 mL of 3.13 pH DI water was added to each Eppendorf tube, adjusting the aggregate concentration slightly so the final OD remained well below 0.3 in a 100 um path length cuvette within our laser spectral range of 650 nm to 750 nm. The final concentrations of the TPPS monomer, NaCl, and L(D)-valine were 2.0 X 10^2 uM, 17.8 mM, and 40.2mM(40.2mM) respectively. The samples were stored under ambient conditions in a dark drawer for approximately 1 month prior to making 2DES and TA measurements due to unstable laser lab conditions. However, the described synthetic conditions for chiral TPPS aggregates yield stable aggregates.